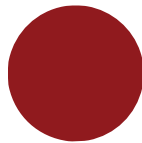


MASTER THESIS

SPIN-PHOTON ENTANGLEMENT
REALISED BY QUANTUM DOTS
EMBEDDED IN WAVEGUIDES



UNIVERSITY OF
COPENHAGEN

MIKKEL BLOCH LAURITZEN

SPIN-PHOTON ENTANGLEMENT REALISED BY QUANTUM DOTS EMBEDDED IN WAVEGUIDES

Author Mikkel Bloch Lauritzen
Advisor Anders S. Sørensen¹
Advisor Peter Lodahl¹

¹Hy-Q, The Niels Bohr Institute

Hy-Q
The Niels Bohr Institute

Submitted to the University of Copenhagen
March 4, 2019

Abstract

Spin-photon Entanglement Realised by Quantum Dots Embedded in Waveguides

by Mikkel Bloch Lauritzen

Quantum information theory is a relatively new and rapidly growing field of physics which in the last decades has made predictions of exciting features with no classical counterpart. The fact that the properties of quantum systems differ significantly from classical systems create opportunities for new communication protocols and sharing of information. Within all these applications, entanglement is an essential quantum feature. Having reliable sources of highly entangled qubits is paramount when applying quantum information theory. The performance of these sources is limited both by unwanted interaction with the environment and by the performance of experimental equipment. In this thesis, two protocols which creates highly entangled spin-photon quantum states are presented and imperfections in the protocols are studied. The two spin-photon entanglement protocols are both realised by quantum dots embedded in waveguides. The studied imperfections relate to both the visibility of the system, the ability to separate the ground states, and the branching ratio of spontaneous decay, photon loss and phonon induced pure dephasing. In the study, realistic parameter values are applied which are based on experimental results. It is found, that the two studied protocols are promising and likely to perform well if applied in the laboratory to create highly entangled states.

Acknowledgements

To my friends expecting a funny acknowledgement, I am sorry, but no jokes will be included. This thesis must be submitted in a few hours and I am tired.

First and foremost, I wish to thank my supervisor Anders Sørensen for teaching me quantum mechanics in 2014, quantum information in 2017 and finally supervising in this thesis. Secondly, I would like to thank my second supervisor Peter Lodahl and Martin Appel for teaching me the experimental aspects described of this thesis. Many thanks to Smads, Slars, and Durak for the moral support. Lastly I would like to thank Helle for explaining to me how to explain and teaching me that it's unscientific to use abbreviations. Okay, maybe a single joke.

Contents

Abstract	3
Acknowledgements	5
1 Introduction	1
2 Quantum Entanglement	3
2.1 Entanglement	3
2.1.1 Entanglement in Quantum Information Theory	4
2.2 Fidelity	4
3 Nanophotonics	7
3.1 Quantum dots	7
3.1.1 Spin Dynamics and Optics of a Singly Charged Self-Assembled Quantum Dot	8
3.1.2 The Zeeman Effect	9
Optical Transitions	10
3.1.3 Hyperfine Interactions and Spin Coherence	10
3.2 Nanophotonic Waveguides	12
3.2.1 Purcell Enhancement and the β Factor	13
4 Four Level System	15
4.1 The Hamiltonian	15
4.2 Wavefunction	16
4.3 Schrödinger Equation	17
5 Spin-Photon Frequency Entanglement	23
5.1 Sub-maximal Entanglement	24
5.1.1 Orthogonal Basis	25
5.1.2 State Fidelity	26
5.2 Visibility	27
5.2.1 Non-Averaged Visibility Fidelity	28
5.2.2 Averaged Visibility Fidelity	28
5.2.3 Optimising the Combined Fidelity	33
6 Spin-photon Time-Bin Entanglement	37
6.1 Visibility	38
6.1.1 The Ideal State and Output State	38
6.1.2 Visibility Fidelity	39
6.2 Imperfect Decay Ratio and Photon Loss	46
6.2.1 The Output State	47
6.2.2 The Conditional Decay Fidelity	49
6.3 Phonon Induced Pure Dephasing	56
6.3.1 Hamiltonian and Wavefunction	56

6.3.2	Rotating Frame	58
6.3.3	Ideal State and Output State	63
6.3.4	Dephasing Fidelity	64
6.4	Combined Fidelity	66
7	Conclusion and Outlook	69
7.1	Conclusion	69
7.2	Outlook	70
A	Photon basis	71
A.1	Normalised Orthogonal Photon Basis	71
B	Coherence time	73
C	Combined Fidelity	75
C.1	Validity of the combined fidelity perturbative expression	75
D	Phonons	77
D.1	Phonon Coherent State	77
D.2	Displaced Vacuum	77

Chapter 1

Introduction

Claude Shannon earned the title "The Father of the Digital Age" in 1948 when he published the article *A Mathematical Theory of Communication* [1]. In this article, Shannon introduced the concept of information entropy defined as

$$H(X) = - \sum_{i=0}^n P(x_i) \log_b P(x_i), \quad (1.1)$$

where X is a discrete random variable with possible values $\{x_1, \dots, x_n\}$ and b is the base of the logarithm. Imagining a single toss of a coin. There are two possible outcomes, heads or tails, each with equal probability $1/2$. In the logarithm base $b = 2$, the information entropy describing the toss is

$$H(X) = - \sum_{i=1}^2 P(x_i) \log_2 P(x_i) \quad (1.2)$$

$$= -\frac{1}{2} \log_2 \left(\frac{1}{2}\right) - \frac{1}{2} \log_2 \left(\frac{1}{2}\right) \quad (1.3)$$

$$= 1, \quad (1.4)$$

which defines the basic unit in information theory, sometimes referred to as a *shannon* but more commonly known as a *bit*. In present day computers and cell phones, the bit is not realised by coins but most often low DC voltage, where a certain voltage corresponds to a logical value of 0 or 1. Any physical system of two equally possible distinct states is in principle a bit and in the early 1980s Paul Benioff [2], Yuri Manin [3], Richard Feynman [4] and David Deutsch [5] pioneered the field of *quantum computing*, where the physical system is governed by the laws of quantum mechanics. This introduces a fundamental difference in the way we think of bits, since quantum mechanics allows for the system to be in a superposition of the two states and hence simultaneously 0 and 1. This is known as a *qubit*, which is the basic unit of quantum information, and can be described as a state which is a linear combination of $|0\rangle$ and $|1\rangle$

$$|\psi\rangle = c_0 |0\rangle + c_1 |1\rangle, \quad (1.5)$$

where c_0 and c_1 are probability amplitudes. The qubit have been realised in the last decade by different physical systems such as atoms, superconductors and semiconductors. Based upon the qubit, many exciting proposals have been contemplated such as quantum algorithms [6, 7] and quantum cryptography [8].

This thesis presents a theoretical study of two different protocols which create qubits. Specifically, it studies possible imperfections in the protocols which can affect the

qubits and possible ruin them. These imperfections arises from unwanted interaction between the system creating the desired qubits and the surrounding environment and from limited performance of the experimental equipment. The protocols studied in this thesis are both realised using a system where a single spin is confined within a quantum dot influenced by an external magnetic field and embedded in a waveguide. In the first protocol, purposed by Gao et. al [9], the qubits are realised from the spin of a spin half particle and the frequency of a photon. In the second protocol, purposed by Lee et. al [10], the qubits are likewise realised from spin of a spin half particle and by the time-bin in which a photon is detected. The outline of this thesis is as follows:

- **Chapter 2:** The concept of quantum entanglement is briefly introduced, focusing on how entanglement is applied within quantum information theory. The measure of *fidelity* is introduced which quantifies the probability that two quantum states are identified as each other in a measurement. The fidelity is the primary tool used in the study of protocol imperfections considered in this thesis.
- **Chapter 3:** Photonic nanostructures are introduced focusing on semiconductor quantum dots and nanophotonic waveguides, as these structures constitute the physical system realising the protocols. Advantages and disadvantages of employing photonic nanostructures are discussed.
- **Chapter 4:** Solving the Schrödinger equation, the equations of motion corresponding to a four level diagram are found and solved. The considered system consists of a single spin confined within a quantum dot influenced by an external magnetic field. Such a four level system is applied in the two studied protocols.
- **Chapter 5:** The spin-photon frequency entanglement protocol [9] is presented and imperfections are studied.
- **Chapter 6:** The spin-photon time-bin entanglement protocol [10] is presented and imperfections are studied.
- **Chapter 7:** The studies of imperfections in the two protocols are concluded and the need for further theoretical investigation is discussed.

Chapter 2

Quantum Entanglement

Quantum entanglement is a concept that is easily explained but hard to grasp. In this section, entanglement is first defined and then several important aspects and applications of entanglement are discussed. Furthermore, the measure of fidelity is presented and motivated.

2.1 Entanglement

In a single sentence, entanglement can be qualitatively explained as: *quantum correlation between two or more particles such that the state of each particle cannot be described individually* (note, however, that two or more particles can be correlated even though they are not entangled). Mathematically, an entangled state of two or more particles, must satisfy:

$$|\Psi\rangle_{AB\dots} \neq |\psi\rangle_A \otimes |\psi\rangle_B \otimes \dots \quad (2.1)$$

Equation (2.1) shows that a state $|\Psi\rangle_{AB\dots}$ of multiple particles is entangled when it is not identical to the product of states for each subsystem. We say that the state $|\Psi\rangle_{AB\dots}$ is *non-separable*. For simplicity we begin by considering bipartite systems, i.e. systems with a Hilbert space equal to the direct product of two factors,

$$\mathcal{H}_{AB} = \mathcal{H}_A \otimes \mathcal{H}_B, \quad (2.2)$$

and hence the criteria of (2.1) simplifies to

$$|\Psi\rangle_{AB} \neq |\psi\rangle_A \otimes |\psi\rangle_B. \quad (2.3)$$

A simple but important example of such systems is the Bell states. The four Bell states are two qubit states defined as:

$$|\Phi^\pm\rangle_{AB} = \frac{1}{\sqrt{2}} \left(|0\rangle_A \otimes |0\rangle_B \pm |1\rangle_A \otimes |1\rangle_B \right) \quad (2.4)$$

$$|\Psi^\pm\rangle_{AB} = \frac{1}{\sqrt{2}} \left(|0\rangle_A \otimes |1\rangle_B \pm |1\rangle_A \otimes |0\rangle_B \right). \quad (2.5)$$

All of the four Bell states fulfill (2.3) and are thus entangled. Furthermore, the Bell states are maximally entangled, meaning the reduced density matrix with respect to either of the subsystems is maximally mixed, i.e. if one traces over the subsystem A then the reduced density operator of the system will be a multiple of the identity

operator. We show this explicitly for (2.4)

$$\hat{\rho}_B = \text{Tr}_A [|\Phi^\pm\rangle_{AB} \langle\Phi^\pm|_{AB}] \quad (2.6)$$

$$= \text{Tr}_A \left[\frac{1}{2} (|0\rangle_A \otimes |0\rangle_B \pm |1\rangle_A \otimes |1\rangle_B) (\langle 0|_B \otimes \langle 0|_A \pm \langle 1|_B \otimes \langle 1|_A) \right] \quad (2.7)$$

$$= \text{Tr}_A \left[\frac{1}{2} (|0\rangle_A \otimes |0\rangle_B \langle 0|_B \otimes \langle 0|_A + |1\rangle_A \otimes |1\rangle_B \langle 1|_B \otimes \langle 1|_A) \right. \\ \left. \pm |0\rangle_A \otimes |0\rangle_B \langle 1|_B \otimes \langle 1|_A \pm |1\rangle_A \otimes |1\rangle_B \langle 0|_B \otimes \langle 0|_A \right] \quad (2.8)$$

$$= \frac{1}{2} (|0\rangle_B \langle 0|_B + |1\rangle_B \langle 1|_B) \quad (2.9)$$

$$= \frac{1}{2} I_B. \quad (2.10)$$

This is equivalent to saying that if we measure in subsystem B the result will be completely random. 0 or 1 with equal probability $1/2$. The same is true for subsystem A if we trace out B . However, there is a perfect correlation between subsystem A and B as seen from (2.4). If we measure 0 (1) in B we will also measure 0 (1) in A . Bell states are for those reasons very desirable in quantum information theory.

2.1.1 Entanglement in Quantum Information Theory

Imagine the Bell states as two entangled qubits. Now imagine the two subsystems A and B to be spatially separated. For example, subsystem A could be a laboratory where a girl called Alice works. Thousands of kilometres away is a laboratory, subsystem B , where a boy called Bob works. The idea is now that a channel exists between Alice and Bob via the entanglement of the qubit pairs. Some applications of this channel include superdense coding [11] and quantum teleportation [12]. Shared Bell states have also been used to test the fundamental principles of quantum mechanics [13].

A Bell state is the simplest example of shared qubits between Alice and Bob, but more complex, multi-particle quantum states can also be shared between two or more parties. For example the Greenberger–Horne–Zeilinger (GHZ) state:

$$|GHZ\rangle = \frac{1}{\sqrt{2}} (|1\rangle^{\otimes N} + |0\rangle^{\otimes N}), \quad N > 2. \quad (2.11)$$

which can be used for quantum secret sharing between an arbitrary number of parties [14, 15].

Above we motivated the use of entanglement by spatially separating Alice and Bob, hence all examples given so far are examples of quantum *communication*. But entanglement can also be useful for local applications such as the one-way quantum computing, where one performs single qubit measurements on a so-called cluster state [16].

2.2 Fidelity

In chapter 5 and 6, different protocols are introduced which are used to create highly entangled spin-photon states. When applying these protocols, it is crucial to examine possible imperfections since these ruin the entanglement of the ideal states. Hence, it is necessary to have a measure of how closely an output state $|\psi_{output}\rangle$, influenced by

imperfections, resembles an ideal state $|\psi_{ideal}\rangle$, not influenced by any imperfections. Since our ideal states are highly entangled, this measure also becomes a measure of entanglement.

One of the most widely used measures is fidelity. For a given output state, the fidelity is defined as the overlap between an ideal target state and the output state,

$$F = |\langle \psi_{ideal} | \psi_{output} \rangle|^2 \quad (2.12)$$

for which $0 \leq F \leq 1$ where $F = 1$ if and only if $|\psi_{output}\rangle = |\psi_{ideal}\rangle$. The fidelity is very useful when minimising the effect of imperfections, since this is equal to maximising the fidelity, and will be used repeatedly in chapter 5 and 6.

Chapter 3

Nanophotonics

The protocols examined in this thesis are realised utilising photonic nanostructures in which light is manipulated and confined on the nanometer scale. In this chapter, relevant concepts within nanophotonics are introduced. First, quantum dots are examined in section 3.1. Then, by studying spin dynamics and optics, it is shown that quantum dots serve excellently as single photon emitters - especially if the dots are embedded in so-called photonic crystals which we cover in section 3.2.

3.1 Quantum dots

Simply put, a quantum dot is a tiny ensemble of semiconducting matter, typically $10^4 - 10^6$ atoms, dimensions of only several nanometers and with optical properties similar to those of a single atom. They are often referred to as artificial atoms. The key to understanding quantum dots is to understand charge carrier (electrons and holes) confinement in semiconductors. If a region of lower bandgap material is interfaced with a higher band gap material, the charge carriers will be confined within the region of low energy in the valence and conduction band. Hence this structure is similar to that of the well-known square well. If some lower bandgap material is completely surrounded by higher band gap material, such that the charge carrier is confined in all three spatial dimensions, a three-dimensional square well is formed which is called a quantum dot.

There are many different types of quantum dots, which differ in materials, growth method etc., but here we shall restrict our selves to discussing Indium Arsenide (InAs) self-assembled quantum dots embedded in Gallium Arsenide (GaAs) grown by the Stranski-Krastanov method [17]. These quantum dots are created using a flat baselayer of GaAs upon which single mono-layers of InAs are applied. This thin layer of InAs is called the wetting layer. At some point, tiny islands of InAs will be formed, known as nuclearisation, due to a 7% larger lattice constant of InAs than GaAs since this formation of islands minimises the binding energy. Lastly, the InAs islands are capped with GaAs.

The properties of self-assembled quantum dots depend on several factors, such as size and composition, which differ from dot to dot. As one might expect, the strain-driven process of nuclearisation is random. Hence the size and composition of the quantum dots is, to some extent, uncontrollable, and the islands formed across the GaAs surface will have a distribution of size and composition. The width of the distribution depends on the material system and growth conditions [18].

Some properties, however, can be controlled. In the next section, we discuss singly charged self-assembled quantum dots and how to manipulate the spin of the trapped electron or hole.

3.1.1 Spin Dynamics and Optics of a Singly Charged Self-Assembled Quantum Dot

Imaging a single trapped electron or hole in a self-assembled quantum dot (such a system can be achieved by different techniques [19]-[22]). The optically excited states are trion states. For an electron in the ground state, the trion states are singlet electrons and a lone hole with either spin up or spin down. This is known as a negative trion (denoted $|X^- \rangle \equiv |\uparrow\downarrow, \uparrow \rangle \wedge |\uparrow\downarrow, \downarrow \rangle$). For a hole in the ground state, the trion consists of paired holes and a lone electron with either spin up or spin down. This is known as a positive trion (denoted $|X^+ \rangle \equiv |\uparrow\downarrow, \uparrow \rangle \wedge |\uparrow\downarrow, \downarrow \rangle$).

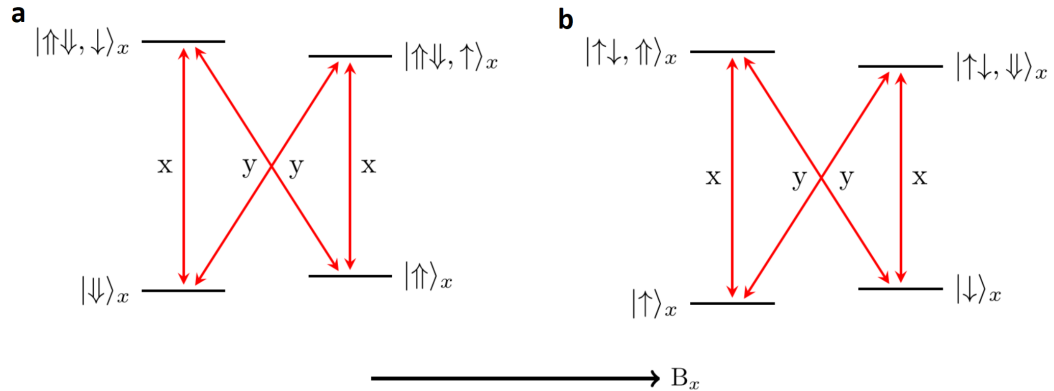


FIGURE 3.1: Level diagrams of a singly charged quantum dot with an electron (**a**) and a hole (**b**) in the ground state. The spins are written in the eigenbasis of the applied magnetic field which is oriented in the in-plane x-direction, known as Voigt geometry. This allows both diagonal transitions (y-polarised light) and vertical transitions (x-polarised light). The hole is assumed to be in a pure heavy hole state.

Fig. 3.1 shows the level diagrams of a singly charged quantum dot in the ideal limit where the heavy hole contribution is dominant in the so called effective mass description. In this description, often referred to as $\mathbf{k} \cdot \mathbf{p}$ model, the hole state is constructed from heavy-hole ($J = 3/2, J_z = \pm 3/2$), light-hole ($J = 3/2, J_z = \pm 1/2$) and spin-orbit split-off ($J = 1/2, J_z = \pm 1/2$). The strain and strong vertical confinement in the quantum dot reduces the light-hole component while the spin-orbit interaction and the large energy spacing compared to the Coulomb energy, known as the strong-confinement regime, reduces the mixing of the valence band. Resultant, we can describe the features of a quantum dot using only two bands. This is illustrated in fig 3.2, which corresponds to the level diagrams shown in fig. 3.1, where only the heavy-hole in the valence- and conduction-band is included, for further discussion see [23, 24].

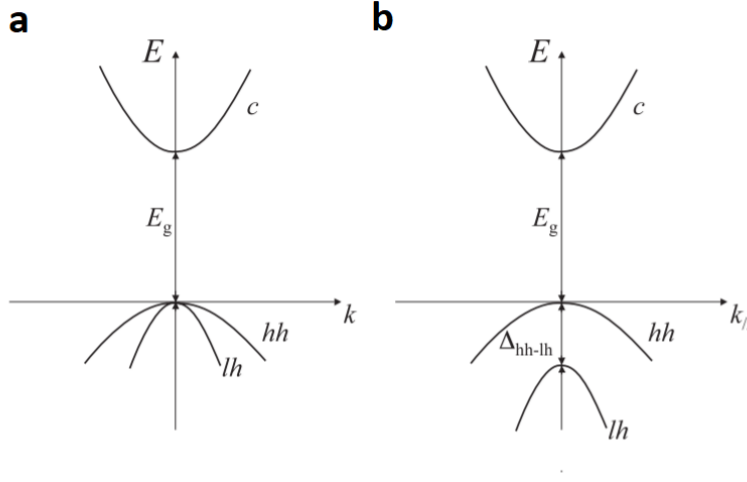


FIGURE 3.2: Illustration of the bandstructure around the Γ point in the effective mass description showing the lowest conduction band and the two upper valence bands. The split-off band is not included since it typically is sufficiently separated from the light hole and heavy hole that it can be ignored. In (a), the light hole, lh, and the heavy hole, hh, are at the same energy level whereas in (b), the heavy hole and light hole are separated by the energy gap δ_{hh-lh} . The picture is taken from [26].

3.1.2 The Zeeman Effect

The electron and hole spin states are split by the Zeeman effect due to an external magnetic field. The Hamiltonian of the Zeeman interaction for an electron and a hole are respectively determined as:

$$\hat{H}_{Zeeman}^e = \frac{\mu_B}{\hbar} \mathbf{B} \underline{\mathbf{g}}^e \hat{\mathbf{S}}^e \quad (3.1)$$

$$\hat{H}_{Zeeman}^h = \frac{\mu_B}{\hbar} \mathbf{B} \underline{\mathbf{g}}^h \hat{\mathbf{S}}^h, \quad (3.2)$$

where μ_B is the Bohr magneton, \mathbf{B} is the effective magnetic field and $\underline{\mathbf{g}}^e$ ($\underline{\mathbf{g}}^h$) is the electron (hole) g tensor, which determines the coupling strength between the magnetic field and the spin. $\hat{\mathbf{S}}^e = \hbar/2(\hat{\mathbf{e}}_x \hat{\sigma}_x^e + \hat{\mathbf{e}}_y \hat{\sigma}_y^e + \hat{\mathbf{e}}_z \hat{\sigma}_z^e)$ ($\hat{\mathbf{S}}^h = \hbar/2(\hat{\mathbf{e}}_x \hat{\sigma}_x^h + \hat{\mathbf{e}}_y \hat{\sigma}_y^h + \hat{\mathbf{e}}_z \hat{\sigma}_z^h)$) is the spin operator of the electron (hole). In the case where the g tensors are orthogonal, the Hamiltonians can be written as

$$\hat{H}_{Zeeman}^e = \frac{\mu_B}{2} (B_x g_x^e \sigma_x^e + B_y g_y^e \sigma_y^e + B_z g_z^e \sigma_z^e) \quad (3.3)$$

$$\hat{H}_{Zeeman}^h = \frac{\mu_B}{2} (B_x g_x^h \sigma_x^h + B_y g_y^h \sigma_y^h + B_z g_z^h \sigma_z^h). \quad (3.4)$$

In case of the electron, a spin half particle, the spin operators are the three Pauli spin operators

$$\sigma_x^e = \begin{pmatrix} 0 & 1 \\ 1 & 0 \end{pmatrix}, \quad \sigma_y^e = \begin{pmatrix} 0 & -i \\ i & 0 \end{pmatrix}, \quad \sigma_z^e = \begin{pmatrix} 1 & 0 \\ 0 & -1 \end{pmatrix}. \quad (3.5)$$

Defining the spin operator, $\hat{\mathbf{S}}^h$, for a hole is more troublesome. Recall the effective mass description where we deconstruct the hole into 3 parts: heavy hole with, light hole and spin-orbit split-off and note that heavy hole has a different projection of

the total angular momentum than the other three parts. This leads to an important feature of the hole Zeeman interaction: the anisotropy of the hole g factor. In the case of a pure heavy hole state, the in-plane g factor is zero, since the total angular momentum lies exclusively in the z-direction. In reality, however, band-mixing occurs for several reasons such as strain, dot size, applied electric field, total magnetic field and the indium concentration [27]-[31]. Consequently, the hole g factor becomes anisotropic due to the complex spin structure and varies from dot to dot, since it depends on the particular dot properties. For completeness we should mention, that the band-mixing of the holes and their admixture to the electron band induces an anisotropy of the electron g factor, though not significant [32].

Some examples of observed g factor values for InAs quantum dots in the in-plane x-direction are [27]-[30]

$$0.35 < |g_x^e| < 1.9, \quad 0.06 < |g_x^h| < 0.14 \quad (3.6)$$

In this thesis, we chose to label $g_x^e = 0.5$ and $g_x^h = 0.08$ as "typical" values.

Optical Transitions

Since the magnetic field is in the in-plane x-direction in fig. 3.1, all four optical transition between all four spin eigenstates are allowed. Vertical transitions are x-polarised light while diagonal transitions are y-polarised. Ideally, the vertical and diagonal transitions are equally strong but often the band-mixing will soften the selection rules. To some extent, it is possible to manipulate the selection rules via the external magnetic field utilising the anisotropy of the g factor. Another possibility is to embed the quantum dot in a nanostructure to control the optical transitions. We discuss this possibility further in section 3.2. Both spin-photon entanglement protocols rely on control of the optical transitions, as we shall see, each in their own way.

3.1.3 Hyperfine Interactions and Spin Coherence

As stated in section 3.1, a quantum dot consists of 10^4 - 10^6 atoms, so even though the dot is singly charged and has a central spin it is crucial to consider the nuclear spin bath dynamics within the quantum dot. The confined spin interacts with the spin of the nuclear bath via the hyperfine interaction which limits the coherence time of the confined spin. In this section we shall describe the hyperfine interaction, introduce the important Overhauser field, discuss the difference between holes and electrons in this context and finally present some observed values of the time-averaged spin coherence time T_2^* .

The hyperfine interaction can be divided into two main contributions: Fermi contact interaction and dipole-dipole interaction, the first being dominant for electrons and the second dominant for holes. The different nature of the hyperfine interactions for electrons and holes is primarily caused by the orbital differences. Electrons have s-orbitals (zero angular momentum) resulting in a large physical overlap between the electron wavefunction and the nuclei. Hence, the Fermi contact interaction is dominant for electrons. On the other hand, the wavefunction of the hole is p-type (non-zero angular momentum) such that the dipole-dipole interaction becomes dominant because the wave function is approximately zero at the position of the nuclei (see fig. 3.3).

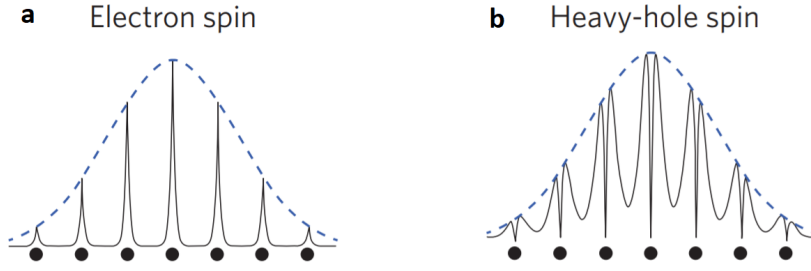


FIGURE 3.3: Schematic illustration of the difference in the hyperfine interaction with the nuclear spins of electron and holes. The electron wavepacket is primarily centralised at the position of the nuclei (black dots) while the wavepacket of the heavy hole is decentralised. The illustration is taken from [24].

The electron spin Fermi-contact interaction with the nuclear spin bath and the hole dipole-dipole interaction with the nuclear spin bath can be described, respectively, by the Hamiltonians [33]

$$\hat{H}_{fc}^e = \frac{\nu_0}{2} \sum_j A_j^e |\psi(\mathbf{r}_j)|^2 \left(\hat{I}_z^j S_z^e + \frac{1}{2} [\hat{I}_+^j \hat{S}_-^e + \hat{I}_-^j \hat{S}_+^e] \right) \quad (3.7)$$

$$\hat{H}_{dip}^h = \nu_0 \sum_j \frac{A_j^h}{1 + \beta^2} |\psi(\mathbf{r}_j)|^2 \left(\hat{I}_z^j S_z^e + \frac{\alpha}{2} [\hat{I}_+^j \hat{S}_-^e + \hat{I}_-^j \hat{S}_+^e] \right), \quad (3.8)$$

where ν_0 is the InAs unit cell volume, \mathbf{r}_j is the position of the j 'th nuclei with spin \hat{I}^j . The operators \hat{S}_\pm are spin operators acting on the confined spin, $\psi(\mathbf{r}_j)$ is the normalised envelope function of the confined spin, A_j^e and A_j^h are the constants of the hyperfine interaction and the parameters α and β quantify the amount of hole-mixing. To say something analytically about the hyperfine interaction Hamiltonians (3.7) and (3.8) we introduce the averaged hyperfine constants \bar{A}^e and \bar{A}^h for the Fermi contact and dipole-dipole interaction, respectively. Assuming moderate heavy hole-light hole mixing and uniform wavefunctions $\psi(\mathbf{r}) = \sqrt{2/N\nu_0}$, (3.7) and (3.8) respectively simplifies to

$$\hat{H}_{fc}^e = \frac{2\bar{A}^e}{N} \left(\hat{I}_z S_z^e + \frac{1}{2} (\hat{I}_+ \hat{S}_-^e + \hat{I}_- \hat{S}_+^e) \right) \quad (3.9)$$

$$\hat{H}_{dip}^h = \frac{2\bar{A}^h}{N} \left(\hat{I}_z S_z^e + \alpha \left[\frac{\hat{I}_+ \hat{S}_-^h + \hat{I}_- \hat{S}_+^h}{2} \right] \right). \quad (3.10)$$

Two important features of the averaged interaction Hamiltonians should be highlighted. Firstly, the ratio $|\bar{A}^h|/\bar{A}^e$ has been theoretically predicted [34] and later experimentally demonstrated [35, 36] to be ~ 0.1 . Hence we expect the coherence time of the hole to be larger than the corresponding coherence time of the electron. Secondly, the dipole-dipole interaction depends, like the Zeeman effect, on hole-mixing. The amplitude α of the spin-flip term is defined such that $\alpha = 0$ if the hole is a pure heavy hole. In this limit, only the z -component couples to the nuclear spin bath while any hole-mixing will result in an in-plane coupling as well. This shows that the coherence time of the hole, like the g factor, depends on the particular dot properties.

Returning to (3.7) and (3.8). Since the sums run over all 10^4 - 10^6 lattice sites, all

simultaneously interacting with the confined spin, we may preform a mean field approximation and write the interaction as an effective magnetic field. This field is known as the Overhauser field. In this thesis, we model the Overhauser field semi-classically. Assuming the magnetic field to be semi-classical and Gaussian distributed, the Overhauser field has the following property

$$\rho \propto \exp\left(\frac{B_z^2}{2\delta B_{\parallel}^2}\right) \exp\left(\frac{B_x^2 + B_y^2}{2\delta B_{\perp}^2}\right) \quad (3.11)$$

where δB_{\parallel} and δB_{\perp} represent the nuclear fluctuations parallel and orthogonal to the z-direction, respectively. The two terms are necessary in order to account for the strong hole g factor anisotropy. Note that a pure heavy hole would only experience the component along the z-direction. For an electron we could collect the contributions into a single distribution since the dephasing is, to a good approximation, isotropic. If the quantum dot is subjected to a strong external magnetic field, the components of the Overhauser field perpendicular to the applied field are negligible since the strength of the Overhauser field is in the order of 20 mT [24] and hence suppressed to first order. The component parallel to the applied field is, however, not suppressed and is the limiting effect of the coherence time of the confined spin since these magnetic field fluctuations result in a random change in the precession frequency of the confined spin. For an electron, the dephasing time T_2^* is typically a few nanoseconds [19, 43] which, as we shall see later, is a serious problem when applying electrons to realise the spin-photon entanglement protocols. The coherence time of the hole is, as expected, larger and becomes increasingly larger with increasing in-plane magnetic field [34] since the fluctuations along the field become increasingly suppressed - especially for a pure heavy-hole state. A T_2^* a factor of 10 larger than that of an electron is realistic.

3.2 Nanophotonic Waveguides

It should by now be clear why quantum dots can be effective systems for creating spin-photon entanglement. If we wish to fully utilise them as reliable single-photon sources in our protocols, we need a way to tailor the properties of the quantum dot to our specific purpose. A nanophotonic waveguide allows, in principle, to do exactly that by enhancing light-matter interaction. In particular, it gives control over the dipole-dipole interaction between the quantum dot and the photons. Fig. 3.4 shows an example of a nanophotonic waveguide: a nanobeam waveguide. For further discussion on photonic waveguides see [23], upon which section 3.2.1 is also based.



FIGURE 3.4: Scanning electron microscope image of a GaAs nanobeam waveguide embedded with a quantum dot and suspended in air. The gratings in the ends of the waveguide scatter light in the z-direction. Due to the high difference in refractive index between GaAs ($n \sim 3.5$) and air ($n \sim 1$) the mode of an emitted photon is confined to modes travelling along the waveguide. These modes are referred to as *waveguide modes*.

3.2.1 Purcell Enhancement and the β Factor

The mode density of the waveguide mode, which is interacting with the dipole emitter, is described by the projected local density of state (LDOS)

$$\rho(\mathbf{r}, \omega, \hat{\mathbf{e}}_{\mathbf{d}}) = \frac{a}{\pi v_g} \frac{f(\mathbf{r})}{\epsilon(\mathbf{r}) V_{eff}} |\hat{\mathbf{e}}_{\mathbf{k}}^*(\mathbf{r}) \cdot \hat{\mathbf{e}}_{\mathbf{d}}|^2, \quad (3.12)$$

where a is the lattice constant, v_g is the group velocity, V_{eff} is the effective mode volume per unit cell and $f(\mathbf{r}) = \epsilon(\mathbf{r}) |\mathbf{b}_k(\mathbf{r})|^2 V_{eff}$, where $\epsilon(\mathbf{r})$ is the permittivity at position \mathbf{r} and \mathbf{b}_k is a 1D periodic function along the waveguide, is a scalar between 0 and 1 which quantifies the spatial mismatch between the quantum dot and the waveguide mode field maximum. If $f(\mathbf{r}) = 1$, the quantum dot is optimally positioned on an antinode of the waveguide mode. Lastly, the quantity $|\hat{\mathbf{e}}_{\mathbf{k}}^*(\mathbf{r}) \cdot \hat{\mathbf{e}}_{\mathbf{d}}|^2$ quantifies the alignment of the electric field of the waveguide mode, $\hat{\mathbf{e}}_{\mathbf{k}}$ is the unit vector of this electric field with respect to the dipole $\hat{\mathbf{e}}_{\mathbf{d}}$.

For a quantum dot with the transition dipole moment \mathbf{d} , a transition frequency ω_0 between the ground state and excited state, and a spatial position \mathbf{r}_0 , the LDOS is related to the spontaneous emission rate given a Markov approximation. The spontaneous emission rate is then defined by:

$$\gamma_{rad}(\mathbf{r}_0, \omega_0, \mathbf{d}) = \frac{\pi d^2}{\epsilon_0 \hbar} \rho(\mathbf{r}_0, \omega_0, \hat{\mathbf{e}}_{\mathbf{d}}), \quad (3.13)$$

where ϵ_0 is the vacuum permittivity. Equation (3.13) represents the essence of this section: by alternating the LDOS we can control the spontaneous emission. Not only can the spontaneous emission rate be enhanced by lowering the group velocity of the light, we can tailor the mode of the emitted photon by strategical placement of the quantum dot and orientation of the dipole moments. In effect, we can address the vertical and diagonal optical transitions of fig. 3.1 separately and control the branching ratio of the decay. The increase in decay rate can be quantified by the Purcell factor, defined as

$$F_p(\mathbf{r}, \omega, \hat{\mathbf{e}}_{\mathbf{d}}) = \frac{\gamma_{rad}(\mathbf{r}_0, \omega_0, \mathbf{d})}{\gamma_{rad}^{hom}(\omega)}, \quad (3.14)$$

which represents the ratio between the decay rate of an emitter in the tailored environment and the same emitter in a homogeneous environment where the decay rate is typically $\gamma_{rad}^{hom}(\omega) \approx 1 \text{ ns}^{-1}$. A Purcell Factor of $F_p = 5.2$ has been observed for a GaAs waveguide embedded with a InGaAs quantum dot corresponding to a decay rate of 5.7 ns^{-1} . This value shall become impotent later.

This section is concluded by another quantification of the advantages achievable by waveguides: the control of the mode of the emitted photon, i.e. enhancement of probability of emitting a photon into the mode of the waveguide which is a necessity to archive a high collection efficiency of the photons. The β factor is defined as the rate of photons spontaneous emitted into the waveguide mode γ_{wg} relative to the overall spontaneous emission rate γ

$$\beta = \frac{\gamma_{wg}}{\gamma_{wg} + \gamma}. \quad (3.15)$$

Experiments have reported $\beta = 98.4\%$. We shall return to this number when we consider the effect of loss on the time-bin entanglement protocol in section 6.2.

Chapter 4

Four Level System

In this section we solve the Schrödinger equation

$$i\frac{\partial}{\partial t} |\psi(t)\rangle = \hat{H} |\psi(t)\rangle, \quad (4.1)$$

for a isolated spin in a quantum dot in the Voigt geometry, which can be excited by absorption of a photon and decay by spontaneous emission of a photon corresponding to the four level diagram shown in fig. 3.1. The only difference between the Hamiltonian describing a singly charged quantum dot with either an electron or a hole, is the sign of the Zeeman splitting. We chose to solve the Schrödinger equation for an electron but note that the solution applies equally well to a hole, if we simply change the sign of the ground state splitting and the splitting of the excited state δ_g and δ_e , respectively .

4.1 The Hamiltonian

In this section, the Hamiltonian of the system is presented. In order to simplify the equations in this chapter, the applied notation is first presented. As mentioned above, the only difference in the equations of motion for an electron and a hole is the sign of the Zeeman splitting, so it is not important to distinguish these states in the notation. Throughout this thesis, we denote the ground state $|\uparrow\rangle$ and $|\downarrow\rangle$ and the excited trion state as $|\uparrow\rangle$ and $|\downarrow\rangle$ independent of the choice of confined spin. Furthermore, we omit the tensor product when we combine Hilbert spaces, i.e. we define $|\psi\rangle_A \otimes |\phi\rangle_b \otimes \dots \equiv |\psi, \phi, \dots\rangle$.

We shall assume Markovian dynamics and under the rotating wave approximation the total Hamiltonian in k-space is

$$\hat{H} = \hat{H}_0 + \hat{H}_{Zeeman} + \hat{H}_{field} + \hat{H}_{int}, \quad (4.2)$$

where

$$\hat{H}_0 = \omega_0 (|\uparrow\rangle \langle\uparrow| + |\downarrow\rangle \langle\downarrow|) \quad (4.3)$$

$$\hat{H}_{Zeeman} = \frac{\delta_e}{2} (|\uparrow\rangle \langle\uparrow| - |\downarrow\rangle \langle\downarrow|) + \frac{\delta_g}{2} (|\downarrow\rangle \langle\downarrow| - |\uparrow\rangle \langle\uparrow|) \quad (4.4)$$

$$\hat{H}_{field} = \sum_k \omega_k (\hat{a}_{k,y}^\dagger \hat{a}_{k,y} + \hat{a}_{k,x}^\dagger \hat{a}_{k,x}) \quad (4.5)$$

$$\begin{aligned} \hat{H}_{int} = \sum_k g_k & (|\uparrow\rangle \langle\uparrow| \hat{a}_{k,x} + |\downarrow\rangle \langle\uparrow| \hat{a}_{k,y} + |\downarrow\rangle \langle\downarrow| \hat{a}_{k,x} + |\uparrow\rangle \langle\downarrow| \hat{a}_{k,y} \\ & + |\uparrow\rangle \langle\uparrow| \hat{a}_{k,x}^\dagger + |\uparrow\rangle \langle\downarrow| \hat{a}_{k,y}^\dagger + |\downarrow\rangle \langle\downarrow| \hat{a}_{k,x}^\dagger + |\downarrow\rangle \langle\uparrow| \hat{a}_{k,y}^\dagger). \end{aligned} \quad (4.6)$$

In (4.3), \hat{H}_0 is the bare spin Hamiltonian. In (4.4), \hat{H}_{Zeeman} is the Zeeman Hamiltonian written in a eigenbasis of the magnetic field. In (4.5), \hat{H}_{field} is the freely propagating photon field Hamiltonian where $\hat{a}_{k,i}^\dagger$ ($\hat{a}_{k,i}$) is the creation (annihilation) photon operator for a mode with wavenumber k and polarisation i ($i = x, y$). The frequency ω_k is the frequency of the free field photon, which we shall assume to be close to the transition frequency between the ground state and excited state, such that linear dissipation holds true for the free field photons: $\omega_k = v_g|k|$. In (4.6), \hat{H}_{int} is the spin-photon interaction Hamiltonian with coupling constant g_k for the k 'th mode.

We proceed by Fourier transforming the photonic operators to real-space. This will prove useful later when we solve the equations of motion if we assume the quantum dot to be 0 dimensional, i.e. a Dirac delta function in space.

The two Hamiltonian involving photonic operators, \hat{H}_{field} and \hat{H}_{int} , Fourier transform to real space as

$$\mathcal{F}[\hat{H}_{field}] = iv_g \int_{-\infty}^{\infty} dz \left(\frac{\partial \hat{a}_y^\dagger(z)}{\partial z} \hat{a}_y(z) + \frac{\partial \hat{a}_x^\dagger(z)}{\partial z} \hat{a}_x(z) \right) \quad (4.7)$$

$$\begin{aligned} \mathcal{F}[\hat{H}_{int}] = g \int_{-\infty}^{\infty} dz \delta(z) & \left(e^{-ik_0 z} (|\uparrow\rangle \langle \uparrow| \hat{a}_x(z) + |\downarrow\rangle \langle \uparrow| \hat{a}_y(z) \right. \\ & + |\downarrow\rangle \langle \downarrow| \hat{a}_x(z) + |\uparrow\rangle \langle \downarrow| \hat{a}_y(z)) + e^{ik_0 z} (|\uparrow\rangle \langle \uparrow| \hat{a}_x^\dagger(z) \\ & \left. + |\uparrow\rangle \langle \downarrow| \hat{a}_y^\dagger(z) + |\downarrow\rangle \langle \downarrow| \hat{a}_x^\dagger(z) + |\downarrow\rangle \langle \uparrow| \hat{a}_y^\dagger(z)) \right), \end{aligned} \quad (4.8)$$

where v_g is the group velocity of the emitted photon wave-packet and $k_0 = \omega_0/v_g$. As mentioned above, it is assumed that the quantum dot have no spatial extend which means that there is only a dipole interaction at $z = 0$ where the quantum dot is located. (4.7) is calculated by partial integration and imposing that the probability of measuring a photon at the boundary should be zero.

The total Fourier transformed Hamiltonian is denoted \hat{H} and can now be defined as:

$$\begin{aligned} \hat{H} = & \omega_0 (|\uparrow\rangle \langle \uparrow| + |\downarrow\rangle \langle \downarrow|) + \frac{\delta_e}{2} (|\uparrow\rangle \langle \uparrow| - |\downarrow\rangle \langle \downarrow|) + \frac{\delta_g}{2} (|\downarrow\rangle \langle \downarrow| - |\uparrow\rangle \langle \uparrow|) \\ & + iv_g \int_{-\infty}^{\infty} dz \left(\frac{\partial a_y^\dagger(z)}{\partial z} a_y(z) + \frac{\partial a_x^\dagger(z)}{\partial z} a_x(z) \right) \\ & + g \int_{-\infty}^{\infty} dz \delta(z) \left(e^{-ik_0 z} (|\uparrow\rangle \langle \uparrow| \hat{a}_x(z) + |\downarrow\rangle \langle \uparrow| \hat{a}_y(z) \right. \\ & + |\downarrow\rangle \langle \downarrow| \hat{a}_x(z) + |\uparrow\rangle \langle \downarrow| \hat{a}_y(z)) + e^{ik_0 z} (|\uparrow\rangle \langle \uparrow| \hat{a}_x^\dagger(z) \\ & \left. + |\uparrow\rangle \langle \downarrow| \hat{a}_y^\dagger(z) + |\downarrow\rangle \langle \downarrow| \hat{a}_x^\dagger(z) + |\downarrow\rangle \langle \uparrow| \hat{a}_y^\dagger(z)) \right) \end{aligned} \quad (4.9)$$

4.2 Wavefunction

In order to solve the Schrödinger equation, it is necessary to apply a suitable ansatz for the wavefunction. In this system, six contributions contribute to the wavefunction: $c_\downarrow(t)$ and $c_\uparrow(t)$, which is the probability of being in the excited state with spin down and spin up, respectively, at time t . The four ground state coefficients are $\phi(t_e, t)_{\uparrow,x}$, $\phi(t_e, t)_{\uparrow,y}$, $\phi(t_e, t)_{\downarrow,x}$ and $\phi(t_e, t)_{\downarrow,y}$ which are the probabilities of being in the ground

state with spin up or down while a photon was emitted at time t_e with polarisation x or y . The wavefunction becomes

$$\begin{aligned} |\Psi(t)\rangle &= c_{\uparrow}(t)e^{-i\omega_0 t} |\uparrow, 0\rangle + c_{\downarrow}(t)e^{-i\omega_0 t} |\downarrow, 0\rangle \\ &+ \sqrt{v_g} \int dt_e \left(\phi(t_e, t)_{\uparrow, x} \hat{a}_x^\dagger(z_0) |\uparrow, 0\rangle + \phi(t_e, t)_{\uparrow, y} \hat{a}_y^\dagger(z_0) |\uparrow, 0\rangle \right. \\ &\left. + \phi(t_e, t)_{\downarrow, x} \hat{a}_x^\dagger(z_0) |\downarrow, 0\rangle + \phi(t_e, t)_{\downarrow, y} \hat{a}_y^\dagger(z_0) |\downarrow, 0\rangle \right). \end{aligned} \quad (4.10)$$

4.3 Schrödinger Equation

In order to solve the Schrödinger equation, see (4.1), several steps have to be applied. First, the left- and right-hand side of the Schrödinger are evaluated separately. In the second step, the two expressions are set equal to each other so six coupled differential equations are determined. The third step is to solve these coupled differential equations by applying a Laplace transformation and impose boundary conditions. Finally, an inverse Laplace transformation can be made and the coefficients for the excited states can be determined and thus also determine the coefficients for the ground states.

First, the time-derivative of the wave function is determined:

$$\begin{aligned} \frac{\partial}{\partial t} |\psi(t)\rangle &= (\dot{c}_{\uparrow}(t) - i\omega_0 c_{\uparrow}(t))e^{-i\omega_0 t} |\uparrow, 0\rangle + (\dot{c}_{\downarrow}(t) - i\omega_0 c_{\downarrow}(t))e^{-i\omega_0 t} |\downarrow, 0\rangle \\ &+ \sqrt{v_g} \int dt_e \left(\dot{\phi}(t_e, t)_{\uparrow, x} \hat{a}_x^\dagger(z_0) |\uparrow, 0\rangle + \dot{\phi}(t_e, t)_{\uparrow, y} \hat{a}_y^\dagger(z_0) |\uparrow, 0\rangle \right. \\ &\left. + \dot{\phi}(t_e, t)_{\downarrow, x} \hat{a}_x^\dagger(z_0) |\downarrow, 0\rangle + \dot{\phi}(t_e, t)_{\downarrow, y} \hat{a}_y^\dagger(z_0) |\downarrow, 0\rangle \right). \end{aligned} \quad (4.11)$$

The right-hand side of (4.1) is evaluated by allowing the Fourier transformed Hamiltonian (4.9) to operate on the wave function (4.10)

$$\begin{aligned}
\hat{H} |\psi(t)\rangle &= \omega_0 c_{\uparrow}(t) e^{-i\omega_0 t} |\uparrow, 0\rangle + \omega_0 c_{\downarrow}(t) e^{i\omega_0 t} |\downarrow, 0\rangle + \frac{\delta_e}{2} c_{\uparrow}(t) e^{-i\omega_0 t} |\uparrow, 0\rangle \\
&\quad - \frac{\delta_e}{2} c_{\downarrow}(t) e^{i\omega_0 t} |\downarrow, 0\rangle - \frac{\delta_g}{2} \sqrt{v_g} \int dt e(\phi(t_e, t)_{\uparrow, x} \hat{a}_x^\dagger(z_0) |\uparrow, 0\rangle \\
&\quad + \phi(t_e, t)_{\uparrow, y} \hat{a}_y^\dagger(z_0) |\uparrow, 0\rangle - \phi(t_e, t)_{\downarrow, x} \hat{a}_x^\dagger(z_0) |\downarrow, 0\rangle - \phi(t_e, t)_{\downarrow, y} \hat{a}_y^\dagger(z_0) |\downarrow, 0\rangle) \\
&\quad + i v_g^{3/2} \int_{-\infty}^{\infty} dz \int dt_e \left(\frac{\partial \hat{a}_y^\dagger(z)}{\partial z} \hat{a}_y(z) + \frac{\partial \hat{a}_x^\dagger(z)}{\partial z} \hat{a}_x(z) \right) \\
&\quad (\phi(t_e, t)_{\uparrow, x} \hat{a}_x^\dagger(z_0) |\uparrow, 0\rangle + \phi(t_e, t)_{\uparrow, y} \hat{a}_y^\dagger(z_0) |\uparrow, 0\rangle \\
&\quad + \phi(t_e, t)_{\downarrow, x} \hat{a}_x^\dagger(z_0) |\downarrow, 0\rangle + \phi(t_e, t)_{\downarrow, y} \hat{a}_y^\dagger(z_0) |\downarrow, 0\rangle) \tag{4.12} \\
&\quad + g \sqrt{v_g} \int_{-\infty}^{\infty} dz \int dt_e \delta(z_0) e^{-ik_0 z} (\phi(t_e, t)_{\uparrow, x} \hat{a}_x(z) \hat{a}_x^\dagger(z_0) |\uparrow, 0\rangle \\
&\quad + \phi(t_e, t)_{\uparrow, x} \hat{a}_y(z) \hat{a}_x^\dagger(z_0) |\downarrow, 0\rangle + \phi(t_e, t)_{\uparrow, y} \hat{a}_x(z) \hat{a}_y^\dagger(z_0) |\uparrow, 0\rangle \\
&\quad + \phi(t_e, t)_{\uparrow, y} \hat{a}_y(z) \hat{a}_y^\dagger(z_0) |\downarrow, 0\rangle + \phi(t_e, t)_{\downarrow, x} \hat{a}_x(z) \hat{a}_x^\dagger(z_0) |\downarrow, 0\rangle \\
&\quad + \phi(t_e, t)_{\downarrow, x} \hat{a}_y(z) \hat{a}_x^\dagger(z_0) |\uparrow, 0\rangle + \phi(t_e, t)_{\downarrow, y} \hat{a}_x(z) \hat{a}_y^\dagger(z_0) |\downarrow, 0\rangle \\
&\quad + \phi(t_e, t)_{\downarrow, y} \hat{a}_y(z) \hat{a}_y^\dagger(z_0) |\uparrow, 0\rangle) \\
&\quad + g \int_{-\infty}^{\infty} dz \delta(z_0) e^{-i\omega_0 t + ik_0 z} (c_{\uparrow} \hat{a}_x^\dagger(z) |\uparrow, 0\rangle + c_{\uparrow} \hat{a}_y^\dagger(z) |\downarrow, 0\rangle \\
&\quad + c_{\downarrow} \hat{a}_x^\dagger(z) |\downarrow, 0\rangle + c_{\downarrow} \hat{a}_y^\dagger(z) |\uparrow, 0\rangle).
\end{aligned}$$

The expressions for the left- and right-hand side of the Schrödinger in (4.11) and (4.12) are now set equal to each other. By multiplying with $\langle \uparrow, 0 |$, $\langle \downarrow, 0 |$, $\langle \uparrow, 0 | \hat{a}_x(z)$, $\langle \uparrow, 0 | \hat{a}_y(z)$, $\langle \downarrow, 0 | \hat{a}_x(z)$, and $\langle \downarrow, 0 | \hat{a}_y(z)$ we obtain a set of six coupled differential equations. Respectively:

$$\dot{c}_{\uparrow}(t) = -i \frac{\delta_e}{2} c_{\uparrow}(t) - i \frac{g}{\sqrt{v_g}} \phi(t_e, t)_{\uparrow, x} - i \frac{g}{\sqrt{v_g}} \phi(t_e, t)_{\downarrow, y} \tag{4.13}$$

$$\dot{c}_{\downarrow}(t) = i \frac{\delta_e}{2} c_{\downarrow}(t) - i \frac{g}{\sqrt{v_g}} \phi(t_e, t)_{\uparrow, y} - i \frac{g}{\sqrt{v_g}} \phi(t_e, t)_{\downarrow, x} \tag{4.14}$$

$$\dot{\phi}(t_e, t)_{\uparrow, x} = i \frac{\delta_g}{2} \phi(t_e, t)_{\uparrow, x} - i \frac{g}{\sqrt{v_g}} c_{\uparrow}(t) \delta(t - t_e) \tag{4.15}$$

$$\dot{\phi}(t_e, t)_{\uparrow, y} = i \frac{\delta_g}{2} \phi(t_e, t)_{\uparrow, y} - i \frac{g}{\sqrt{v_g}} c_{\downarrow}(t) \delta(t - t_e) \tag{4.16}$$

$$\dot{\phi}(t_e, t)_{\downarrow, x} = -i \frac{\delta_g}{2} \phi(t_e, t)_{\downarrow, x} - i \frac{g}{\sqrt{v_g}} c_{\downarrow}(t) \delta(t - t_e) \tag{4.17}$$

$$\dot{\phi}(t_e, t)_{\downarrow, y} = -i \frac{\delta_g}{2} \phi(t_e, t)_{\downarrow, y} - i \frac{g}{\sqrt{v_g}} c_{\uparrow}(t) \delta(t - t_e). \tag{4.18}$$

To solve this set of six coupled differential equations we Laplace transform (4.13)-(4.18) to obtain a set of six coupled algebraic equations. The boundary conditions of the system are defined using the requirement that the system is in the excited state with spin up at time $t=0$. This means: $c_{\uparrow}(t=0) = 1$ and the additional five

coefficients being 0 at time $t=0$. The Laplace transformed equations are now:

$$\begin{aligned}\mathcal{L}[\dot{c}_{\uparrow}(t)](s) &= s\bar{c}_{\uparrow}(s) - c_{\uparrow}(t=0) \\ &= -i\frac{\delta_e}{2}\bar{c}_{\uparrow}(s) - i\frac{g}{\sqrt{v_g}}\bar{\phi}(t_e, s)_{\uparrow, x} - i\frac{g}{\sqrt{v_g}}\bar{\phi}(t_e, s)_{\downarrow, y} \\ \Rightarrow 1 &= s\bar{c}_{\uparrow}(s) - i\frac{\delta_e}{2}\bar{c}_{\uparrow}(s) + i\frac{g}{\sqrt{v_g}}\bar{\phi}(t_e, s)_{\uparrow, x} + i\frac{g}{\sqrt{v_g}}\bar{\phi}(t_e, s)_{\downarrow, y}\end{aligned}\quad (4.19)$$

$$\begin{aligned}\mathcal{L}[\dot{c}_{\downarrow}(t)](s) &= s\bar{c}_{\downarrow}(s) - c_{\downarrow}(t=0) \\ &= -i\frac{\delta_e}{2}\bar{c}_{\downarrow}(s) - i\frac{g}{\sqrt{v_g}}\bar{\phi}(t_e, s)_{\uparrow, y} - i\frac{g}{\sqrt{v_g}}\bar{\phi}(t_e, s)_{\downarrow, x} \\ \Rightarrow 0 &= -s\bar{c}_{\downarrow}(s) - i\frac{\delta_e}{2}\bar{c}_{\downarrow}(s) - i\frac{g}{\sqrt{v_g}}\bar{\phi}(t_e, s)_{\uparrow, y} - i\frac{g}{\sqrt{v_g}}\bar{\phi}(t_e, s)_{\downarrow, x}\end{aligned}\quad (4.20)$$

$$\begin{aligned}\mathcal{L}[\dot{\phi}(t_e, t)_{\uparrow, x}](s) &= s\bar{\phi}(t_e, s)_{\uparrow, x} - \phi(t_e, t=0)_{\uparrow, x} \\ &= i\frac{\delta_g}{2}\bar{\phi}(t_e, s)_{\uparrow, x} - i\frac{g}{\sqrt{v_g}}e^{-t_e s}\theta(t-t_e)c_{\uparrow}(t_e) \\ \Rightarrow 0 &= -s\bar{\phi}(t_e, s)_{\uparrow, x} + i\frac{\delta_g}{2}\bar{\phi}(t_e, s)_{\uparrow, x} - i\frac{g}{\sqrt{v_g}}e^{-t_e s}\theta(t-t_e)c_{\uparrow}(t_e)\end{aligned}\quad (4.21)$$

$$\begin{aligned}\mathcal{L}[\dot{\phi}(t_e, t)_{\uparrow, y}](s) &= s\bar{\phi}(t_e, s)_{\uparrow, y} - \phi(t_e, t=0)_{\uparrow, y} \\ &= i\frac{\delta_g}{2}\bar{\phi}(t_e, s)_{\uparrow, y} - i\frac{g}{\sqrt{v_g}}e^{-t_e s}\theta(t-t_e)c_{\downarrow}(t_e) \\ \Rightarrow 0 &= -s\bar{\phi}(t_e, s)_{\uparrow, y} + i\frac{\delta_g}{2}\bar{\phi}(t_e, s)_{\uparrow, y} - i\frac{g}{\sqrt{v_g}}e^{-t_e s}\theta(t-t_e)c_{\downarrow}(t_e)\end{aligned}\quad (4.22)$$

$$\begin{aligned}\mathcal{L}[\dot{\phi}(t_e, t)_{\downarrow, x}](s) &= s\bar{\phi}(t_e, s)_{\downarrow, x} - \phi(t_e, t=0)_{\downarrow, x} \\ &= -i\frac{\delta_g}{2}\bar{\phi}(t_e, s)_{\downarrow, x} - i\frac{g}{\sqrt{v_g}}e^{-t_e s}\theta(t-t_e)c_{\downarrow}(t_e) \\ \Rightarrow 0 &= -s\bar{\phi}(t_e, s)_{\downarrow, x} - i\frac{\delta_g}{2}\bar{\phi}(t_e, s)_{\downarrow, x} - i\frac{g}{\sqrt{v_g}}e^{-t_e s}\theta(t-t_e)c_{\downarrow}(t_e)\end{aligned}\quad (4.23)$$

$$\begin{aligned}\mathcal{L}[\dot{\phi}(t_e, t)_{\downarrow, y}](s) &= s\bar{\phi}(t_e, s)_{\downarrow, y} - \phi(t_e, t=0)_{\downarrow, y} \\ &= -i\frac{\delta_g}{2}\bar{\phi}(t_e, s)_{\downarrow, y} - i\frac{g}{\sqrt{v_g}}e^{-t_e s}\theta(t-t_e)c_{\uparrow}(t_e) \\ \Rightarrow 0 &= -s\bar{\phi}(t_e, s)_{\downarrow, y} - i\frac{\delta_g}{2}\bar{\phi}(t_e, s)_{\downarrow, y} - i\frac{g}{\sqrt{v_g}}e^{-t_e s}\theta(t-t_e)c_{\uparrow}(t_e).\end{aligned}\quad (4.24)$$

The four ground states can now be isolated using the expressions in (4.13)-(4.18) which yields:

$$\bar{\phi}(t_e, s)_{\uparrow, x} = \frac{g}{\sqrt{v_g}} \frac{e^{-st_e}}{s + \delta_g} \theta(t-t_e) c_{\uparrow}(t_e) \quad (4.25)$$

$$\bar{\phi}(t_e, s)_{\uparrow, y} = \frac{g}{\sqrt{v_g}} \frac{e^{-st_e}}{s + \delta_g} \theta(t-t_e) c_{\downarrow}(t_e) \quad (4.26)$$

$$\bar{\phi}(t_e, s)_{\downarrow, x} = \frac{g}{\sqrt{v_g}} \frac{e^{-st_e}}{s - \delta_g} \theta(t-t_e) c_{\downarrow}(t_e) \quad (4.27)$$

$$\bar{\phi}(t_e, s)_{\downarrow, y} = \frac{g}{\sqrt{v_g}} \frac{e^{-st_e}}{s - \delta_g} \theta(t-t_e) c_{\uparrow}(t_e), \quad (4.28)$$

where $\theta(t - t_e)$ is a Heaviside step function ensuring that the states only exist after emission of a photon. Performing an inverse Laplace transformation on (4.25)-(4.28) yields

$$\phi(t_e, t)_{\uparrow, x} = \frac{g}{\sqrt{v_g}} e^{-\frac{\delta_e}{2}(t-t_e)} \theta(t - t_e) c_{\uparrow}(t_e) \quad (4.29)$$

$$\phi(t_e, t)_{\uparrow, y} = \frac{g}{\sqrt{v_g}} e^{-\frac{\delta_e}{2}(t-t_e)} \theta(t - t_e) c_{\downarrow}(t_e) \quad (4.30)$$

$$\phi(t_e, t)_{\downarrow, x} = \frac{g}{\sqrt{v_g}} e^{\frac{\delta_e}{2}(t-t_e)} \theta(t - t_e) c_{\downarrow}(t_e) \quad (4.31)$$

$$\phi(t_e, t)_{\downarrow, y} = \frac{g}{\sqrt{v_g}} e^{\frac{\delta_e}{2}(t-t_e)} \theta(t - t_e) c_{\uparrow}(t_e). \quad (4.32)$$

The final step to solve the Schrödinger equation is to determine the coefficients for the two excited states. This is done by integrating (4.15)-(4.18), which gives:

$$\begin{aligned} \phi(t_e, t)_{\uparrow, x} &= i \frac{\delta_g}{2} \int_{t_e - \epsilon}^{t_e + \epsilon} dt \phi(t_e, t)_{\uparrow, x} - i \frac{g}{\sqrt{v_g}} \int_{t_e - \epsilon}^{t_e + \epsilon} dt c_{\uparrow}(t) \delta(t - t_e) \\ &= -i \frac{g}{\sqrt{v_g}} c_{\uparrow}(t) \end{aligned} \quad (4.33)$$

$$\begin{aligned} \phi(t_e, t)_{\uparrow, y} &= i \frac{\delta_g}{2} \int_{t_e - \epsilon}^{t_e + \epsilon} dt \phi(t_e, t)_{\uparrow, y} - i \frac{g}{\sqrt{v_g}} \int_{t_e - \epsilon}^{t_e + \epsilon} dt c_{\downarrow}(t) \delta(t - t_e) \\ &= -i \frac{g}{\sqrt{v_g}} c_{\downarrow}(t) \end{aligned} \quad (4.34)$$

$$\begin{aligned} \phi(t_e, t)_{\downarrow, x} &= i \frac{\delta_g}{2} \int_{t_e - \epsilon}^{t_e + \epsilon} dt \phi(t_e, t)_{\downarrow, x} - i \frac{g}{\sqrt{v_g}} \int_{t_e - \epsilon}^{t_e + \epsilon} dt c_{\downarrow}(t) \delta(t - t_e) \\ &= -i \frac{g}{\sqrt{v_g}} c_{\downarrow}(t) \end{aligned} \quad (4.35)$$

$$\begin{aligned} \phi(t_e, t)_{\downarrow, y} &= i \frac{\delta_g}{2} \int_{t_e - \epsilon}^{t_e + \epsilon} dt \phi(t_e, t)_{\downarrow, y} - i \frac{g}{\sqrt{v_g}} \int_{t_e - \epsilon}^{t_e + \epsilon} dt c_{\uparrow}(t) \delta(t - t_e) \\ &= -i \frac{g}{\sqrt{v_g}} c_{\uparrow}(t). \end{aligned} \quad (4.36)$$

Inserting (4.33)-(4.36) into (4.13) and (4.14) yields

$$\dot{c}_{\uparrow}(t) = -i \frac{\delta_e}{2} c_{\uparrow}(t) - 2 \frac{g^2}{v_g} c_{\uparrow}(t) \quad (4.37)$$

$$\dot{c}_{\downarrow}(t) = i \frac{\delta_e}{2} c_{\downarrow}(t) - 2 \frac{g^2}{v_g} c_{\downarrow}(t) \quad (4.38)$$

with the solutions

$$c_{\uparrow}(t) = e^{-2 \frac{g^2}{v_g} t_e + i \frac{\delta_e}{2} t} \quad (4.39)$$

$$c_{\downarrow}(t) = e^{-2 \frac{g^2}{v_g} t_e - i \frac{\delta_e}{2} t}. \quad (4.40)$$

Lastly, we define the spontaneous emission rate as $\gamma \equiv 4\frac{g^2}{v_g}$ and insert (4.39) and (4.40) into (4.29)-(4.32). This yields the six coefficients and the result of this section

$$c_{\uparrow}(t) = e^{-\frac{\gamma}{2}t + i\frac{\delta_e}{2}t} \quad (4.41)$$

$$c_{\downarrow}(t) = e^{-\frac{\gamma}{2}t - i\frac{\delta_e}{2}t} \quad (4.42)$$

$$\phi(t_e, t)_{\uparrow, x} = \sqrt{\gamma} e^{-i\frac{\delta_g}{2}(t-t_e) - \frac{\gamma}{2}t_e + i\frac{\delta_e}{2}t_e} \theta(t - t_e) \quad (4.43)$$

$$\phi(t_e, t)_{\uparrow, y} = \sqrt{\gamma} e^{-i\frac{\delta_g}{2}(t-t_e) - \frac{\gamma}{2}t_e - i\frac{\delta_e}{2}t_e} \theta(t - t_e) \quad (4.44)$$

$$\phi(t_e, t)_{\downarrow, x} = \sqrt{\gamma} e^{i\frac{\delta_g}{2}(t-t_e) - \frac{\gamma}{2}t_e - i\frac{\delta_e}{2}t_e} \theta(t - t_e) \quad (4.45)$$

$$\phi(t_e, t)_{\downarrow, y} = \sqrt{\gamma} e^{i\frac{\delta_g}{2}(t-t_e) - \frac{\gamma}{2}t_e + i\frac{\delta_e}{2}t_e} \theta(t - t_e). \quad (4.46)$$

We have, in summation, obtained complete knowledge of a four-level system describing an electron or hole in a magnetic field which can be excited by absorbing a photon and spontaneous decay by emitting a photon. In the following sections we describe the two protocols for creating spin-photon entanglement using such a four-level system and (4.41)-(4.46) shall, naturally, play an essential role.

Chapter 5

Spin-Photon Frequency Entanglement

The first protocol examined in this thesis is a protocol which creates spin-photon frequency entanglement. Specifically, it creates Bell states, see (2.4) and (2.5), by initialising the ground state spin in $|\downarrow\rangle$, then exciting it to a trion state $|\downarrow\rangle \rightarrow |\downarrow\downarrow\rangle$, and finally letting it spontaneously decay which creates the Bell state.

In this chapter, spin-photon frequency entanglement is examined by first introducing the theory behind the protocol and then going into depth with the possible imperfections that can affect the outcome of the protocol and the techniques applied to handle these complications.

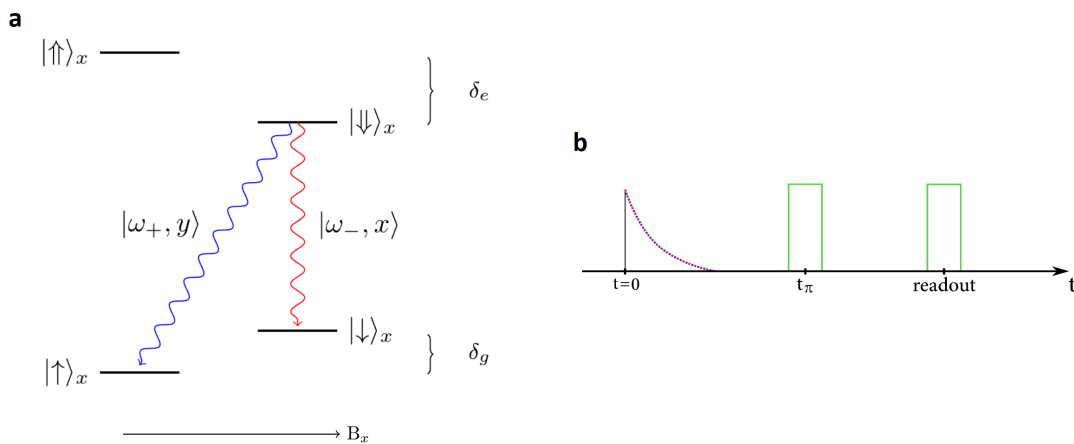


FIGURE 5.1: **a**, Level diagram showing the spontaneous emission of a photon frequency entangled with the ground state spin. We assume the level $|\uparrow\rangle_x$ to be isolated from the rest of the system such that we may regard the diagram as an effective three level system. **b**, timeline showing the pulse sequence of the protocol. Assuming the spin is initialised in $|\downarrow\rangle_x$, the quantum dot is excited at $t = 0$, a spin-echo pulse is applied at t_π and the spin is subsequently read out.

The essential steps applied in the protocol are presented in fig. 5 which shows both a level diagram of the system and a timeline providing the pulse sequence applied in the protocol. No details about the experimental techniques for spin initialisation and readout are provided here, but further details can be found in [9, 24].

In the previous section, the wave function for the system was derived and these results can now be applied for this protocol. By inserting the coefficients (4.44) and (4.45)

into the wave function (4.10), the state of the system is defined:

$$|\psi(t)\rangle = \sqrt{\frac{\gamma}{2}} \int_0^\infty dt_e \theta(t - t_e) (e^{-i\frac{\delta g}{2}(t-t_e) - \frac{\gamma}{2}t_e - i\frac{\delta e}{2}t_e} \hat{a}_y^\dagger(z_0) |\uparrow, 0\rangle + e^{i\frac{\delta g}{2}(t-t_e) - \frac{\gamma}{2}t_e - i\frac{\delta e}{2}t_e} \hat{a}_x^\dagger(z_0) |\uparrow, 0\rangle) \quad (5.1)$$

$$= \frac{1}{\sqrt{2}} (|\uparrow\rangle |\omega_+, y\rangle + |\downarrow\rangle |\omega_-, x\rangle), \quad (5.2)$$

where in (5.2), the form of the wave function is simplified by introducing $|\omega_+, +\rangle$ and $|\omega_-, -\rangle$.

Depending on how we map from physical qubit to logical qubit, (5.2) can be mapped into either of the bell states (2.4) and (2.5). As an example, mapping $|\uparrow\rangle \rightarrow |0\rangle$, $|\downarrow\rangle \rightarrow |1\rangle$, $|\omega_+, y\rangle \rightarrow |0\rangle$ and $|\omega_-, x\rangle \rightarrow |1\rangle$ would yield the Bell state $|\Phi^+\rangle$ which we in section 2.1 showed to maximally entangled.

As mentioned above, two possible imperfections of the protocol are studied in this chapter: sub-maximal entanglement and sub-maximal visibility. The two types of imperfections are briefly introduced below and examined in more detail within the following sections.

The first imperfection appear if the two created photons are not orthogonal, i.e.

$$\langle \omega_+, y | \omega_-, x \rangle \neq 0. \quad (5.3)$$

Physically, this means that the two photons have a overlap in frequency or, in other words, that the grounds states are insufficiently separated. Recall the calculation leading to (2.10) in section 2.1 which showed that Bell states are indeed maximally entangled since the subsystem were maximally mixed. This calculation relied on the states of the subsystem A and B to be orthogonal. Hence if this is no longer the case the subsystems are not maximally mixed, meaning the Bell states is sub-maximal entangled.

The second imperfection is related to the ability to observe the system, i.e. a possible imperfect visibility of the system. Imperfect visibility is twofold. The first part involves the finite time resolution of the detector. This sets an upper limit for how strong the external magnetic field can be since a too strong magnetic field can ruin the visibility caused by a high Larmor frequency of the ground state spin. The second part involves the Overhauser field of the nuclear spin-bath in the quantum dot which, as explained in section 3.1.3, introduces an uncertainty in frequency.

In section 5.1 and 5.2 are sub-maximal entanglement and sub-maximal visibility examined, respectively. Furthermore, the effect of encountering both types of imperfections is discussed in section 5.2.3 which shows that an optimisation problem arise due to the inversely dependence on the decay rate γ and the ground state splitting δg .

5.1 Sub-maximal Entanglement

As explained above, it is not possible to create a Bell state if the two ground states, $|\omega_+, y\rangle$ and $|\omega_-, x\rangle$, are insufficiently separated. In order to characterise this imperfection, the concept of fidelity can be applied which was introduced in section 2.2. When studying sub-maximal entanglement, the fidelity quantifying the imperfection

is referred to as state fidelity.

In section 2.2, the fidelity was defined as

$$F = |\langle \psi_{ideal} | \psi_{output} \rangle|^2. \quad (5.4)$$

The fidelity of the studied system can be determined using the coefficients (4.41)-(4.46) and the definition of the wave function (4.10). In order to ease the calculation, we start by defining a new smarter choice of basis for the states. This basis is a photon basis which is all ways orthogonal, even for low ground state separation, which is superior to the photon basis used so far since this basis is naturally not all ways orthogonal.

5.1.1 Orthogonal Basis

We introduce a shorthand notation by omitting the polarisation of the photons. Using this notation, the state in (5.2) can be written as:

$$|\psi\rangle = \frac{1}{\sqrt{2}}(|\uparrow\rangle|\omega_+\rangle + |\downarrow\rangle|\omega_-\rangle). \quad (5.5)$$

The task is now to express (5.5) in a orthogonal basis. For this purpose, we introduce the two vectors

$$|\psi_+\rangle = \frac{1}{\sqrt{2}}(e^{i\phi}|\uparrow\rangle + e^{-i\phi}|\downarrow\rangle) \quad (5.6)$$

$$|\psi_-\rangle = \frac{1}{\sqrt{2}}(e^{i\phi}|\uparrow\rangle - e^{-i\phi}|\downarrow\rangle), \quad (5.7)$$

and rewrite (5.5) as

$$|\psi\rangle = \frac{1}{2}(|\psi_+\rangle(e^{-i\phi}|\omega_+\rangle + e^{i\phi}|\omega_-\rangle) + |\psi_-\rangle(e^{-i\phi}|\omega_+\rangle - e^{i\phi}|\omega_-\rangle)). \quad (5.8)$$

We are free to chose ϕ . If we chose it to be $\phi = -\arccos\langle\omega_+|\omega_-\rangle$ then (5.8) is orthogonal. For further convenience we define the two vectors

$$|\theta_\pm\rangle = \frac{1}{\sqrt{2}}(e^{-i\phi}|\omega_+\rangle \pm e^{i\phi}|\omega_-\rangle), \quad (5.9)$$

such that (5.8) can be written as

$$|\psi\rangle = \frac{1}{2}(|\psi_+\rangle|\theta_+\rangle + |\psi_-\rangle|\theta_-\rangle). \quad (5.10)$$

Lastly, we normalise (5.10) to obtain the spin-photon state (5.2) rewritten in an orthogonal basis

$$|\Phi\rangle = N_+|\psi_+\rangle|\theta_+\rangle + N_-|\psi_-\rangle|\theta_-\rangle, \quad (5.11)$$

such that $\langle\Phi|\Phi\rangle = 1$ with the normalisation coefficients $N_\pm = \frac{\sqrt{1 \pm |\langle\omega_+|\omega_-\rangle|}}{\sqrt{2}}$. In appendix A, a further discussion of the orthogonalisation and normalisation of the state is presented.

5.1.2 State Fidelity

We now proceed to calculate the state fidelity using the orthonormal state found above. In the ideal state, i.e. maximally entangled state, the photons are completely separated in frequency, hence $\langle \omega_+ | \omega_- \rangle = 0$ and from (5.10) we define the ideal state as

$$|\psi_{ideal}^{state}\rangle = \frac{1}{\sqrt{2}} (|\psi_+\rangle |\theta_+\rangle + |\psi_-\rangle |\theta_-\rangle). \quad (5.12)$$

The output state is simply (5.10)

$$|\psi_{output}^{state}\rangle = N_+ |\psi_+\rangle |\theta_+\rangle + N_- |\psi_-\rangle |\theta_-\rangle, \quad (5.13)$$

which is normalised such that $N_+^2 + N_-^2 = 1$. The state fidelity, given the ideal and output states in (5.12) and (5.13) respectively, can now be determined:

$$F_{state} = |\langle \psi_{ideal}^{state} | \psi_{output}^{state} \rangle|^2 \quad (5.14)$$

$$= \left| \frac{1}{\sqrt{2}} (\langle \psi_+ | \langle \theta_+ | + \langle \psi_- | \langle \theta_- |) (N_+ |\psi_+\rangle |\theta_+\rangle + N_- |\psi_-\rangle |\theta_-\rangle) \right|^2 \quad (5.15)$$

$$= \left| \frac{N_+}{\sqrt{2}} + \frac{N_-}{\sqrt{2}} \right|^2 \quad (5.16)$$

$$= \frac{1}{2} (N_+ N_+ + N_- N_- + 2N_+ N_-) \quad (5.17)$$

$$= \frac{1}{2} \left(\frac{1 + |\langle \omega_+ | \omega_- \rangle|}{2} - \frac{1 - |\langle \omega_+ | \omega_- \rangle|}{2} + \sqrt{1 + |\langle \omega_+ | \omega_- \rangle|} \sqrt{1 - |\langle \omega_+ | \omega_- \rangle|} \right) \quad (5.18)$$

$$= \frac{1}{2} + \frac{1}{2} \sqrt{1 - |\langle \omega_+ | \omega_- \rangle|^2}. \quad (5.19)$$

From the definition of $|\omega_+\rangle$ and $|\omega_-\rangle$ in (5.2) we can calculate that

$$|\langle \omega_+ | \omega_- \rangle|^2 = \frac{\gamma^2}{\delta_g^2 + \gamma^2}. \quad (5.20)$$

By combining the expressions in (5.20) and (5.19), the state fidelity is determined

$$F_{state} = \frac{1}{2} + \frac{1}{2} \sqrt{1 - \frac{\gamma^2}{\delta_g^2 + \gamma^2}}. \quad (5.21)$$

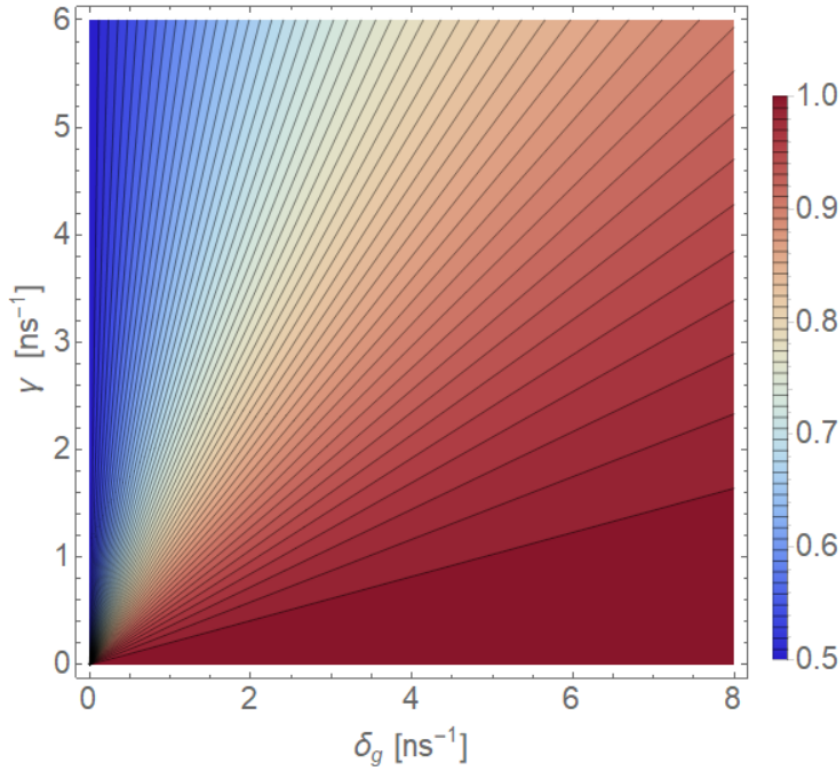


FIGURE 5.2: Each contour line corresponds to a change in F_{state} of 0.01. $F_{state} \sim 1$ in the limit $\delta_g \gg \gamma$ which corresponds to a Bell state and hence maximal entanglement. $F_{state} \sim 1/2$ in the limit $\gamma \gg \delta_g$ which corresponds to no entanglement.

As a final remark in this section, the typical decay rates are related to the typical g factors of electrons and holes in order to determine the necessary strength of the magnetic field required to sufficiently separate the ground state and obtain a state fidelity of $F_{state} > 0.99$. The relation between the ground state energy splitting, the g factor and the magnetic field is given by Zeeman Hamiltonians (3.3) and (3.4), which we collectively write as

$$\delta_g = \frac{g\mu_B}{\hbar} B. \quad (5.22)$$

Without any Purcell enhancement, the decay rate is typically $\gamma \approx 1 \text{ ns}^{-1}$ and the g factors are typically $0.35 < |g_x^e| < 1.9$ and $0.06 < |g_x^h| < 0.14$, see section 3.2.1 and 3.1.2, respectively. This shows that a state fidelity of $F_{state} > 0.99$ is achievable with a strength of the in-plane magnetic field in the x-direction of $0.14 \text{ T} < B < 0.78 \text{ T}$ and $1.96 \text{ T} < B < 4.48 \text{ T}$, respectively. Note, as previously stated, that the g factor can depend on the magnetic field direction due to band mixing.

5.2 Visibility

The second imperfection we consider in the frequency entanglement protocol is imperfect visibility of the system. In the previous section we showed that the role of the magnetic field is vital if we wish to create a Bell State. As a consequence, one might naively think that a strong magnetic field all ways is favourable, however, we also need to consider our ability to observe the system. Imperfect visibility is twofold;

it depends both on the finite time resolution and the nuclear Overhauser field. Both effects will be included in the fidelity $F_{visibility}$, the measure of visibility.

5.2.1 Non-Averaged Visibility Fidelity

In contrast to the procedure used when calculating the state fidelity, it is now favourable to first calculate the non-averaged visibility fidelity and thereafter the averaged visibility fidelity. In order to do this, the non-averaged states are first identified as:

$$|\psi_{ideal}^{visibility}\rangle = \frac{1}{\sqrt{2}} (|\uparrow\rangle e^{-i\frac{\delta g}{2}(t-2t_\pi-t_c)} + |\downarrow\rangle e^{i\frac{\delta g}{2}(t-2t_\pi-t_c)}) \quad (5.23)$$

$$|\psi_{output}^{visibility}\rangle = \frac{1}{\sqrt{2}} (|\uparrow\rangle e^{-i(\frac{\delta g}{2}+\Delta\delta_g)(t-2t_\pi-t_e)} + |\downarrow\rangle e^{i(\frac{\delta g}{2}+\Delta\delta_g)(t-2t_\pi-t_e)}), \quad (5.24)$$

where t_π is the timing of the spin-echo pulse which is defined such that $t - 2t_\pi = 0$ corresponds to the spin-echo pulse being applied exactly between the excitation and readout. The actual time the photon is measured by the detector is t_c , and $t_e = t_c$ corresponds to no time-jitter. The uncertainty in frequency is taken into account by $\Delta\delta_g$ which is introduced by the nuclear Overhauser field.

The non-averaged visibility fidelity is

$$F(t, t_\pi, t_e, t_c, \Delta\delta_g) = \left| \langle \psi_{ideal}^{visibility} | \psi_{output}^{visibility} \rangle \right|^2 \quad (5.25)$$

$$= \left| \frac{1}{2} \left(\langle \uparrow | e^{i\frac{\delta g}{2}(t-2t_\pi-t_c)} + \langle \downarrow | e^{-i\frac{\delta g}{2}(t-2t_\pi-t_c)} \right) \right. \\ \left. \left(|\uparrow\rangle e^{-i(\frac{\delta g}{2}+\Delta\delta_g)(t-2t_\pi-t_e)} + |\downarrow\rangle e^{i(\frac{\delta g}{2}+\Delta\delta_g)(t-2t_\pi-t_e)} \right) \right|^2 \quad (5.26)$$

$$= \left| \frac{1}{2} \left(e^{i\frac{\delta g}{2}(t-2t_\pi-t_c)-i(\frac{\delta g}{2}+\Delta\delta_g)(t-2t_\pi-t_e)} \right. \right. \\ \left. \left. + e^{-i\frac{\delta g}{2}(t-2t_\pi-t_c)+i(\frac{\delta g}{2}+\Delta\delta_g)(t-2t_\pi-t_e)} \right) \right|^2 \quad (5.27)$$

$$= \frac{1}{4} \left(e^{-i\frac{\delta g}{2}(t_e-t_c)+i\Delta\delta_g(t-2t_\pi-t_e)} + e^{i\frac{\delta g}{2}(t_e-t_c)-i\Delta\delta_g(t-2t_\pi-t_e)} \right) \\ \left(e^{i\frac{\delta g}{2}(t_e-t_c)-i\Delta\delta_g(t-2t_\pi-t_e)} + e^{-i\frac{\delta g}{2}(t_e-t_c)+i\Delta\delta_g(t-2t_\pi-t_e)} \right) \quad (5.28)$$

$$= \frac{1}{4} \left(2 + e^{-2i(\frac{\delta g}{2}(t_e-t_c)+i\Delta\delta_g(t-2t_\pi-t_e))} \right. \\ \left. + e^{2i(\frac{\delta g}{2}(t_e-t_c)-i\Delta\delta_g(t-2t_\pi-t_e))} \right) \quad (5.29)$$

$$= \frac{1}{2} + \frac{1}{2} \cos(\delta_g(t_e - t_c) - 2\Delta\delta_g(t - 2t_\pi - t_e)). \quad (5.30)$$

This shows that the visibility fidelity is perfect, $F_{visibility} = 1$, in the limit where $\delta_g(t_e - t_c) - 2\Delta\delta_g(t - 2t_\pi - t_e) = 2n\pi$.

5.2.2 Averaged Visibility Fidelity

We now proceed by averaging (5.30) over three different probability distributions: the time resolution of the detector, the uncertainty in frequency introduced by the nuclear Overhauser field and the emission of a photon. Hence we write the averaged visibility fidelity as

$$\bar{F}_{visibility} = \int_{-\infty}^{\infty} d\Delta\delta_g \int_0^{\infty} dt_e \int_0^{\infty} dt_c \rho(t_c - t_e) \rho(\Delta\delta_g) \rho(t_e) F(t, t_\pi, t_e, t_c, \Delta\delta_g), \quad (5.31)$$

where

$$\rho(t_c - t_e) = \frac{1}{\sqrt{2\pi}\epsilon} e^{-\frac{(t_c - t_e)^2}{2\epsilon^2}} \quad (5.32)$$

$$\rho(\Delta\delta_g) = \frac{1}{\sqrt{2\pi}\sigma} e^{-\frac{\Delta\delta_g^2}{2\sigma^2}} \quad (5.33)$$

$$\rho(t_e) = \gamma e^{-\gamma t_e}. \quad (5.34)$$

The probability density of the time resolution of the detector, $\rho(t_c - t_e)$, is defined in (5.32) which shows a Gaussian distribution with the standard deviation ϵ . We shall refer to ϵ as the time-jitter. Detectors with $\epsilon = 0.03$ ns are commercial available [25]. The probability density for the Overhauser field, see section 3.1.3, is shown in (5.33) which is again a Gaussian distribution. The Overhauser field is approximated to only contain the component parallel to the applied magnetic field and it is written on an effective form where the uncertainty of the magnetic field has been substituted with the uncertainty in frequency splitting of the ground state, for which

$$T_2^* = \sqrt{2}/\sigma. \quad (5.35)$$

The relation (5.35) is derived in appendix B

Finally, the probability density of emitting a photon at time t_e is defined in (5.34) as an exponentially decaying function which can be determined using the coefficients found in section 4.3.

Now, we have all the components necessary to determine the averaged visibility fidelity. First, the visibility fidelity in (5.30) is inserted in the expression for the average visibility fidelity in (5.31):

$$\begin{aligned} \bar{F}_{visibility} = & \int_{-\infty}^{\infty} d\Delta\delta_g \int_0^{\infty} dt_e \int_0^{\infty} dt_c \rho(t_c - t_e) \rho(\Delta\delta_g) \rho(t_e) \\ & \left(\frac{1}{2} + \frac{1}{2} \cos(\delta_g(t_e - t_c) - 2\Delta\delta_g(t - 2t_\pi - t_e)) \right), \end{aligned} \quad (5.36)$$

which shows that two terms emerge that can be calculated separately. Separating the two terms of the averaged fidelity

$$\bar{F}_{visibility}(t, t_\pi) = \bar{F}^{(1)}(t, t_\pi) + \bar{F}^{(2)}(t, t_\pi), \quad (5.37)$$

where

$$\bar{F}^{(1)} = \frac{1}{2} \int_{-\infty}^{\infty} d\Delta\delta_g \int_0^{\infty} dt_e \int_0^{\infty} dt_c \rho(t_c - t_e) \rho(\Delta\delta_g) \rho(t_e) \quad (5.38)$$

$$\begin{aligned} \bar{F}^{(2)}(t, t_\pi) = & \frac{1}{2} \int_{-\infty}^{\infty} d\Delta\delta_g \int_0^{\infty} dt_e \int_0^{\infty} dt_c \rho(t_c - t_e) \rho(\Delta\delta_g) \rho(t_e) \\ & \cos(\delta_g(t_e - t_c) - 2\Delta\delta_g(t - 2t_\pi - t_e)). \end{aligned} \quad (5.39)$$

Now, (5.38) is straight forward to calculate since the three distributions are normalised according to (5.32)-(5.34) and hence

$$\bar{F}^{(1)} = \frac{1}{2} \int_{-\infty}^{\infty} d\Delta\delta_g \int_0^{\infty} dt_e \int_0^{\infty} dt_c \rho(t_c - t_e) \rho(\Delta\delta_g) \rho(t_e) = \frac{1}{2}. \quad (5.40)$$

To calculate the second term (5.39) in the averaged fidelity, we start by plugging (5.32)-(5.34) into (5.39) and rewriting the expression using Euler's formula

$$\begin{aligned} \bar{F}^{(2)} &= \frac{1}{2} \int_{-\infty}^{\infty} d\Delta\delta_g \int_0^{\infty} dt_e \int_0^{\infty} dt_c \rho(t_c - t_e) \rho(\Delta\delta_g) \rho(t_e) \\ &\quad \cos(\delta_g(t_e - t_c) - 2\Delta\delta_g(t - 2t_\pi - t_e)) \end{aligned} \quad (5.41)$$

$$\begin{aligned} &= \frac{\gamma}{8\pi\sigma\epsilon} \int_{-\infty}^{\infty} d\Delta\delta_g \int_0^{\infty} dt_e \int_0^{\infty} dt_c e^{-\frac{(t_c - t_e)^2}{2\epsilon^2}} e^{-\frac{\Delta\delta_g^2}{2\sigma^2}} e^{-\gamma t_e} \\ &\quad e^{i\delta_g(t_e - t_c) + 2i\Delta\delta_g(t - 2t_\pi - t_e)} + e^{-i\delta_g(t_e - t_c) - 2i\Delta\delta_g(t - 2t_\pi - t_e)}, \end{aligned} \quad (5.42)$$

and continue by evaluating the time integrals

$$\begin{aligned} \bar{F}^{(2)} &= \frac{\sqrt{2\pi}\gamma}{8\pi\sigma} \int_{-\infty}^{\infty} d\Delta\delta_g \int_0^{\infty} dt_e e^{-\frac{\Delta\delta_g^2}{2\sigma^2}} \left(e^{(t_e - i\epsilon\delta_g^2)^2/2 - \frac{t_e^2}{2\epsilon^2} - \gamma t_e + i\delta_g t_e + 2i\Delta\delta_g(t - 2t_\pi - t_e)} \right. \\ &\quad \left. + e^{(t_e + i\epsilon\delta_g^2)^2/2 - \frac{t_e^2}{2\epsilon^2} - \gamma t_e - i\delta_g t_e - 2i\Delta\delta_g(t - 2t_\pi - t_e)} \right) \end{aligned} \quad (5.43)$$

$$= \frac{\gamma}{4\sigma\sqrt{2\pi}} e^{-(\delta_g\epsilon)^2/2} \int_{-\infty}^{\infty} d\Delta\delta_g e^{-\frac{\Delta\delta_g^2}{2\sigma^2}} \left(\frac{e^{2i\Delta\delta_g(t - 2t_\pi)}}{\gamma - 2i\Delta\delta_g} + \frac{e^{-2i\Delta\delta_g(t - 2t_\pi)}}{\gamma + 2i\Delta\delta_g} \right). \quad (5.44)$$

In order to solve the last integral in (5.44) we perform a Fourier transformation. Realising that this integral is an inner product, we can use the unitarity of the Fourier transform to evaluate it. The two functions transform individually as

$$\mathcal{F} \left[e^{-\frac{\Delta\delta_g^2}{2\sigma^2} \pm 2i(t - 2t_\pi)\Delta\delta_g} \right] = \sigma e^{-\sigma^2(2(t - 2t_\pi) \pm t')^2/2} \quad (5.45)$$

$$\mathcal{F} \left[\frac{1}{\gamma \pm 2i\Delta\delta_g} \right] = \sqrt{2\pi} e^{\mp\gamma t'} \theta(\pm t'), \quad (5.46)$$

meaning the Fourier transform of (5.44) is

$$\begin{aligned} \mathcal{F}[\bar{F}^{(2)}(t, t_\pi)] &= \frac{\gamma}{4} e^{-(\delta_g\epsilon)^2/2} \int_{-\infty}^{\infty} dt' \left(e^{-\sigma^2(2(t - 2t_\pi) + t')^2/2 + \gamma t'} \theta(-t') \right. \\ &\quad \left. + e^{-\sigma^2(2(t - 2t_\pi) - t')^2/2 - \gamma t'} \theta(t') \right) \end{aligned} \quad (5.47)$$

$$= \sqrt{\frac{\pi}{2}} \frac{\gamma}{16\sigma} e^{-(\delta_g\epsilon)^2/2 - \gamma(t - 2t_\pi) + \frac{\gamma^2}{8\sigma^2}} \left(1 + \left(\frac{2\sigma(t - 2t_\pi) - \frac{\gamma}{2\sigma}}{\sqrt{2}} \right) \right). \quad (5.48)$$

The expressions determined in (5.40) and (5.48) can now be inserted into (5.37) which yields the result of this section

$$\bar{F}_{visibility}(t, t_\pi) = \frac{1}{2} + \sqrt{\frac{\pi}{2}} \frac{\gamma}{16\sigma} e^{-(\delta_g \epsilon)^2/2 - \gamma(t-2t_\pi) + \frac{\gamma^2}{8\sigma^2}} \left(1 + \left(\frac{2\sigma(t-2t_\pi) - \frac{\gamma}{2\sigma}}{\sqrt{2}}\right)\right). \quad (5.49)$$

The different parameters in (5.49) are now discussed starting with the timing of the spin echo pulse modeled by $t - 2t_\pi$. An optimal value is reached when $t - 2t_\pi = \gamma^{-1}$ since this corresponds to the case where an equal amount of time passes between the the average decay time γ^{-1} and the spin echo pulse t_π and between the spin echo pulse t_π and the readout. It is assumed from this point forward that $t - 2t_\pi = \gamma^{-1}$ unless otherwise stated.

The connection between the strength of the magnetic field and the time-jitter is now examined. In order to apply a high Larmor frequency it is necessary to have a good detector time resolution to observe the system. A high Larmor frequency demands a good detector time resolution to observe the system. Fig. 5.3 shows what magnetic field strength is feasible for a given detector time-jitter. It is found that using a

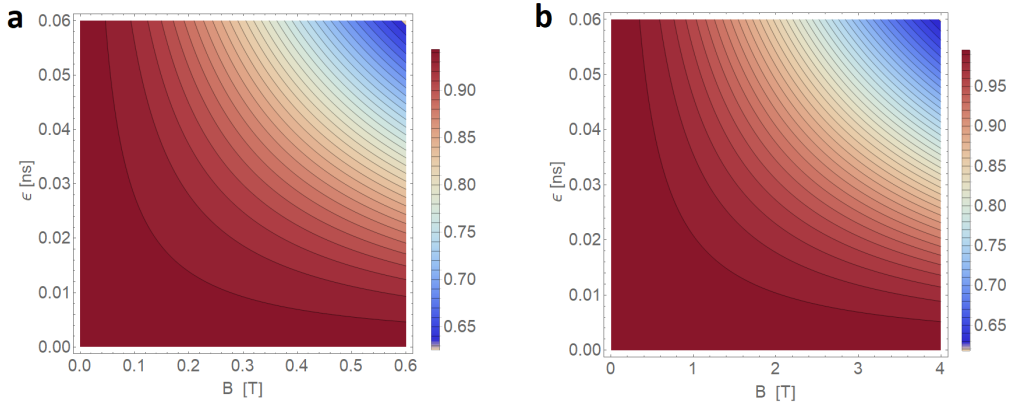


FIGURE 5.3: A contour plot of the visibility fidelity with optimal spin echo timing $t - 2t_\pi = \gamma^{-1}$. Each contour line corresponds to a change in fidelity of 0.01. **a**, Visibility fidelity for an electron in the ground state. Chosen values are: $\sigma = 0.7 \text{ ns}^{-1}$ (corresponding to $T_2^* = 2.0 \text{ ns}$), $\gamma = 2.4 \text{ ns}^{-1}$, and $g^e = 0.5$. **b**, Visibility fidelity for a hole in the ground state. Chosen values are: $\sigma = 0.07 \text{ ns}^{-1}$ (corresponding to $T_2^* = 20.2 \text{ ns}$), $\gamma = 1.2 \text{ ns}^{-1}$ and $g^h = 0.08 \text{ ns}^{-1}$.

hole is superior to an electron if we wish to use a strong magnetic field. A strong magnetic field is desirable as it suppresses the components of the Overhauser field orthogonal to B while narrowing the frequency distribution σ of the fluctuations parallel to B , enhancing the coherence time according to (5.35). Notice that in the case of the electron, not even a perfect detector ($\epsilon = 0$) and no external magnetic field ($B = 0$) would give a visibility fidelity above 0.95. This is because the visibility is still limited by the ratio between the decay rate and the coherence time γ/σ , which is chosen to be $\gamma/\sigma = 2.4 \text{ ns}^{-1}/0.7 \text{ ns}^{-1} = 3.43$. The ratio can be improved by Purcell enhancement (3.14) (recall that a decay rate of 5.7 ns^{-1} have been reported for the system of interest), however, as seen in fig. 5.4a, it is not possible to achieve a close-to-unity visibility fidelity for realistic Purcell enhancement and time-jitter if we refuse to go below $B = 0.3 \text{ T}$. For $\epsilon = 0.03 \text{ ns}^{-1}$ and $\gamma = 5.7 \text{ ns}^{-1}$ the visibility fidelity is $F_{visibility} \approx 0.95$ at $B = 0.3 \text{ T}$.

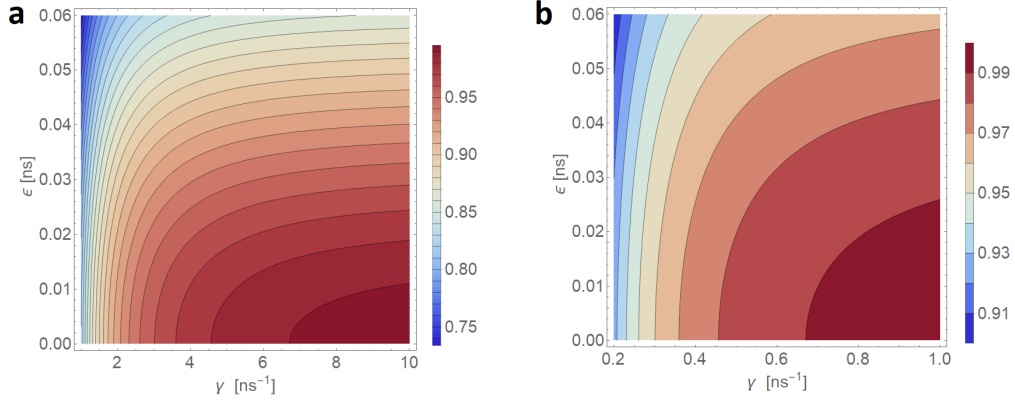


FIGURE 5.4: A contour plot of the visibility fidelity with optimal spin echo timing $t - 2t_\pi = \gamma^{-1}$. Each contour line corresponds to a change in fidelity of 0.01. **a**, Visibility fidelity for an electron in the ground state. Chosen values are: $\sigma = 0.7 \text{ ns}^{-1}$ (corresponding to $T_2^* = 2.0 \text{ ns}$), $B = 0.3 \text{ T}$ and $g^e = 0.5$. **b**, Visibility fidelity for a hole in the ground state. Chosen values are: $\sigma = 0.07 \text{ ns}^{-1}$ (corresponding to $T_2^* = 20.2 \text{ ns}$), $B = 0.8 \text{ T}$ and $g^h = 0.08$.

For the hole we have reason to be more optimistic regarding the visibility. From fig. 5.3 we see that for $\epsilon = 0.03 \text{ ns}$ we can allow $B = 0.8 \text{ T}$ and still achieve $F \approx 0.99$ at $\gamma = 1.2 \text{ ns}^{-1}$. This is supported by fig. 5.4b which also shows that the visibility is not particular vulnerable to lower decay rates.

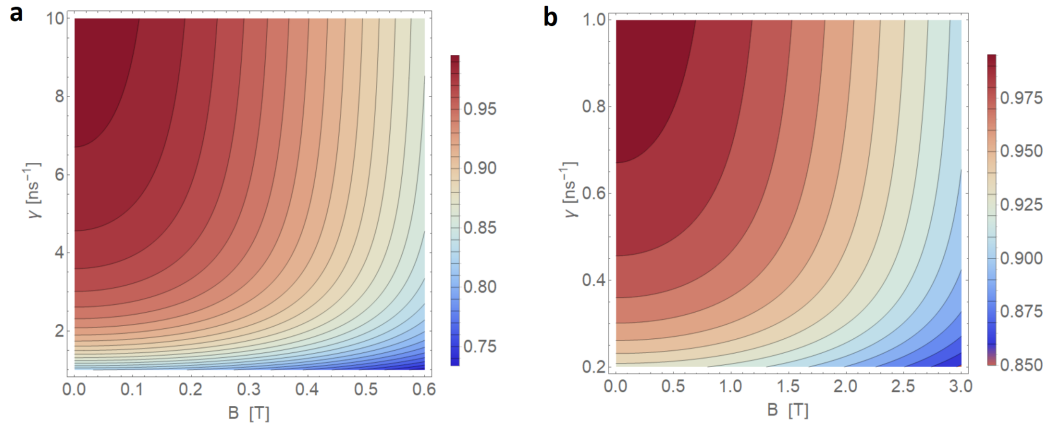


FIGURE 5.5: A contour plot of the visibility fidelity with optimal spin echo timing $t - 2t_\pi = \gamma^{-1}$. Each contour line corresponds to a change in fidelity of 0.01. **a**, Visibility fidelity for an electron in the ground state. Chosen values are: $\sigma = 0.7 \text{ ns}^{-1}$ (corresponding to $T_2^* = 2.0 \text{ ns}$), $\epsilon = 0.03 \text{ ns}$ and $g^e = 0.5$. **b**, Visibility fidelity for a hole in the ground state. Chosen values are: $\sigma = 0.07 \text{ ns}^{-1}$ (corresponding to $T_2^* = 20.2 \text{ ns}$), $\epsilon = 0.03 \text{ ns}$ and $g^h = 0.08$.

To conclude, the following parameter values result in a visibility fidelity of $\bar{F}_{visibility}^{electron} \approx 0.95$ and $\bar{F}_{visibility}^{hole} \approx 0.99$:

	ϵ [ns]	T_2^* [ns]	$g_{e/h}$	γ [ns ⁻¹]	B [T]	$F_{visibility}$
Electron:	0.03	2.0	0.5	5.7	0.3	≈ 0.95
Hole:	0.03	20.2	0.08	1.2	0.8	≈ 0.99

TABLE 5.1: Realistic parameter values and corresponding visibility fidelity.

Now, we will return to the state fidelity studied in section 5.1. The state fidelity depends on γ and δ_g , which for the values shown in table 5.1 is $F_{state} = 0.77$ and $F_{state} = 0.69$ for an electron and a hole respectively. These are relatively low fidelity values not ideal for the performance of the protocol. This effect is caused since the state fidelity favours a strong magnetic field. In fig. 5.3 and 5.5 is the visibility fidelity studied for varying strengths of B which shows that the visibility fidelity favours relatively low values of B . For the electron, it is found from from fig. 5.3a that no realistic detector would be able to observe the system at magnetic fields necessary to achieve a high state fidelity and from fig. 5.4a we see the same is true for realistic Purcell enhancement. In the case of holes, the results are so far more inconclusive. We are able to achieve close-to-unity visibility fidelity, but with a too low magnetic field and/or too high decay rate to achieve a high state fidelity. The question of interest is now whether it is possible to optimise the parameters such that the combined fidelity, defined as $F_{combined} = F_{state}\bar{F}_{visibility}$, becomes close-to-unitary. In the next section we perform a perturbative expansion on the F_{state} and $\bar{F}_{visibility}$ in order to optimise the combined fidelity for both the electron and hole.

5.2.3 Optimising the Combined Fidelity

We define the combined fidelity as

$$F_{combined} = F_{state}\bar{F}_{visibility}. \quad (5.50)$$

It is not trivial to optimise $F_{combined}$ partly due to the big parameter space and partly because of the error function in (5.49). Therefore we shall expand both (5.49) and (5.21) to simplify (5.50). Beginning with (5.49) we start by expanding the error function. In general, the error function can be expanded in an asymptotic series as

$$\text{erf}(x) = \sum_{n=0}^{\infty} \frac{(-1)^n (2n-1)!!}{2^n} x^{-(2n+1)},$$

Identifying $x = \frac{2\sigma(t-2t_\pi) - \frac{\gamma}{2\sigma}}{\sqrt{2}}$, the expansion of the error function to first order becomes

$$\left(\frac{2\sigma(t-2t_\pi) - \frac{\gamma}{2\sigma}}{\sqrt{2}}\right) \approx 1 - \frac{e^{-\left(2\sigma(t-2t_\pi) - \frac{\gamma}{2\sigma}\right)^2/2}}{\sqrt{\frac{\pi}{2}}\left(2\sigma(t-2t_\pi) - \frac{\gamma}{2\sigma}\right)}. \quad (5.51)$$

Substituting this into (5.49) yields

$$\bar{F}_{visibility} \approx \frac{1}{2} + \sqrt{\frac{\pi}{2}} \frac{\gamma}{16\sigma} e^{-\frac{(\delta_g \epsilon)^2}{2} - \gamma(t-2t_\pi) + \frac{\gamma^2}{8\sigma^2}} \left(1 + 1 - \frac{e^{-\left(2\sigma(t-2t_\pi) - \frac{\gamma}{2\sigma}\right)^2/2}}{\sqrt{\frac{\pi}{2}}\left(2\sigma(t-2t_\pi) - \frac{\gamma}{2\sigma}\right)}\right) \quad (5.52)$$

$$= \frac{1}{2} + \sqrt{\frac{\pi}{2}} \frac{\gamma}{8\sigma} e^{-\frac{(\delta_g \epsilon)^2}{2} - \gamma(t-2t_\pi) + \frac{\gamma^2}{8\sigma^2}} - \frac{\gamma e^{-\frac{(\delta_g \epsilon)^2}{2} - 2\sigma^2(t-2t_\pi)^2}}{16\left(2\sigma(t-2t_\pi) - \frac{\gamma}{2\sigma}\right)}. \quad (5.53)$$

We are interested in the limits $\gamma \gg \sigma$, $\gamma(2-2t_\pi) \sim 1$ and consequently $1 \gg \sigma(2-2t_\pi)$. In this limit, (5.53) can be approximated to

$$\bar{F}_{visibility}(t, t_\pi) \approx \frac{1}{2} + \frac{\gamma}{16(2\sigma(t-2t_\pi) - \frac{\gamma}{2\sigma})} e^{-\frac{(g_e B \epsilon)^2}{2} - 2\sigma^2(t-2t_\pi)^2}. \quad (5.54)$$

The three terms in (5.54) can now be expanded separately as follows

$$e^{-\frac{(g_e B \epsilon)^2}{2}} \approx 1 - \frac{(\delta_g B \epsilon)^2}{2} + \dots \quad (5.55)$$

$$e^{-2\sigma^2(t-2t_\pi)^2} \approx 1 - 2\sigma^2(t-2t_\pi)^2 + \dots \quad (5.56)$$

$$\frac{1}{2\sigma(2-2t_\pi) - \frac{\gamma}{2\sigma}} \approx -\frac{\gamma}{2\sigma} \left(1 - \frac{4\sigma^2(t-2t_\pi)}{\gamma} + \dots\right), \quad (5.57)$$

where the last expansion is true since $-1 < \frac{4\sigma(t-2t_\pi)}{\gamma} < 1$ in our expansion limit. This limit also allows us to substitute $t-2t_\pi \rightarrow \gamma^{-1}$ since $\gamma(2-2t_\pi) \sim 1$. Performing this substitution in (5.56) and (5.57) and hereafter substituting (5.55)-(5.57) into (5.54) yields

$$\bar{F}_{visibility} \approx \frac{1}{2} + \frac{\sigma}{8} \left(-1 + \frac{4\sigma^2}{\gamma^2} + \dots\right) \left(1 - \frac{2\sigma^2}{\gamma^2} + \dots\right) \left(1 - \frac{(\delta_g \epsilon)^2}{2} + \dots\right) \quad (5.58)$$

$$\approx 1 - \frac{2\sigma^2}{\gamma^2} - \frac{(\delta_g B \epsilon)^2}{4}. \quad (5.59)$$

This is the final expression for the simplified visibility of our system and it is pleasantly intuitive and transparent. To maximise the visibility we shall minimise the time-jitter, the frequency distribution of the nuclear spin-bath and the strength of the external magnetic field, while maximising the decay rate.

The state fidelity, which has inverse proportionality with respect to γ and the external magnetic field compared to the visibility, can be approximated in the limit $\delta_g \gg \gamma$ as

$$F_{state} \approx 1 - \frac{\gamma^2}{4\delta_g^2}. \quad (5.60)$$

We obtain the approximated combined fidelity by substituting the approximated expression for the visibility fidelity (5.59) and the approximated expression for the state fidelity (5.60) into the combined fidelity (5.50)

$$F_{combined} \approx \left(1 - \frac{2\sigma^2}{\gamma^2} - \frac{(\delta_g \epsilon)^2}{4}\right) \left(1 - \frac{\gamma^2}{4\delta_g^2}\right) \quad (5.61)$$

$$\approx 1 - \frac{(\delta_g \epsilon)^2}{4} - \frac{\gamma^2}{4\delta_g^2} + \frac{\epsilon^2 \gamma^2}{8} - \frac{2\sigma^2}{\gamma^2}. \quad (5.62)$$

Equation 5.62 allows for straightforward optimisation of $F_{combined}$ with respect to γ and B . The optimal values are

$$B_{optimal} = \sqrt{\frac{\gamma}{\epsilon(g\mu_B/\hbar)^2}}, \quad \gamma_{optimal} = \sqrt[3]{\frac{4\sigma^2}{\epsilon}}. \quad (5.63)$$

We conclude our study of imperfections in the frequency entanglement protocol by showing selected combined fidelities.

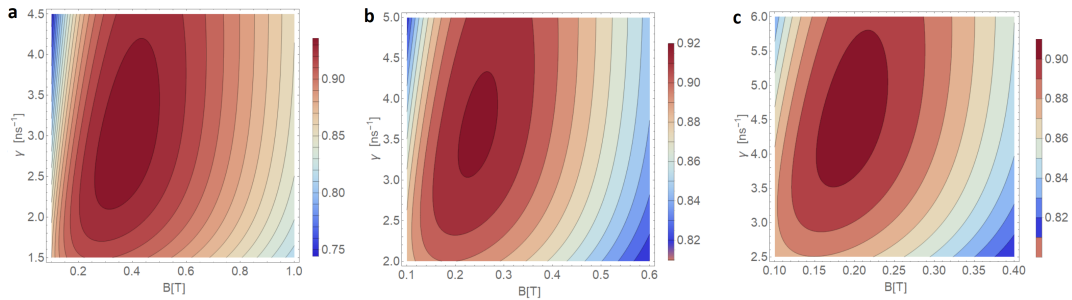


FIGURE 5.6: Combined fidelity with an electron in the ground state. Each contour line corresponds to a change in fidelity of 0.01. **a** is an optimistic case, **b** is a realistic case and **c** is a pessimistic case. The chosen values for all three cases can be seen in table 5.2.

Figure 5.6 shows three cases for the combined fidelity given an electron as the confined spin: the optimistic, realistic and pessimistic case. The parameter values applied to the three cases are listed in table 5.2 which are determined such that the optimistic case require an ideal protocol setup with state-of-the-art performance, the realistic case has lowered expectations to the protocol performance, and finally the pessimistic case has rather low expectations to the performance.

	ϵ [ns]	T_2^* [ns]	g_e	$\gamma_{optimal}$ [ns ⁻¹]	$B_{optimal}$ [T]	$F_{combined}$
a , optimistic	0.03	2.8	0.3	3.2	0.39	0.935
b , realistic	0.03	2.0	0.5	4.0	0.26	0.921
c , pessimistic	0.03	1.4	0.7	5.1	0.21	0.903

TABLE 5.2: Values used in fig. 5.6 where $\gamma_{optimal}$ and $B_{optimal}$ are calculated from (5.63).

For the realistic case, an unsatisfyingly low combined fidelity is evident. Comparing the realistic case to the optimistic shows that there is not much to gain in terms of the value of the combined fidelity since an increase of ~ 0.01 in the combined fidelity is insufficient to obtain a great fidelity. Two additional advantages are present in the optimistic case: a reduced sensitivity to changes in the decay rate around the optimal fidelity and an increase in $B_{optimal}$. The reduced sensitivity relaxes the requirements in the precision of the Purcell Enhancement and the increase in $B_{optimal}$ decreases the effect of the Overhauser field.

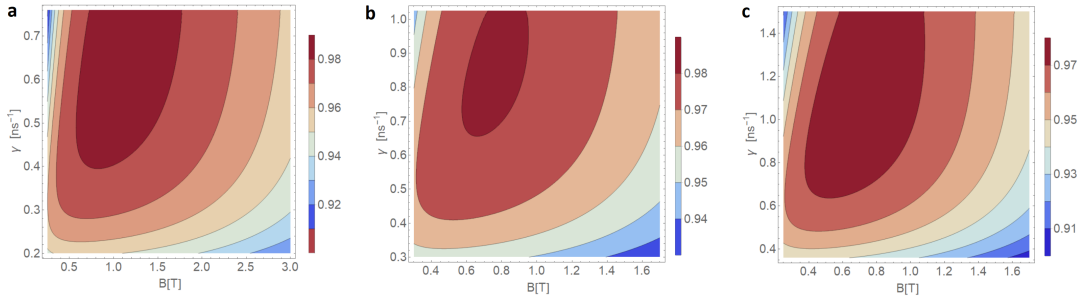


FIGURE 5.7: Combined fidelity with a hole in the ground state. Each contour line corresponds to a change in fidelity of 0.01. **a** is an optimistic case, **b** is a realistic case and **c** is a pessimistic case. The chosen values for all three cases can be seen in table 5.3.

Figure 5.7 similarly shows three cases for a hole in the ground state which are again denoted optimistic, realistic and pessimistic. The parameter values applied in the three cases are shown in table 5.3. Due to the long coherence time of the hole, it is evident that a hole is superior to an electron when comparing the ability to achieve a high combined fidelity.

	ϵ [ns]	T_2^* [ns]	g_h	$\gamma_{optimal}$ [ns^{-1}]	$B_{optimal}$ [T]	$F_{combined}$
a , optimistic	0.03	28.3	0.05	0.69	1.1	0.985
b , realistic	0.03	20.2	0.08	0.87	0.76	0.981
c , pessimistic	0.03	14.2	1.0	1.1	0.69	0.976

TABLE 5.3: Values used in fig. 5.7 where $\gamma_{optimal}$ and $B_{optimal}$ are calculated from (5.63).

Chapter 6

Spin-photon Time-Bin Entanglement

When applying time-bin entanglement, quantum information is encoded in the arrival time of photons. In this chapter, the protocol applied to create spin-photon time-bin entanglement is examined as proposed by Lee et. al [10]. Furthermore, the possible imperfections introduced when applying the protocol are studied. We begin by explaining the protocol. Then we shall study the visibility of the system, similarly to the studied made in the previous chapter for the frequency entanglement protocol, followed by a study of the impact of imperfect decay ratio and photon loss on the protocol. The last imperfection we study is the effect of phonon induced pure dephasing of the excited state. We conclude the study of imperfections in section 6.4, where the combined effect of the three imperfections is discussed.

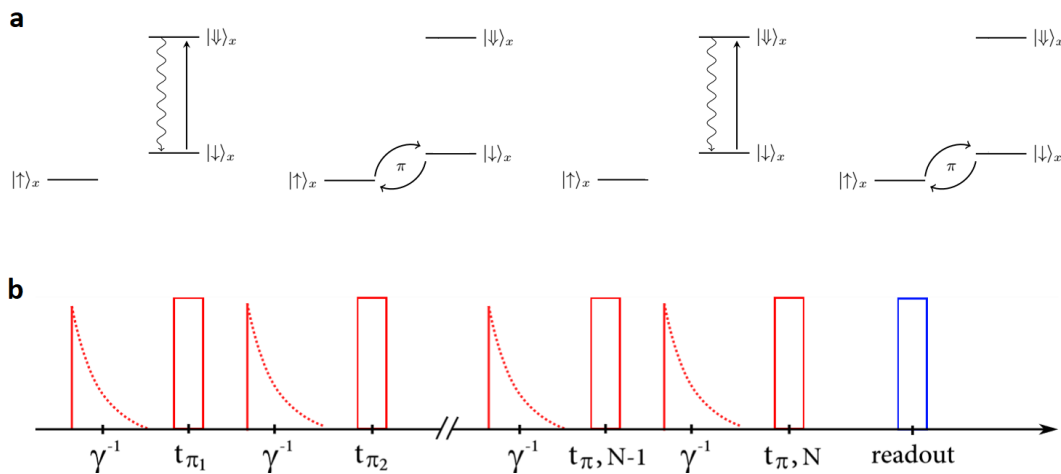


FIGURE 6.1: **a**, illustration of a single repetition of the protocol, creating of a single photon time-bin entangled with the ground state spin. **b**, timeline of the pulse sequence creating a $N/2$ photon GHZ state. γ^{-1} indicates a resonant pulse driving the transition $|\downarrow\rangle_x \rightarrow |\uparrow\rangle_x$ and the subsequent decay. $t_{\pi, i}$ indicates the i 'th ground state flip.

After initialising the ground state is in an equal superposition $1/\sqrt{2}(|\uparrow\rangle + |\downarrow\rangle)$ [47], a resonant pulse drives the transition $|\downarrow\rangle_x \rightarrow |\uparrow\rangle_x$ and the subsequent decay creates the state $1/\sqrt{2}(|\uparrow\rangle |0\rangle + |\downarrow\rangle |e\rangle)$, where $|e\rangle$ is a photon in an *early* time-bin. Then the ground state spin is flip creating the state $1/\sqrt{2}(-|\uparrow\rangle |e\rangle + |\downarrow\rangle |0\rangle)$, which corresponds to the second step shown in fig. 6.1a. In the third step, another excitation and decay creates a *late* photon and the state $1/\sqrt{2}(-|\uparrow\rangle |0, e\rangle + |\downarrow\rangle |l, 0\rangle)$, where $|l\rangle$ is a photon in a *late* time-bin. Finally, another ground state spin flip creates the state

$1/\sqrt{2}(|\uparrow\rangle |l, 0\rangle + |\downarrow\rangle |0, e\rangle)$. Repeating the sequence $N/2$ times creates the state

$$|\psi\rangle = \frac{1}{\sqrt{2}}(|\uparrow\rangle |l, 0\rangle^{\otimes \frac{N}{2}} + |\downarrow\rangle |0, e\rangle^{\otimes \frac{N}{2}}). \quad (6.1)$$

Mapping $|l, 0\rangle$ to a logical 1 and $|0, e\rangle$ to a logical 0 creates a $N/2$ photon GHZ state. The notation in (6.1) is clarified: the states $|l, 0\rangle^{\otimes \frac{N}{2}}$ and $|0, e\rangle^{\otimes \frac{N}{2}}$ are to be understood as

$$|l, 0\rangle^{\otimes \frac{N}{2}} = |l, 0, l, 0, \dots\rangle \quad (6.2)$$

$$|0, e\rangle^{\otimes \frac{N}{2}} = |0, e, 0, e, \dots\rangle, \quad (6.3)$$

with $N/2$ photons in each state, all with distinct emission times.

It is possible to alter the protocol to create a 1D cluster state (see section 2.1.1) by implementing *Hadamard* gates. A Hadamard transform the spins as:

$$|\uparrow\rangle \rightarrow \frac{1}{\sqrt{2}}(|\uparrow\rangle + |\downarrow\rangle), \quad |\downarrow\rangle \rightarrow \frac{1}{\sqrt{2}}(|\uparrow\rangle - |\downarrow\rangle). \quad (6.4)$$

Applying this transformation after the creation of every late photon will result in the creation of a 1D cluster state. In this chapter we shall only study the GHZ state, but the imperfections considered are equally relevant for the 1D cluster state.

6.1 Visibility

It is unnecessary to include the imperfection of the detector for time-bin entangled states when the time-bin is much larger than the uncertainty in detection time. This assumption is very reasonable since detectors with time-jitter in the order of picoseconds are commercially available.

However, the nuclear Overhauser field can in some cases ruin the visibility. This effect, caused by the nuclear Overhauser field, can be examined using a calculation of the visibility fidelity which is the focus of this section. The calculation of the visibility fidelity is very similar to the calculation performed in chapter 5.2 but with two main differences. Since the imperfection of the detector is now longer relevant, we do not average the fidelity over the time-resolution of the detector. Also, since the time-bin protocol is capable of creating GHZ-states, we shall generalise the fidelity to an arbitrary number of photons.

6.1.1 The Ideal State and Output State

In order to determine the visibility fidelity, it is necessary to first define the ideal state and output state of the system. We begin by writing the ideal $N/2$ -photon GHZ state as

$$\begin{aligned} |\psi_{Ideal, GHZ}^{visibility}\rangle = & \frac{1}{\sqrt{2}}(|\uparrow\rangle |0, e\rangle^{\otimes \frac{N}{2}} e^{-i\frac{\delta g}{2}(\tau_1 - t_{e,1} + \tau_3 - t_{e,3} + \dots + \tau_{N-1} - t_{e,N-1})} \\ & + |\downarrow\rangle |l, 0\rangle^{\otimes \frac{N}{2}} e^{-i\frac{\delta g}{2}(\tau_2 - t_{e,2} + \tau_4 - t_{e,4} + \dots + \tau_N - t_{e,N})}). \end{aligned} \quad (6.5)$$

The photon states $|0, e\rangle$ and $|l, 0\rangle$ represent an early and a late photon, respectively. The quantum dot is excited N times, thus creating $N/2$ early and $N/2$ late states.

The timing of the ground state flip is defined similar to the spin-echo pulse, as

$$\tau_i = t - 2t_{\pi,i} \quad (6.6)$$

where $t_{\pi,i}$ is the time of the i 'th π -pulse.

The emission time of the i 'th photon is written as $t_{e,i}$. Later, when we find the averaged fidelity, we must average over the N emission times. Furthermore we must average over the frequency distribution introduced by the Overhauser field. We include this in the output $N/2$ -photon GHZ state as

$$\begin{aligned} |\psi_{output,GHZ}^{visibility}\rangle &= \frac{1}{\sqrt{2}} \left(|\uparrow\rangle |0, e\rangle \otimes \frac{N}{2} e^{-i(\frac{\delta_g}{2} + \Delta\delta_g)(\tau_1 - t_{e,1} + \tau_3 - t_{e,3} + \dots + \tau_{N-1} - t_{e,N-1})} \right. \\ &\quad \left. + |\downarrow\rangle |l, 0\rangle \otimes \frac{N}{2} e^{-i(\frac{\delta_g}{2} + \Delta\delta_g)(\tau_2 - t_{e,2} + \tau_4 - t_{e,4} + \dots + \tau_N - t_{e,N})} \right). \end{aligned} \quad (6.7)$$

6.1.2 Visibility Fidelity

We find the non-averaged fidelity by taking the absolute square of the overlap between the input and output state, see (6.5) and (6.7), which yields

$$\begin{aligned} F_{visibility}(\tau_N, \dots, \tau_1) &= |\langle \psi_{Ideal,GHZ}^{visibility} | \psi_{output,GHZ}^{visibility} \rangle|^2 \\ &= \frac{1}{2} \left(\langle \uparrow | \langle 0, e | \otimes \frac{N}{2} e^{i\frac{\delta_g}{2}(\tau_1 - t_{e,1} + \tau_3 - t_{e,3} + \dots + \tau_{N-1} - t_{e,N-1})} \right. \\ &\quad \left. + \langle \downarrow | \langle l, 0 | \otimes \frac{N}{2} e^{i\frac{\delta_g}{2}(\tau_1 - t_{e,1} + \tau_3 - t_{e,3} + \dots + \tau_{N-1} - t_{e,N-1})} \right) \\ &\quad \left(|\uparrow\rangle |0, e\rangle \otimes \frac{N}{2} e^{-i(\frac{\delta_g}{2} + \Delta\delta_g)(\tau_1 - t_{e,1} + \tau_3 - t_{e,3} + \dots + \tau_{N-1} - t_{e,N-1})} \right. \\ &\quad \left. + |\downarrow\rangle |l, 0\rangle \otimes \frac{N}{2} e^{-i(\frac{\delta_g}{2} + \Delta\delta_g)(\tau_2 - t_{e,2} + \tau_4 - t_{e,4} + \dots + \tau_N - t_{e,N})} \right)^2 \\ &= \frac{1}{2} + \frac{1}{2} \cos \left(-i^N \Delta\delta_g (\tau_N - t_{e,N} + \dots + \tau_1 - t_{e,1}) \right). \end{aligned} \quad (6.8)$$

To create a single photon the quantum dot must be excited twice, hence we do not allow N to be an odd number and do not have to worry about an imaginary argument in the cosine.

We write the averaged fidelity as

$$\begin{aligned} \bar{F}_{visibility}(\tau_N, \dots, \tau_1) &= \int_{-\infty}^{\infty} d\Delta\delta_g \int_0^{\infty} \dots \int_0^{\infty} dt_{e,N} \dots dt_{e,1} \rho(\Delta\delta_g) \\ &\quad \rho(t_{e,N}, \dots, t_{e,1}) F(\tau_N, \dots, \tau_1), \end{aligned} \quad (6.9)$$

where

$$\rho(\Delta\delta_g) = \frac{1}{\sqrt{2\pi}\sigma} e^{-\frac{\Delta\delta_g^2}{2\sigma^2}} \quad (6.10)$$

$$\rho(t_{e,N}, \dots, t_{e,1}) = \gamma^N e^{-\gamma(t_{e,N} - \dots - t_{e,1})}, \quad (6.11)$$

from identical arguments as in the frequency entanglement visibility fidelity.

We now calculate the averaged fidelity by inserting the non-averaged fidelity (6.8), and the probability density distributions in (6.10) and (6.11) into the equation for the

time-averaged fidelity (6.9), which yields

$$\begin{aligned}
\bar{F}(\tau_N, \dots, \tau_1) &= \frac{\gamma^N}{2^N \sqrt{2\pi\sigma}} \int_{-\infty}^{\infty} d\Delta\delta_g \int_0^{\infty} \dots \int_0^{\infty} dt_{e,N} \dots dt_{e,1} e^{-\frac{\Delta\delta_g^2}{2\sigma^2} - \frac{\gamma}{2}(t_{e,N} + \dots + t_{e,1})} \\
&\quad \left(\frac{1}{2} + \frac{1}{2} \cos \left(-i^N \Delta\delta_g (\tau_N - t_{e,N} - \tau_{N-1} + t_{e,N-1} + \dots - \tau_1 - t_{e,1}) \right) \right) \\
&= \frac{\gamma^N}{2^N \sqrt{2\pi\sigma}} \int_{-\infty}^{\infty} d\Delta\delta_g \int_0^{\infty} \dots \int_0^{\infty} dt_{e,N} \dots dt_{e,1} e^{-\frac{\delta\delta_g^2}{2\sigma^2} - \frac{\gamma}{2}(t_{e,N} + \dots + t_{e,1})} \\
&\quad \left(\frac{1}{2} + \frac{1}{4} (e^{i^{N+1} \Delta\delta_g (\tau_N - t_{e,N} - \tau_{N-1} + t_{e,N-1} + \dots - \tau_1 - t_{e,1})} \right. \\
&\quad \left. + e^{-i^{N+1} \Delta\delta_g (\tau_N - t_{e,N} - \tau_{N-1} + t_{e,N-1} + \dots - \tau_1 - t_{e,1})}) \right)
\end{aligned}$$

The calculation can be split into several pieces which will now be evaluated separately. Starting with the part independent of $\tau_N \dots \tau_1$, we find that

$$\frac{\gamma^N}{2^{N+1} \sqrt{2\pi\sigma}} \int_{-\infty}^{\infty} d\Delta\delta_g \int_0^{\infty} \dots \int_0^{\infty} dt_{e,N} \dots dt_{e,1} e^{-\frac{\Delta\delta_g^2}{2\sigma^2} - \frac{\gamma}{2}(t_{e,N} + \dots + t_{e,1})} = \frac{1}{2},$$

since the distributions are normalised according to (6.10) and (6.11).

The part which depends on $\tau_N \dots \tau_1$ is more complicated to evaluate. We start by rewriting the cosine using Euler's formula and then evaluating the N emission time

integrals, which gives

$$F^l(\tau_N, \dots, \tau_1) = \frac{\gamma^N}{2^{N+2}\sqrt{2\pi\sigma}} \int_{-\infty}^{\infty} d\Delta\delta_g \int_0^{\infty} \dots \int_0^{\infty} dt_{e,N} \dots dt_{e,1} e^{-\frac{\Delta\delta_g^2}{2\sigma^2} - \frac{\gamma}{2}(t_{e,N} + \dots + t_{e,1})} \\ (e^{i^{N+1}\Delta\delta_g(\tau_N - t_{e,N} - \tau_{N-1} + t_{e,N-1} + \dots - \tau_1 - t_{e,1})} + e^{-i^{N+1}\Delta\delta_g(\tau_N - t_{e,N} - \tau_{N-1} + t_{e,N-1} + \dots - \tau_1 - t_{e,1})}) \quad (6.12)$$

$$= \frac{\gamma^N}{2^{N+2}\sqrt{2\pi\sigma}} \int_{-\infty}^{\infty} d\Delta\delta_g e^{-\frac{\Delta\delta_g^2}{2\sigma^2}} \int_0^{\infty} \dots \int_0^{\infty} dt_{e,N} \dots dt_{e,1} \\ (e^{-t_{e,N}(\frac{\gamma}{2} + i^{N+1}\Delta\delta_g) - \dots - t_{e,1}(\frac{\gamma}{2} - i^{N+1}\Delta\delta_g) + i^{N+1}\Delta\delta_g(\tau_N - \tau_{N-1} + \dots - \tau_1)} \\ + e^{-t_{e,N}(\frac{\gamma}{2} - i^{N+1}\Delta\delta_g) - \dots - t_{e,1}(\frac{\gamma}{2} + i^{N+1}\Delta\delta_g) - i^{N+1}\Delta\delta_g(\tau_N - \tau_{N-1} + \dots - \tau_1)}) \quad (6.13)$$

$$= \frac{\gamma^N}{2^{N+2}\sqrt{2\pi\sigma}} \int_{-\infty}^{\infty} d\Delta\delta_g e^{-\frac{\Delta\delta_g^2}{2\sigma^2}} \int_0^{\infty} \dots \int_0^{\infty} dt_{e,N} \dots dt_{e,2} \\ (\frac{1}{\frac{\gamma}{2} - i^{N+1}\Delta\delta_g} e^{-t_{e,N}(\frac{\gamma}{2} + i^{N+1}\Delta\delta_g) - \dots - t_{e,2}(\frac{\gamma}{2} + i^{N+1}\Delta\delta_g)} \\ e^{i^{N+1}\Delta\delta_g(\tau_N - \tau_{N-1} + \dots - \tau_1)} + \frac{1}{\frac{\gamma}{2} + i^{N+1}\Delta\delta_g} e^{-t_{e,N}(\frac{\gamma}{2} - i^{N+1}\Delta\delta_g) - \dots - t_{e,2}(\frac{\gamma}{2} - i^{N+1}\Delta\delta_g)} \\ e^{-i^{N+1}\Delta\delta_g(\tau_N - \tau_{N-1} + \dots - \tau_1)}) \quad (6.14)$$

$$= \frac{\gamma^N}{2^{N+2}\sqrt{2\pi\sigma}} \int_{-\infty}^{\infty} d\Delta\delta_g e^{-\frac{\Delta\delta_g^2}{2\sigma^2}} \int_0^{\infty} \dots \int_0^{\infty} dt_{e,N} \dots dt_{e,3} \\ (\frac{1}{\frac{\gamma^2}{4} + \Delta\delta_g^2} e^{-t_{e,N}(\frac{\gamma}{2} + i^{N+1}\Delta\delta_g) - \dots - t_{e,3}(\frac{\gamma}{2} - i^{N+1}\Delta\delta_g)} \\ e^{i^{N+1}\Delta\delta_g(\tau_N - \tau_{N-1} + \dots - \tau_1)} + \frac{1}{\frac{\gamma^2}{4} + \Delta\delta_g^2} e^{-t_{e,N}(\frac{\gamma}{2} - i^{N+1}\Delta\delta_g) - \dots - t_{e,3}(\frac{\gamma}{2} + i^{N+1}\Delta\delta_g)} \\ e^{-i^{N+1}\Delta\delta_g(\tau_N - \tau_{N-1} + \dots - \tau_1)}) \quad (6.15)$$

$$= \dots \\ \vdots \\ = \frac{\gamma^N}{2^{N+2}\sqrt{2\pi\sigma}} \int_{-\infty}^{\infty} d\Delta\delta_g e^{-\frac{\Delta\delta_g^2}{2\sigma^2}} \left(\frac{1}{\frac{\gamma^2}{4} + \delta\delta_g^2} \right)^{\frac{N}{2}} \\ (e^{i^{N+1}\Delta\delta_g(\tau_N - \tau_{N-1} + \dots - \tau_1)} + e^{-i^{N+1}\Delta\delta_g(\tau_N - \tau_{N-1} + \dots - \tau_1)}). \quad (6.16)$$

It is difficult to solve (6.16) for general N , so we use a different solution strategy. First we will solve for $N = 2$ and then for $N \rightarrow \infty$. Naturally, all other solutions must lie in between these two solutions.

For $N = 2$ (6.16) becomes

$$F'(\tau_2, \tau_1) = \frac{\gamma^2}{2^4 \sqrt{2\pi}\sigma} \int_{-\infty}^{\infty} d\Delta\delta_g e^{-\frac{\Delta\delta_g^2}{2\sigma^2}} \left(\frac{1}{\frac{\gamma^2}{4} + \Delta\delta_g^2} \right) (e^{i^3 \Delta\delta_g(\tau_2 - \tau_1)} + e^{-i^3 \Delta\delta_g(\tau_2 - \tau_1)}) \quad (6.17)$$

We solve this using the unitarity of the Fourier transform, i.e. we will view this integral as an inner product between two functions and Fourier transform them separately. The two Fourier transformations give

$$\begin{aligned} \mathcal{F} \left[e^{-\frac{\Delta\delta_g^2}{2\sigma^2} \pm i\Delta\delta_g(\tau_2 - \tau_1)} \right] &= \sigma e^{-\frac{1}{2}(\tau_1 - \tau_2 \mp t')^2 \sigma^2} \\ \mathcal{F} \left[\frac{1}{\frac{\gamma^2}{4} + \Delta\delta_g^2} \right] &= \frac{\sqrt{\pi/2}}{\gamma} e^{-\frac{\gamma}{2}t'} (2(e^{\gamma t'} \theta(-t') + \theta(t')), \end{aligned}$$

where $\theta(\pm t')$ are Heaviside step functions.

Hence the Fourier transform of (6.17) is

$$\begin{aligned} \mathcal{F}[F'(\tau_2, \tau_1)] &= \frac{\sqrt{\pi/2}\gamma}{16\sqrt{2\pi}} \int_{-\infty}^{\infty} dt' (e^{-\frac{1}{2}(\tau_1 - \tau_2 + t')^2 \sigma^2} + e^{-\frac{1}{2}(\tau_1 - \tau_2 - t')^2 \sigma^2}) \\ &\quad (e^{-\frac{\gamma}{2}t'} (2(e^{\gamma t'} \theta(-t') + \theta(t')))) \\ &= \frac{\sqrt{\pi/2}\gamma}{8\sigma} e^{\frac{\gamma^2}{4\sigma^2} + \frac{\gamma}{2}(\tau_1 - \tau_2)} \operatorname{erfc} \left(\frac{\gamma + 2\sigma^2(\tau_1 - \tau_2)}{2\sqrt{2}\sigma} \right) \end{aligned} \quad (6.18)$$

This expression can be optimised by using the ability to freely choose the timing of the π -pulses and requiring $\tau_1 = \tau_2$. This requirement is met as long as the time between the first excitation and the first π -pulse is equal to the time between the second excitation and the second π -pulse. Physically, this corresponds to the confined spin spending as much time in $|\uparrow\rangle$ as it does in $|\downarrow\rangle$.

Imposing $\tau_1 = \tau_2$ in (6.18) yields the final solution to (6.16) for $N = 2$

$$F_{\text{visibility}}(\tau_1 = \tau_2) = \frac{1}{2} + \frac{\sqrt{\pi/2}\gamma}{4\sigma} e^{\frac{\gamma^2}{8\sigma^2}} \operatorname{erfc} \left(\frac{\gamma}{2\sqrt{2}\sigma} \right) \quad (6.19)$$

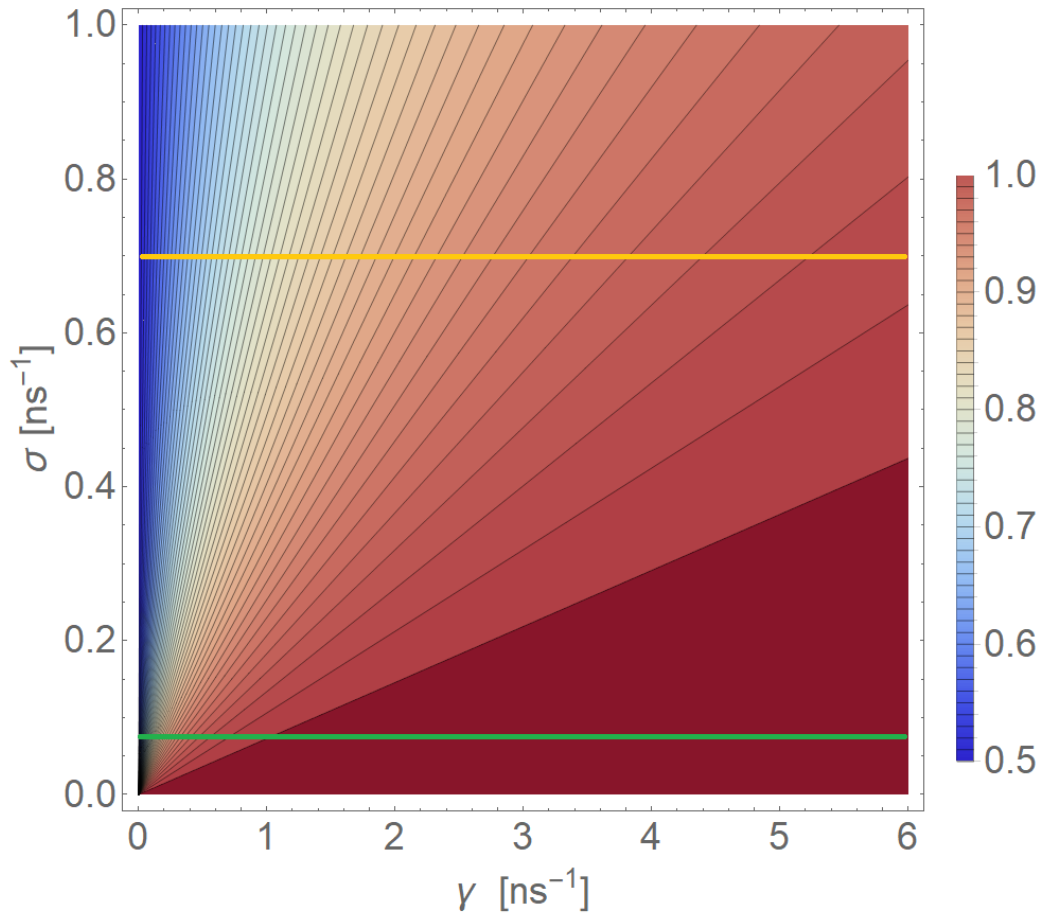


FIGURE 6.2: The visibility fidelity for a time-bin entangled Bell state ($N = 2$) optimised with the condition $\tau_1 = \tau_2$. Each contour line corresponds to a change in fidelity of 0.01. The yellow line marks a usual realistic value for an electron: $\sigma = 0.7 \text{ ns}^{-1}$ (corresponding to a coherence time of $T_2^* = 2 \text{ ns}$). The green line marks a usual realistic values for a hole: $\sigma = 0.7 \text{ ns}^{-1}$ (corresponding to a coherence time of $T_2^* = 20.2 \text{ ns}$).

In fig. 6.2, we see that the visibility fidelity for an electron is increasing significantly with an increasing γ , showing that Purcell enhancement is very beneficial. For a typical coherence time of an electron, $T_2^* = 2 \text{ ns}$, we are able to achieve $F_{\text{visibility}} = 0.975$ at $\gamma = 5.7 \text{ ns}^{-1}$. For a hole, given a coherence time of $T_2^* = 20.2 \text{ ns}$, Purcell enhancement is not necessary since $F_{\text{visibility}} > 0.99$ at $\gamma = 1 \text{ ns}^{-1}$.

We now solve (6.16) in the limit $N \rightarrow \infty$. In this limit the fraction can be approximated using a series expanding as

$$\begin{aligned}
\left(\frac{1}{\frac{\gamma^2}{4} + \Delta\delta_g^2}\right)^{\frac{N}{2}} &= \frac{1}{\left(\frac{\gamma^2}{4}\right)^{\frac{N}{2}} \left(1 + \frac{4\Delta\delta_g^2}{\gamma^2}\right)^{\frac{N}{2}}} \\
&= \frac{2^N}{\gamma^N \left(1 + \frac{4\Delta\delta_g^2}{\gamma^2}\right)^{\frac{N}{2}}} \\
&= \frac{2^N}{\gamma^N} \left(1 + \left(-\frac{4\Delta\delta_g^2}{\gamma^2}\right) + \left(-\frac{4\Delta\delta_g^2}{\gamma^2}\right)^2 + \dots\right)^{\frac{N}{2}} \\
&\approx \frac{2^N}{\gamma^N} \left(1 + \left(-\frac{4\Delta\delta_g^2}{\gamma^2}\right)\right)^{\frac{N}{2}} \\
&= \frac{2^N}{\gamma^N} \left(1 + \frac{N}{2} \left(-\frac{4\Delta\delta_g^2}{\gamma^2}\right) + \frac{N^2}{4} \left(-\frac{2\Delta\delta_g^2}{\gamma^2}\right)^2 + \dots\right) \\
&\approx \frac{2^N}{\gamma^N} e^{-N \frac{4\Delta\delta_g^2}{\gamma^2}}. \tag{6.20}
\end{aligned}$$

Using the approximation in (6.20), the fidelity in (6.16) can in the limit $N \rightarrow \infty$ be expressed as:

$$\begin{aligned}
F'(\tau_N, \dots, \tau_1) &= \frac{1}{4\sqrt{2\pi}\sigma} \int_{-\infty}^{\infty} d\Delta\delta_g e^{-\Delta\delta_g^2 \left(\frac{1}{2\sigma^2} + N \frac{4}{\gamma^2}\right)} \left(e^{-i^{N+1}\Delta\delta_g(\tau_1 - \tau_2 + \dots - \tau_N)} + e^{i^{N+1}\Delta\delta_g(\tau_1 - \tau_2 + \dots - \tau_N)} \right) \\
&= \frac{1}{4\sqrt{2\pi}\sigma} \sqrt{\frac{1}{\frac{1}{2\sigma^2} + N \frac{4}{\gamma^2}}} \left(e^{\frac{(-i^{N+1}(\tau_1 - \tau_2 + \dots - \tau_N))^2}{\frac{2}{\sigma^2} + N \frac{16}{\gamma^2}}} + e^{\frac{(-i^{N+1}(\tau_1 - \tau_2 + \dots - \tau_N))^2}{\frac{2}{\sigma^2} + N \frac{16}{\gamma^2}}} \right) \\
&= \frac{\gamma}{2\sigma\sqrt{4N + \frac{\gamma^2}{\sigma^2}}} e^{-i^{2N}\sigma^2\gamma^2(\tau_1 - \tau_2 + \dots - \tau_N)^2 / (2\gamma^2 + 16N\sigma^2)}
\end{aligned}$$

Similar to the solution for $N = 2$, and by the same argument, we optimize (6.21) by setting the timing of the echo pulses equal to each other pairwise $\tau_1 = \tau_2, \tau_3 = \tau_4, \dots, \tau_{N-1} = \tau_N$, yielding

$$F_{visibility}(\tau_1 = \tau_2, \tau_3 = \tau_4, \dots, \tau_{N-1} = \tau_N) = \frac{1}{2} + \frac{\gamma}{2\sigma\sqrt{4N + \frac{\gamma^2}{\sigma^2}}}. \tag{6.21}$$

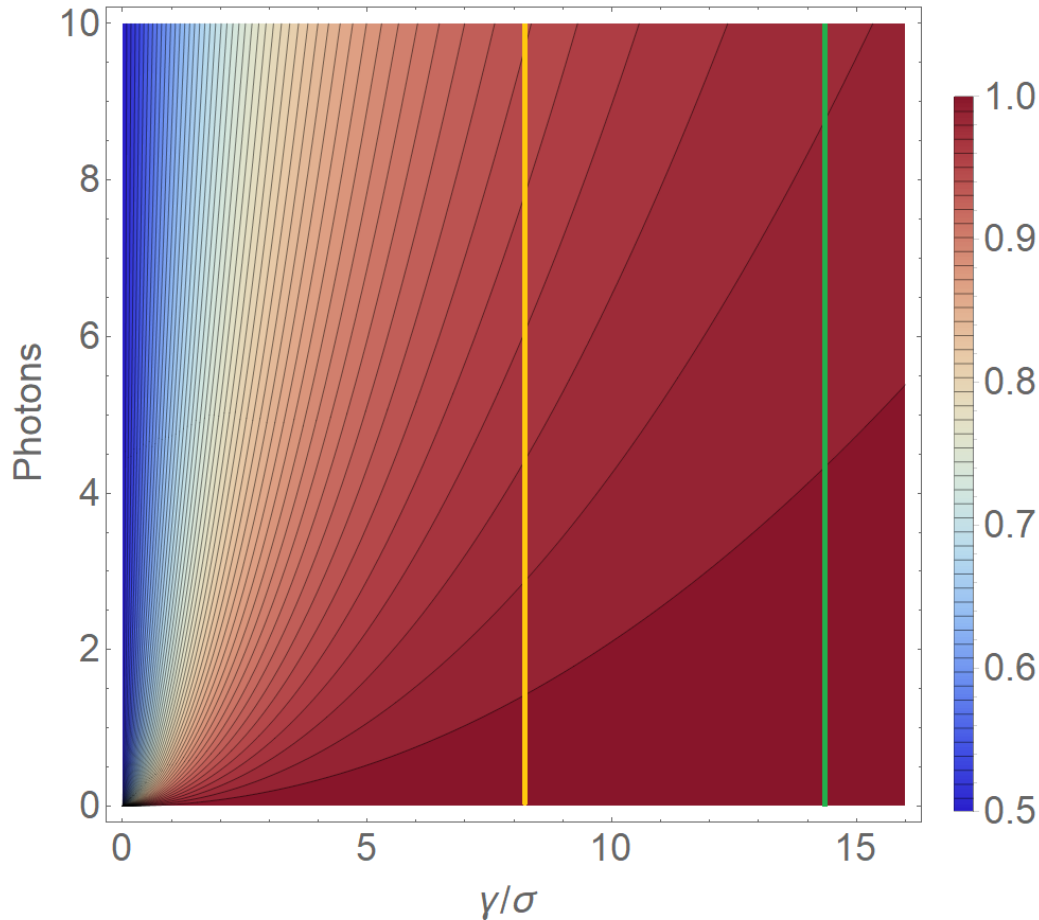


FIGURE 6.3: The visibility fidelity for a time-bin entangled GHZ state in the limit $N \rightarrow \infty$ optimised with the condition $\tau_1 = \tau_2, \tau_3 = \tau_4, \dots, \tau_{N-1} = \tau_N$. Each contour line corresponds to a change in fidelity of 0.01. The yellow line marks the realistic Purcell enhanced values for an electron: $\gamma/\sigma = 5.7 \text{ ns}^{-1}/0.7 \text{ ns}^{-1} = 8.14$. The green line marks the realistic non Purcell enhanced values for a hole: $\gamma/\sigma = 1 \text{ ns}^{-1}/0.07 \text{ ns}^{-1} = 14.29$. Note, since the expression for visibility fidelity is obtained in the limit $N \rightarrow \infty$, the plot becomes more accurate with increasing photon number.

From fig. 6.3 we see that Purcell enhancing the electron to $\gamma = 5.7 \text{ ns}^{-1}$ allows us to create a Bell state with $F_{\text{visibility}} \approx 0.99$ (note that this is in agreement with the visibility fidelity calculated using the solution for $N = 2$). Even creating a four photon GHZ state using an electron is possible with $F_{\text{visibility}} \approx 0.97$. For a hole the predictions are, not surprisingly, even better. Here we can create a four photon GHZ state with $F_{\text{visibility}} \approx 0.99$ and an eight photon GHZ state with $F_{\text{visibility}} \approx 0.98$ without any Purcell enhancement. Purcell enhancing the hole to $\gamma = 5.7 \text{ ns}^{-1}$ would allow us to create a 136 photon GHZ state with $F_{\text{visibility}} \approx 0.99$.

Lastly, we plot both solutions, $N = 2$ and $N \rightarrow \infty$, by scaling the x-axis with $N^{-1/2}$. All solutions for general N lies in between these two curves. A numerical calculation of this result is presented in appendix C which agrees with the prediction shown in fig. 6.4

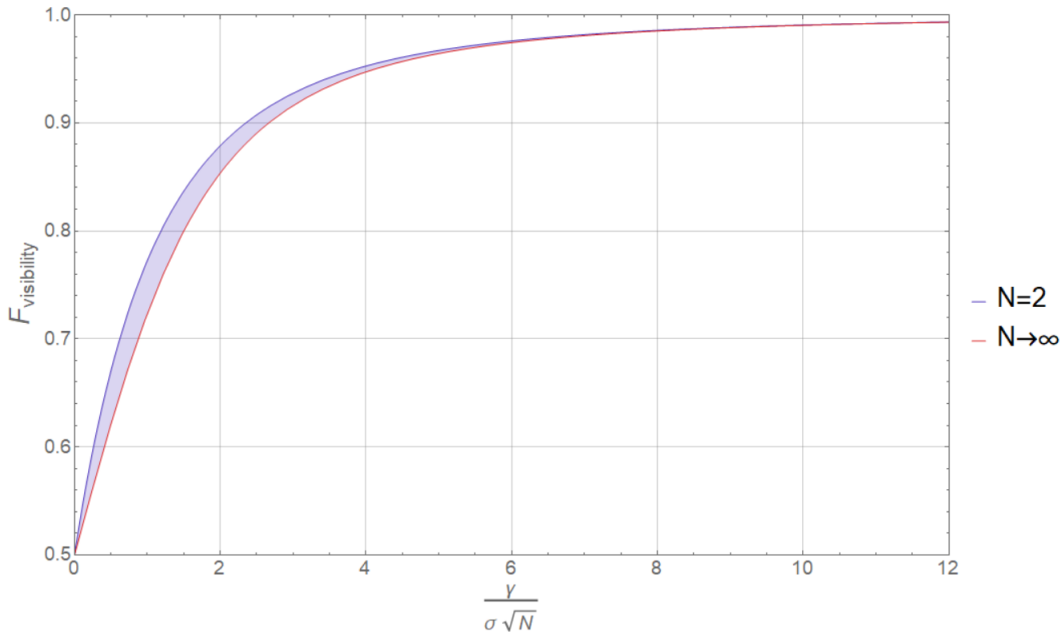


FIGURE 6.4: Scaling the x-axis by $1/\sqrt{N}$ allows us to plot both solutions of the visibility fidelity. Solutions for general N lies in between the two curves.

Now, the take-home message from this section is as follows: in the time-bin spin-photon entanglement protocol, overcoming the Overhauser field and obtaining a high visibility is a manageable problem with current values for γ and σ . The visibility fidelity is good for an electron and great for a hole. The reason that the visibility is better for time-bin entanglement than the frequency entanglement protocol is that in the time-bine entanglement protocol the visibility is no longer limited by the resolution of the detector and the strength of the applied magnetic field. This dependency, or lack of dependency, can easily be shown by comparing the perturbative expansion of the visibility fidelity for a single photon for the two protocols:

$$F_{visibility}^{frequency} = 1 - \frac{2\sigma^2}{\gamma^2} - \frac{(\delta_g \epsilon)^2}{4} \quad (6.22)$$

$$F_{visibility}^{time-bin} = 1 - \frac{2\sigma^2}{\gamma^2}. \quad (6.23)$$

6.2 Imperfect Decay Ratio and Photon Loss

Section 6.1 demonstrated that imperfect visibility of the system due to the Overhauser field is indeed a manageable problem exploiting Purcell enhancement, however, we have so far made assumptions about the decay. We have assumed that only the transition between the two closest energy levels in the ground state and excited state where possible and that emitted photons are always measured by the detector. This section is devoted to studying a more complex decay structure and photon loss. Specifically, how imperfect decay ratios (lambda decay) and photon loss alter the generated quantum state. These two effects are visualised in fig. 6.5 which shows an effective level diagram with additional decay paths and the possibility to loose the emitted photon before it is measured. We refer to the collective measure of these imperfections as decay fidelity. We shall express this measure as a *conditional fidelity* using the density

matrix formalism. By "conditional" we simply mean that if we excited the quantum dot N times, we only accept a result where the detector observes $N/2$ photons in the expected time-order.

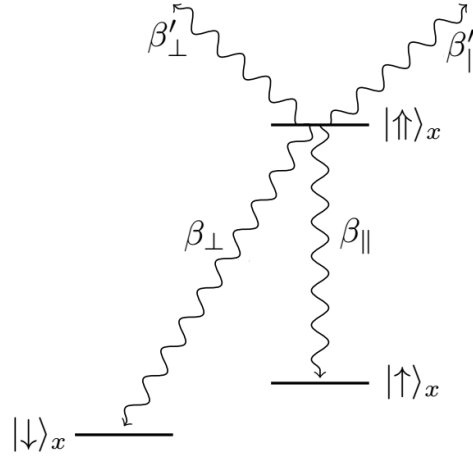


FIGURE 6.5: Effective level diagram with three additional decay paths. β_{\parallel} (β_{\perp}) is the probability for the spin to decay into the good (bad) ground state while the emitted photon is detected. β'_{\parallel} (β'_{\perp}) is the probability for the spin to decay into the good (bad) ground state while the emitted photon is lost before it is measured.

Before we calculate the decay fidelity, we must determine which spin-photon quantum state our time-bin entanglement protocol produces, if we include all four decay paths. This corresponds to the output state of the system.

6.2.1 The Output State

In this section, the output state of the system including the additional possible decay paths is examined. In order to simplify the calculations performed, the applied notation is first defined: " γ_{\rightarrow} " referees to a decay from the excited state, now emitting a photon into the four decay paths. " π_{\rightarrow} " referees to a ground state spin flip. When the excited state decays into wrong state (since we have chosen a electron as the confined spin, the correct ground state is $|\uparrow\rangle$ and the wrong state is $|\downarrow\rangle$) then the emitted photon has higher energy than a photon produced from a decay into the correct ground state. An early (late) photon with higher energy is denoted as $|e'\rangle$ ($|l'\rangle$). A lost photon is denoted $|\phi\rangle$.

Initializing the ground state in an equal superposition of spin up and down, the

produced spin-photon quantum state is

$$\frac{1}{\sqrt{2}}(|\uparrow\rangle + |\downarrow\rangle) \xrightarrow{\gamma} \frac{1}{\sqrt{2}} \left(\sqrt{\beta_{\parallel}} |\uparrow\rangle |e\rangle + \sqrt{\beta'_{\parallel}} |\uparrow\rangle |\phi\rangle + \sqrt{\beta_{\perp}} |\downarrow\rangle |e'\rangle + \sqrt{\beta'_{\perp}} |\downarrow\rangle |\phi\rangle + |\downarrow\rangle |0\rangle \right) \quad (6.24)$$

$$\xrightarrow{\pi} \frac{1}{\sqrt{2}} \left(-\sqrt{\beta_{\parallel}} |\downarrow\rangle |e\rangle - \sqrt{\beta'_{\parallel}} |\downarrow\rangle |\phi\rangle + \sqrt{\beta_{\perp}} |\uparrow\rangle |e'\rangle + \sqrt{\beta'_{\perp}} |\uparrow\rangle |\phi\rangle + |\uparrow\rangle |0\rangle \right) \quad (6.25)$$

$$\xrightarrow{\gamma} \frac{1}{\sqrt{2}} \left(-\sqrt{\beta_{\parallel}} |\downarrow\rangle |0, e\rangle - \sqrt{\beta'_{\parallel}} |\downarrow\rangle |0, \phi\rangle + \sqrt{\beta_{\perp}} \left(\sqrt{\beta_{\parallel}} |\uparrow\rangle |l\rangle + \sqrt{\beta'_{\parallel}} |\uparrow\rangle |\phi\rangle + \sqrt{\beta_{\perp}} |\downarrow\rangle |l'\rangle + \sqrt{\beta'_{\perp}} |\downarrow\rangle |\phi\rangle \right) |e'\rangle + \sqrt{\beta'_{\perp}} \left(\sqrt{\beta_{\parallel}} |\uparrow\rangle |l\rangle + \sqrt{\beta'_{\parallel}} |\uparrow\rangle |\phi\rangle + \sqrt{\beta_{\perp}} |\downarrow\rangle |l'\rangle + \sqrt{\beta'_{\perp}} |\downarrow\rangle |\phi\rangle \right) |\phi\rangle + \left(\sqrt{\beta_{\parallel}} |\uparrow\rangle |l\rangle + \sqrt{\beta'_{\parallel}} |\uparrow\rangle |\phi\rangle + \sqrt{\beta_{\perp}} |\downarrow\rangle |l'\rangle + \sqrt{\beta'_{\perp}} |\downarrow\rangle |\phi\rangle \right) |0\rangle \right) \quad (6.26)$$

$$= \frac{1}{\sqrt{2}} \left(-\sqrt{\beta_{\parallel}} |\downarrow\rangle |0, e\rangle - \sqrt{\beta'_{\parallel}} |\downarrow\rangle |0, \phi\rangle + \sqrt{\beta_{\perp} \beta_{\parallel}} |\uparrow\rangle |l, e'\rangle + \sqrt{\beta_{\perp} \beta'_{\parallel}} |\uparrow\rangle |\phi, e'\rangle + \beta_{\perp} |\downarrow\rangle |l', e'\rangle + \sqrt{\beta_{\perp} \beta'_{\perp}} |\downarrow\rangle |\phi, e'\rangle + \sqrt{\beta'_{\perp} \beta_{\parallel}} |\uparrow\rangle |l, \phi\rangle + \sqrt{\beta'_{\perp} \beta'_{\parallel}} |\uparrow\rangle |\phi, \phi\rangle + \sqrt{\beta'_{\perp} \beta_{\perp}} |\downarrow\rangle |l', \phi\rangle + \beta'_{\perp} |\downarrow\rangle |\phi, \phi\rangle + \sqrt{\beta_{\parallel}} |\uparrow\rangle |l, 0\rangle + \sqrt{\beta'_{\parallel}} |\uparrow\rangle |\phi, 0\rangle + \sqrt{\beta_{\perp}} |\downarrow\rangle |l', 0\rangle + \sqrt{\beta'_{\perp}} |\downarrow\rangle |\phi, 0\rangle \right) \quad (6.27)$$

$$\xrightarrow{\pi} \frac{1}{\sqrt{2}} \left(-\sqrt{\beta_{\parallel}} |\uparrow\rangle |0, e\rangle - \sqrt{\beta'_{\parallel}} |\uparrow\rangle |0, \phi\rangle - \sqrt{\beta_{\perp} \beta_{\parallel}} |\downarrow\rangle |l, e'\rangle - \sqrt{\beta_{\perp} \beta'_{\parallel}} |\downarrow\rangle |\phi, e'\rangle + \beta_{\perp} |\uparrow\rangle |l', e'\rangle + \sqrt{\beta_{\perp} \beta'_{\perp}} |\uparrow\rangle |\phi, e'\rangle - \sqrt{\beta'_{\perp} \beta_{\parallel}} |\downarrow\rangle |l, \phi\rangle - \sqrt{\beta'_{\perp} \beta'_{\parallel}} |\downarrow\rangle |\phi, \phi\rangle + \sqrt{\beta'_{\perp} \beta_{\perp}} |\uparrow\rangle |l', \phi\rangle + \beta'_{\perp} |\uparrow\rangle |\phi, \phi\rangle - \sqrt{\beta_{\parallel}} |\downarrow\rangle |l, 0\rangle - \sqrt{\beta'_{\parallel}} |\downarrow\rangle |\phi, 0\rangle + \sqrt{\beta_{\perp}} |\uparrow\rangle |l, 0\rangle + \sqrt{\beta'_{\perp}} |\uparrow\rangle |\phi, 0\rangle \right).$$

Evidently, the spin-photon state rapidly becomes unmanageable. A state created from two excitations has 14 terms. A state created from 4 excitations can be shown to have 104 terms, so it is clearly not feasible to generalise the produced spin-photon state. As we shall see, it is possible to obtain a conditional decay fidelity for a general number of photons without knowing the generalised state. The reason being the condition previously mentioned: if we excited the quantum dot N times, we only accept a result where the detector observes $N/2$ photons in the correct time-order. This condition tremendously simplifies the density matrix. We shall refer to this density matrix as the conditional density matrix, from which we can calculate the conditional decay fidelity.

6.2.2 The Conditional Decay Fidelity

The conditional density matrix is a sub-ensemble of the regular density matrix. A sub-ensemble for which a measurement yields the value α_i is, in general, described as

$$\hat{\rho}_i = \frac{P_i \hat{\rho} P_i}{\text{Tr}[P_i \hat{\rho}]}, \quad (6.29)$$

where $\hat{\rho}$ is the density matrix and P_i is an operator projecting $\hat{\rho}$ into the sub-ensemble $\hat{\rho}_i$. In our case the sub-ensemble of interest is where we detect exactly $N/2$ photons if we excite the quantum dot N times and where we only accept results where each photon arrive at the detector at the expected time. Thus we write the conditional density matrix as:

$$\hat{\rho}_c = \frac{P_{\frac{N}{2}} \hat{\rho} P_{\frac{N}{2}}}{\text{Tr}[P_{\frac{N}{2}} \hat{\rho}]}, \quad (6.30)$$

where $P_{\frac{N}{2}}$ are projection operators enforcing the conditions discussed above and $\text{Tr}[P_{\frac{N}{2}} \hat{\rho}]$ is the probability of detecting $N/2$ photons in the correct time-order.

From the conditional density matrix (6.30) we define the conditional decay fidelity as

$$F_c = \langle \psi_{ideal,GHZ}^{N/2} | \hat{\rho}_c | \psi_{ideal,GHZ}^{N/2} \rangle \quad (6.31)$$

$$= \frac{1}{\text{Tr}[P_{\frac{N}{2}} \hat{\rho}]} \langle \psi_{ideal,GHZ}^{N/2} | P_{\frac{N}{2}} \hat{\rho} P_{\frac{N}{2}} | \psi_{ideal,GHZ}^{N/2} \rangle, \quad (6.32)$$

where

$$|\psi_{ideal,GHZ}^{N/2}\rangle = \frac{1}{\sqrt{2}} (|\uparrow\rangle |0, e\rangle \otimes^{\otimes \frac{N}{2}} + |\downarrow\rangle |l, 0\rangle \otimes^{\otimes \frac{N}{2}}). \quad (6.33)$$

The equation defining the conditional fidelity (6.32) is now solved by first considering the expression in the numerator and then the expression in the denominator. Starting with the numerator, we calculate the projected density matrix for $N = 2$. The projection operator is

$$P_{\frac{N}{2}=1} = |0, e\rangle \langle 0, e| + |\phi, e'\rangle \langle \phi, e'| + |l, 0\rangle \langle l, 0| + |l', \phi\rangle \langle l', \phi| + |l', 0\rangle \langle l', 0|. \quad (6.34)$$

The definition of the projection operator (6.34) is important if one wishes to apply the results found in this section. Since $P_{N/2=1}$ removes the two states containing two photons in (6.29), $|l, e'\rangle$ and $|l', e'\rangle$, the experimental setup should be designed such that these two states can be discarded. A photon-number-resolving detector would be a possible solution, however, current photon-number-resolving detectors show inadequate performance [46] for our purpose. Fortunately there is a better solution. Implementing a frequency filter will remove the unwanted states as they both contain high energy photons emitted by the decay path β_{\perp} .

The density matrix becomes

$$\begin{aligned}
P_{\frac{N}{2}=1} \hat{\rho} P_{\frac{N}{2}=1} &= \frac{1}{2} (|0, e\rangle \langle 0, e| + |\phi, e'\rangle \langle \phi, e'| + |l, 0\rangle \langle l, 0| + |l', \phi\rangle \langle l', \phi| \\
&\quad + |l', 0\rangle \langle l', 0|) (-\sqrt{\beta_{\parallel}} |\uparrow\rangle |0, e\rangle - \sqrt{\beta'_{\parallel}} |\uparrow\rangle |0, \phi\rangle \\
&\quad - \sqrt{\beta_{\perp} \beta_{\parallel}} |\downarrow\rangle |l, e'\rangle - \sqrt{\beta_{\perp} \beta'_{\parallel}} |\downarrow\rangle |\phi, e'\rangle + \beta_{\perp} |\uparrow\rangle |l', e'\rangle \\
&\quad + \sqrt{\beta_{\perp} \beta'_{\perp}} |\uparrow\rangle |\phi, e'\rangle - \sqrt{\beta'_{\perp} \beta_{\parallel}} |\downarrow\rangle |l, \phi\rangle - \sqrt{\beta'_{\perp} \beta'_{\parallel}} |\downarrow\rangle |\phi, \phi\rangle \\
&\quad + \sqrt{\beta'_{\perp} \beta_{\perp}} |\uparrow\rangle |l', \phi\rangle + \beta'_{\perp} |\uparrow\rangle |\phi, \phi\rangle - \sqrt{\beta_{\parallel}} |\downarrow\rangle |l, 0\rangle \\
&\quad - \sqrt{\beta'_{\parallel}} |\downarrow\rangle |\phi, 0\rangle + \sqrt{\beta_{\perp}} |\uparrow\rangle |l', 0\rangle + \sqrt{\beta'_{\perp}} |\uparrow\rangle |\phi, 0\rangle) \\
&\quad (-\sqrt{\beta_{\parallel}} \langle \uparrow | \langle 0, e| - \sqrt{\beta'_{\parallel}} \langle \uparrow | \langle 0, \phi| - \sqrt{\beta_{\perp} \beta_{\parallel}} \langle \downarrow | \langle l, e'| \quad (6.35) \\
&\quad - \sqrt{\beta_{\perp} \beta'_{\parallel}} \langle \downarrow | \langle \phi, e'| + \beta_{\perp} \langle \uparrow | \langle l', e'| + \sqrt{\beta_{\perp} \beta'_{\perp}} \langle \uparrow | \langle \phi, e'| \\
&\quad - \sqrt{\beta'_{\perp} \beta_{\parallel}} \langle \downarrow | \langle l, \phi| - \sqrt{\beta'_{\perp} \beta'_{\parallel}} \langle \downarrow | \langle \phi, \phi| + \sqrt{\beta'_{\perp} \beta_{\perp}} \langle \uparrow | \langle l', \phi| \\
&\quad + \beta'_{\perp} \langle \uparrow | \langle \phi, \phi| - \sqrt{\beta_{\parallel}} \langle \downarrow | \langle l, 0| - \sqrt{\beta'_{\parallel}} \langle \downarrow | \langle \phi, 0| + \sqrt{\beta_{\perp}} \langle \uparrow | \langle l', 0| \\
&\quad + \sqrt{\beta'_{\perp}} \langle \uparrow | \langle \phi, 0|) (|0, e\rangle \langle 0, e| + |\phi, e'\rangle \langle \phi, e'| \\
&\quad + |l, 0\rangle \langle l, 0| + |l', \phi\rangle \langle l', \phi| + |l', 0\rangle \langle l', 0|) \\
&= \frac{1}{2} (-\sqrt{\beta_{\parallel}} |\uparrow\rangle |0, e\rangle - \sqrt{\beta_{\perp} \beta'_{\parallel}} |\downarrow\rangle |\phi, e'\rangle + \sqrt{\beta_{\perp} \beta'_{\perp}} |\uparrow\rangle |\phi, e'\rangle \\
&\quad - \sqrt{\beta'_{\perp} \beta_{\parallel}} |\downarrow\rangle |l, \phi\rangle + \sqrt{\beta'_{\perp} \beta_{\perp}} |\uparrow\rangle |l', \phi\rangle - \sqrt{\beta_{\parallel}} |\downarrow\rangle |l, 0\rangle \\
&\quad + \sqrt{\beta_{\perp}} |\uparrow\rangle |l', 0\rangle) (-\sqrt{\beta_{\parallel}} \langle \uparrow | \langle 0, e| - \sqrt{\beta_{\perp} \beta'_{\parallel}} \langle \downarrow | \langle \phi, e'| \quad (6.36) \\
&\quad + \sqrt{\beta_{\perp} \beta'_{\perp}} \langle \uparrow | \langle \phi, e'| - \sqrt{\beta'_{\perp} \beta_{\parallel}} \langle \downarrow | \langle l, \phi| + \sqrt{\beta'_{\perp} \beta_{\perp}} \langle \uparrow | \langle l', \phi| \\
&\quad - \sqrt{\beta_{\parallel}} \langle \downarrow | \langle l, 0| + \sqrt{\beta_{\perp}} \langle \uparrow | \langle l', 0|).
\end{aligned}$$

To complete the calculation of the numerator we determine the overlap with the ideal state for $N = 2$, which gives

$$\begin{aligned}
\langle \psi_{ideal,GHZ}^{N/2=1} | P_1 \rho P_1 | \psi_{ideal,GHZ}^{N/2=1} \rangle &= \frac{1}{4} \left(\langle \uparrow | \langle 0, e | + \langle \downarrow | \langle l, 0 | \right) \left(-\sqrt{\beta_{\parallel}} |\uparrow\rangle |0, e\rangle \right. \\
&\quad - \sqrt{\beta_{\perp} \beta'_{\parallel}} |\downarrow\rangle |\phi, e'\rangle + \sqrt{\beta_{\perp} \beta'_{\perp}} |\uparrow\rangle |\phi, e'\rangle \\
&\quad - \sqrt{\beta'_{\perp} \beta_{\parallel}} |\downarrow\rangle |l, \phi\rangle + \sqrt{\beta'_{\perp} \beta_{\perp}} |\uparrow\rangle |l', \phi\rangle \\
&\quad \left. - \sqrt{\beta_{\parallel}} |\downarrow\rangle |l, 0\rangle + \sqrt{\beta_{\perp}} |\uparrow\rangle |l', 0\rangle \right) \\
&\quad \left(-\sqrt{\beta_{\parallel}} \langle \uparrow | \langle 0, e | - \sqrt{\beta_{\perp} \beta'_{\parallel}} \langle \downarrow | \langle \phi, e' | \right. \\
&\quad + \sqrt{\beta_{\perp} \beta'_{\perp}} \langle \uparrow | \langle \phi, e' | - \sqrt{\beta'_{\perp} \beta_{\parallel}} \langle \downarrow | \langle l, \phi | \\
&\quad + \sqrt{\beta'_{\perp} \beta_{\perp}} \langle \uparrow | \langle l', \phi | - \sqrt{\beta_{\parallel}} \langle \downarrow | \langle l, 0 | \\
&\quad \left. + \sqrt{\beta_{\perp}} \langle \uparrow | \langle l', 0 | \right) \left(|\uparrow\rangle |0, e\rangle + |\downarrow\rangle |l, 0\rangle \right) \\
&= \beta_{\parallel}, \tag{6.38}
\end{aligned}$$

where β_{\parallel} represents the probability that the spin decays into the good ground state while the emitted photon is detected, see fig. 6.5. This shows that the state is immensely simplified by the applied conditions and the calculated overlap with the ideal GHZ state, as expected. Evidently so much that the only possible way to generate a state complying with this is if and only if the spin decays into the correct state after every excitation without any photon loss. This is, in fact, true for any number of created photons, hence

$$\langle \psi_{ideal,GHZ}^{N/2} | P_{\frac{N}{2}} \hat{\rho} P_{\frac{N}{2}} | \psi_{ideal,GHZ}^{N/2} \rangle = \beta_{\parallel}^{N/2} \tag{6.39}$$

Now we will evaluate the denominator of the conditional density fidelity (6.32), which is the probability of detecting $N/2$ photons. We write this as $\text{Tr}[P_{\frac{N}{2}} \rho]$, where ρ is given by (6.29). Instead of explicitly calculating the probability, it is possible to imagine every scenario which can create these $N/2$ photons. We imagine 4 possible scenarios, which, if we excite the quantum dot twice, would lead to the detection of a single photon. The 4 scenarios are

1. Everything goes according to plan. This happens with probability β_{\parallel} .
2. The second excitation, which creates the late photon, goes to the bad state but still hits the detector. This happens with probability $\frac{1}{2}\beta_{\perp}$.
3. The first excitation creates a photon which hits the detector, but the spin ends up in the bad state. The photon from the second excitation is lost and the spin ends up in either the good or bad state. This happens with probability $\frac{1}{2}\beta_{\perp}(\beta'_{\perp} + \beta'_{\parallel})$
4. The photon from the first excitation is lost and the spin ends up in the bad state. The photon from the second excitation hits the detector and the spin ends up in either the good or bad state. This happens with probability $\frac{1}{2}\beta'_{\perp}(\beta_{\perp} + \beta_{\parallel})$.

Hence the total probability of detecting a single photon, if we excite the quantum dot twice, is

$$\text{Tr}[P_{\frac{N}{2}=1}\rho] = \left(\frac{1}{2}(2\beta_{\parallel} + \beta_{\perp} + \beta_{\perp}(\beta'_{\perp} + \beta'_{\parallel}) + \beta'_{\perp}(\beta_{\perp} + \beta_{\parallel})) \right), \quad (6.40)$$

which we generalize to $N/2$ photons giving

$$\text{Tr}[P_{\frac{N}{2}}\rho] = \left(\frac{1}{2}(2\beta_{\parallel} + \beta_{\perp} + \beta_{\perp}(\beta'_{\perp} + \beta'_{\parallel}) + \beta'_{\perp}(\beta_{\perp} + \beta_{\parallel})) \right)^{\frac{N}{2}}. \quad (6.41)$$

When applying the generalisation in (6.41), it is assumed that each time a new photon is created, the spin is in the correct superposition. Or, in other words, we have not taken into account that errors can propagate from the creation of a photon to the next photon. This is clearly possible in scenario 2-4 since the spin here can end up in the bad state. As a consequence the generalisation to $N/2$ photons only holds true, strictly speaking, if scenario 1 is dominant, i.e. $\beta_{\parallel} \sim 1$. If the branching ration is sufficiently bad and/or the system is sufficiently lossy, the generalisation breaks down.

Both the numerator and denominator have now been evaluated in (6.39) and (6.41) respectively, so the conditional decay fidelity (6.32) can be determined. After rewriting the expression to a simplified form, the conditional decay fidelity becomes:

$$F_c = \left(1 + \frac{\beta_{\perp}}{2\beta_{\parallel}}(1 + 2\beta'_{\perp} + \beta'_{\parallel}) + \frac{\beta'_{\perp}}{2} \right)^{-N/2}. \quad (6.42)$$

The remaining part of this section is devoted to a discussion of the result in (6.42). In this discussion, it is beneficial to redefine the parameters by deconstructing them. The probabilities introduced in these redefinitions are visualised in fig. 6.6 which shows a schematic drawing of the setup. This is easiest done by first defining the following probabilities:

$$\beta'_{\perp} = \beta'_{\perp,QD} + \beta_{\perp}(1 - \eta_{\perp}) \quad (6.43)$$

$$\beta'_{\parallel} = \beta'_{\parallel,QD} + \beta_{\parallel}(1 - \eta_{\parallel}), \quad (6.44)$$

where $\beta'_{\perp,QD}$ ($\beta'_{\parallel,QD}$) is the probability of losing a photon at the moment of emission such that it never couples into the desired waveguide mode, but instead into a free space mode, while the spin ends up in the bad (good) state and η_{\perp} (η_{\parallel}) is the probability of collecting and detecting a high energy photon (low energy photon) after it is coupled into the waveguide mode. This includes collecting the photon from the waveguide, the subsequent propagation loss and detector inefficiency. Also, in the case of η_{\perp} , the aforementioned frequency cavity can be included. If the cavity filters out all high energy photons then $\eta_{\perp} = 0$. We shall assume the two loss parameters $\beta'_{\perp,QD}$ and $\beta'_{\parallel,QD}$ to be equal and write them as a single parameter defined as the probability that an emitted photon couples into a free space mode instead of the waveguide: $\beta'_{\perp,QD} = \beta'_{\parallel,QD} = \beta_{fs}/2$.

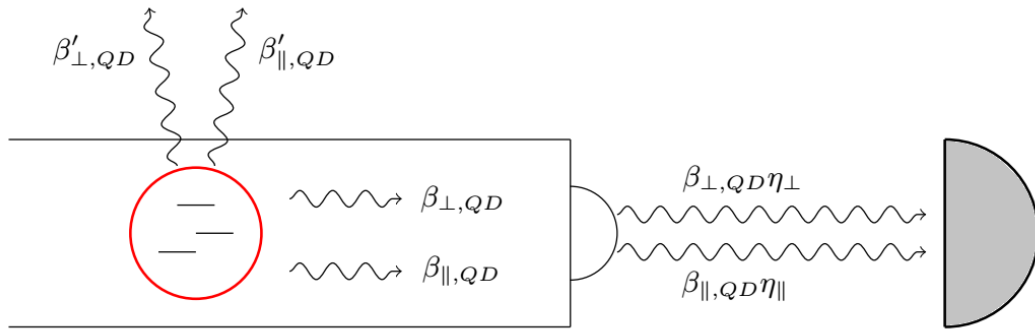


FIGURE 6.6: Schematic drawing of the setup illustrating the probabilities introduced in (6.43)-(6.46). The red circle represents the quantum dot placed in a waveguide and the shaded semi circle represents the photon detector.

Since β_{\perp} and β_{\parallel} are the probabilities of detecting a photon, we can write them as

$$\beta_{\perp} = \beta_{\perp,QD}\eta_{\perp} \quad (6.45)$$

$$\beta_{\parallel} = \beta_{\parallel,QD}\eta_{\parallel}, \quad (6.46)$$

where $\beta_{\perp,QD}$ ($\beta_{\parallel,QD}$) is the probability for the low (high) energy photon to be emitted into the waveguide. These two probabilities are connected to β_{fs} via conservation of probability: $\beta_{fs} = 1 - \beta_{\perp,QD} - \beta_{\parallel,QD}$. The probability β_{fs} can be obtained from the β factor (see section 3.2.1) where, as previously mentioned, a value of $\beta \approx 0.98$ has been observed corresponding to $\beta_{fs} = 0.02$ and $\beta_{\perp,QD} + \beta_{\parallel,QD} = 0.98$.

Figure 6.7 and 6.8 show the conditional decay fidelity for a single photon without and with a frequency filter applied.

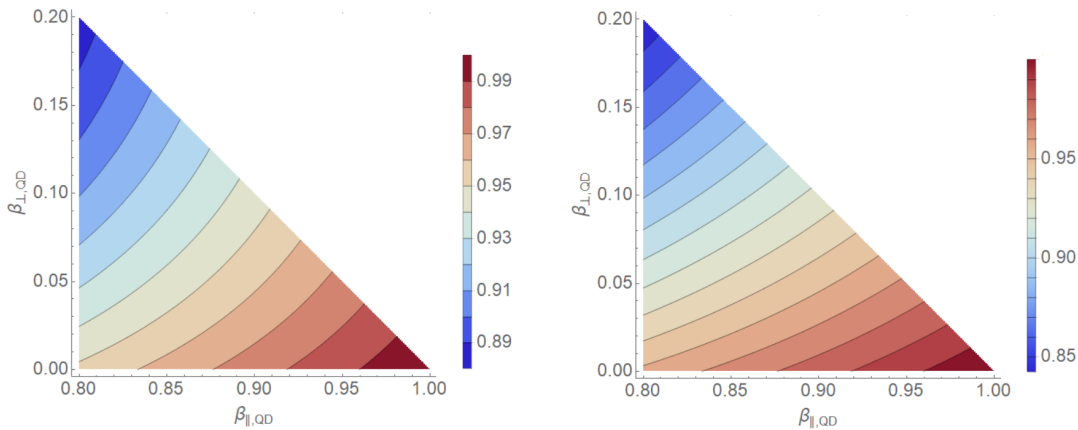


FIGURE 6.7: The conditional decay fidelity for a single photon without a frequency filter. Each contour line corresponds to a change in the fidelity of 0.01. In **a** we have chosen $\eta_{\perp} = \eta_{\parallel} = 0.025$ and in **b** $\eta_{\perp} = \eta_{\parallel} = 0.45$.

Figure 6.7 shows that if the probability of collecting and detecting a photon is increased, an increased dependence on the branching ratio $\beta_{\perp,QD}/\beta_{\parallel,QD}$ is evident. This is because detecting a good photon does less good than detecting a bad photon

does bad. Hence, improving the collection and detection probability is not beneficial unless the unwanted high energy photons are filtered. This is shown in fig. 6.8.

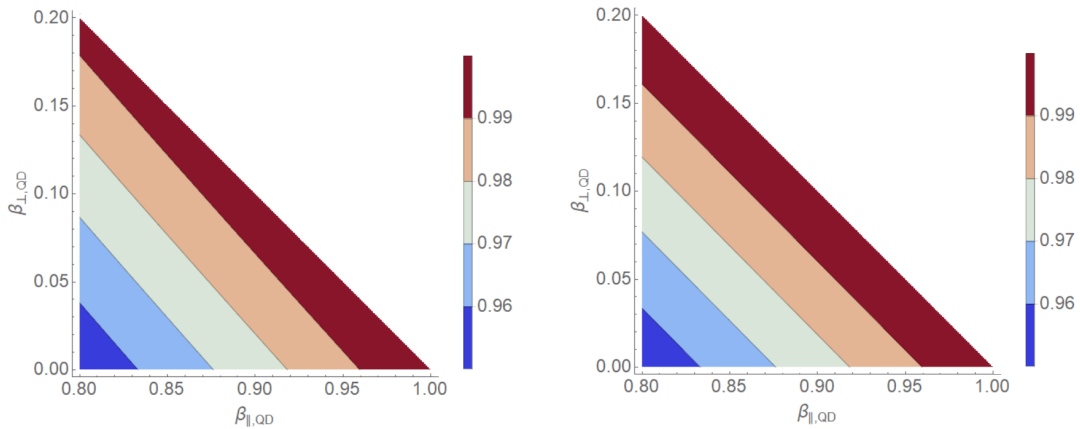


FIGURE 6.8: The conditional decay fidelity for a single photon with a frequency cavity. Each contour line corresponds to a change in the fidelity of 0.01. We have chosen $\beta'_{\perp,QD} + \beta'_{\parallel,QD} = 0.02$. In **a** we have chosen $\eta_{\perp} = 0.001$ and $\eta_{\parallel} = 0.025$ and in **b** $\eta_{\perp} = 0.001$ and $\eta_{\parallel} = 0.05$.

Clearly a nearly perfect frequency filter relaxes the dependency on $\beta_{\perp,QD}/\beta_{\parallel,QD}$ significantly. For $\eta_{\perp} = 0.001$ and $\eta_{\parallel} = 0.05$ (fig. 6.8b), the dependence is approximately gone. In this case is the only remaining dependency of β_{fs} which can be obtained from the β factor (see section 3.2.1) where, as previously mentioned, a value of $\beta \approx 0.98$ has been observed. This corresponds to $\beta_{fs} = 0.02$ achieving $F_c \approx 1$. For $\eta_{\perp} = 0.001$ and $\eta_{\parallel} = 0.025$ (fig. 6.8a), where we see a small dependency on the branching ratio, $F_c > 0.99$ can be achieved by $\beta_{\perp,QD}/\beta_{\parallel,QD} \lesssim 0.09$ when $\beta_{fs} = 0.02$.

Note that the frequency filter reduces the efficiency, i.e. the repetition rate of the protocol, hence a low branching ratio is still desirable if one wishes to obtain a high efficiency.

As a final remark of this section, we will discuss the generation of GHZ states. Figure 6.9 shows the conditional decay fidelity as a function of the number of photons in the GHZ state given five different values of β_{fs} . It is found that we can achieve $F_c \approx 0.945$ for a 5 photon GHZ state if we include a nearly perfect frequency filter and a free space coupling of $\beta_{fs} = 0.02$. Reducing the free space coupling by a factor of 10 would yield $F_c \approx 0.99$ for a 5 photon state and increasing it with a factor of 2 would yield $F_c \approx 0.9$, hence β_{fs} is vital if we wish to create GHZ states.

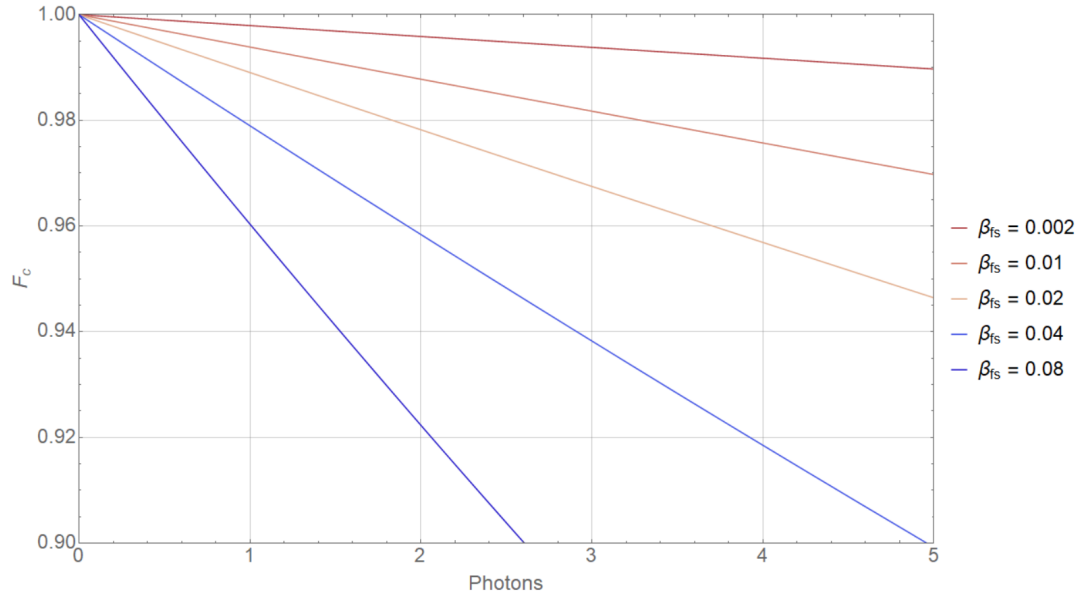


FIGURE 6.9: Conditional decay fidelity for a GHZ state with $\eta_{\perp} = 0.001$, $\eta_{\parallel} = 0.025$ and $\beta_{\perp,QD}/\beta_{\parallel,QD} = 0.05$.

As hinted in fig. 6.8a, implementing a frequency filter still leaves us with a considerable dependence on $\beta_{\perp,QD}/\beta_{\parallel,QD}$ if η_{\parallel} is too low. This effect is further studied in fig. 6.10. A value of $\beta_{\perp,QD}/\beta_{\parallel,QD} \approx 0.01$ is seen to be sufficient to achieve a reasonable decay fidelity for the chosen loss and detection probabilities.

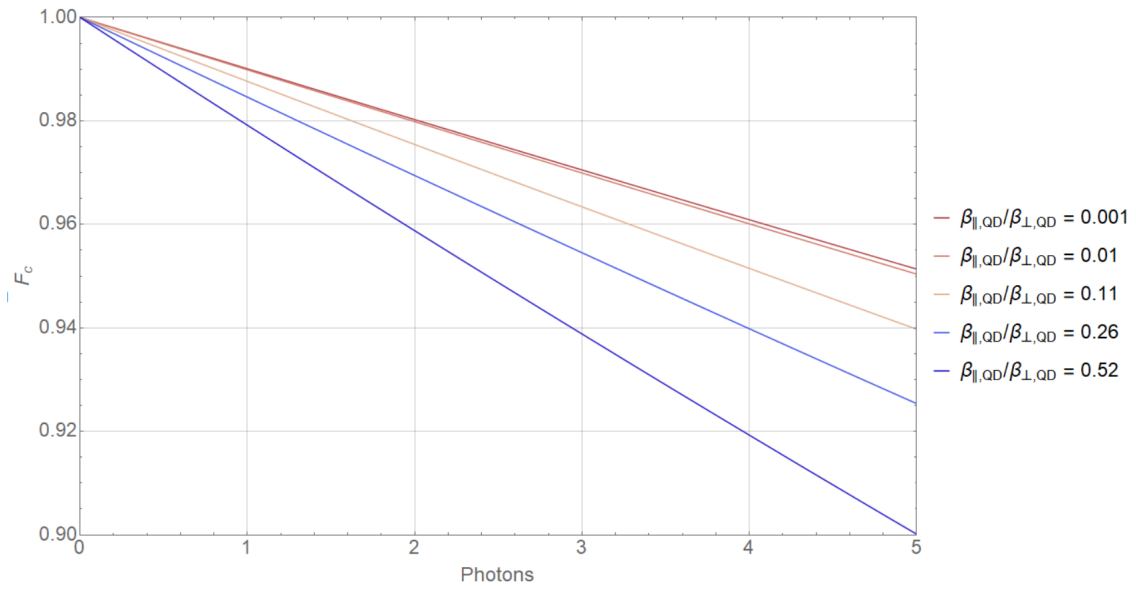


FIGURE 6.10: Conditional decay fidelity for a GHZ state with $\eta_{\perp} = 0.001$, $\eta_{\parallel} = 0.025$ and $\beta_{fs} = 0.02$

6.3 Phonon Induced Pure Dephasing

The last imperfection we will study for the time-bin entanglement protocol is pure dephasing of the trion induced by scattering phonons as shown in fig. 6.11. While the spin is excited, phonons can scatter upon the trion and thereby inducing a random phase γ_d .

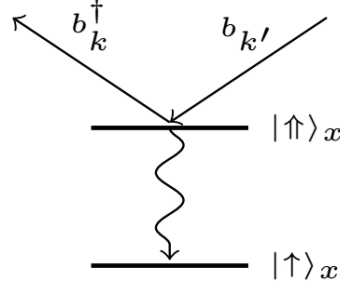


FIGURE 6.11: Effective level diagram showing an incoming phonon with wavenumber k' scatter upon the trion and an outgoing phonon with wavenumber k . Only two energy levels, $|\uparrow\rangle$ and $|\uparrow\rangle_x$, are included as they are sufficient to describe the scattered phonons and the subsequent decay.

The outline of this section is as follows: the Hamiltonian (4.9) and the wavefunction (4.10) is rewritten to describe the system shown in fig. 6.11. To simplify the equations of motion, the free propagation of the phonons is removed by changing to an appropriate rotating frame before solving the Schrödinger equation. Lastly, the fidelity is calculated for a GHZ state quantifying the effect of phonon induced pure dephasing. This fidelity is referred to as the dephasing fidelity.

6.3.1 Hamiltonian and Wavefunction

We go back to the Hamiltonian (4.9) describing a four-level system in an external magnetic field and rewrite it to a two-level system

$$\hat{H}^{two-level} = \hat{H}_0^{two-level} + \hat{H}_{Zeeman}^{two-level} + \hat{H}_{field}^{two-level} + \hat{H}_{int}^{two-level}, \quad (6.47)$$

where

$$\hat{H}_0^{two-level} = \omega_0 |\uparrow\rangle \langle \uparrow| \quad (6.48)$$

$$\hat{H}_{Zeeman}^{two-level} = \frac{\delta g}{2} |\uparrow\rangle \langle \uparrow| \quad (6.49)$$

$$\hat{H}_{field}^{two-level} = iv_g \int dz \frac{\partial \hat{a}^\dagger(z)}{\partial t} \hat{a}(z) \quad (6.50)$$

$$\hat{H}_{int}^{two-level} = g \int dz \delta(z) (e^{-ik_0 z} |\uparrow\rangle \langle \uparrow| \hat{a}^\dagger(z) + e^{ik_0 z} |\uparrow\rangle \langle \uparrow| \hat{a}(z)) \quad (6.51)$$

$$\hat{H}_{phonon} = \sum_{k'} \omega_{k'} \hat{b}_{k'}^\dagger \hat{b}_{k'} + \sum_{k,k'} g_{kk'} \hat{b}_k^\dagger \hat{b}_{k'} |\uparrow\rangle \langle \uparrow|. \quad (6.52)$$

Furthermore we add to (6.47) a term containing the phonon bath and a term containing the trion-phonon interaction. The total Hamiltonian is then

$$\hat{H} = \hat{H}^{two-level} + \hat{H}_{phonon}, \quad (6.53)$$

where

$$\hat{H}_{phonon} = \sum_{k'} \omega_{k'} \hat{b}_{k'}^\dagger \hat{b}_{k'} + \sum_{k,k'} g_{kk'} \hat{b}_k^\dagger \hat{b}_{k'} |\uparrow\rangle \langle \uparrow|. \quad (6.54)$$

The ladder operator \hat{b}_k (\hat{b}_k^\dagger) annihilates (creates) a phonon with wavevector k . The first term in \hat{H}_{phonon} is the energy of the phonon bath, where ω_k is the energy of phonon with wavenumber k and the second term is the phonon coupling to the trion state, where $g_{kk'}$ is the coupling constant.

The wavefunction (4.10) must also be rewritten. Assuming the decay rate is sufficiently fast compared to the phonon scattering rate, the probability of having more than one phonon scattering on the exciton is zero. The wave function can then be defined as a superposition of the case where no phonon is scattered and the case where a single phonon is scattered, which gives:

$$\begin{aligned} |\psi(t)\rangle &= c_{\uparrow}(t) e^{-\omega_0 t} |\uparrow, 0, 0\rangle \otimes \{b_{k'}\} + \sum_k c_{\uparrow}^{(k)}(t) e^{-\omega_k t} \hat{b}_k^\dagger |\uparrow, 0, 0\rangle \otimes \{b_{k'}\} \\ &+ \sqrt{v_g} \int dt_e c_{\uparrow}(t, t_e) \hat{a}^\dagger(z_0) |\uparrow, 0, 0\rangle \otimes \{b_{k'}\} \\ &+ \sqrt{v_g} \int dt_e \sum_k c_{\uparrow}^{(k)}(t, t_e) e^{-i\omega_k t} \hat{a}^\dagger(z_0) \hat{b}_k^\dagger |\uparrow, 0, 0\rangle \otimes \{b_{k'}\}. \end{aligned} \quad (6.55)$$

with the short-hand notation $|\uparrow, 0, 0\rangle \equiv |\uparrow\rangle \otimes |0\rangle_{photon} \otimes |0\rangle_{phonon}$, where $|0\rangle_{photon}$ ($|0\rangle_{phonon}$) is the vacuum state of emitted photons (scattered phonons). The absolute square of $c_{\uparrow}(t)$ is the probability that no phonons is scattered upon the trion, $c_{\uparrow}(t, t_e)$ is the probability that no phonon was scattered upon the trion and a photon was emitted at time t_e , $c_{\uparrow}^{(k)}(t)$ is the probability that a single phonon was scattered upon the trion and $c_{\uparrow}^{(k)}(t, t_e)$ is the probability that a single phonon was scattered upon the trion and a photon was emitted at time t_e . Lastly, $\{b_{k'}\}$ is the phonon bath which we shall assume to be in a coherent state and write it as a displaced vacuum state. In appendix D it is argued that the spin bath can indeed be written as a coherent state and the properties of the displacement operator needed in the calculations below are listed. The wavefunction (6.55) becomes

$$\begin{aligned} |\psi(t)\rangle &= c_{\uparrow}(t) e^{-\omega_0 t} |\uparrow, 0, 0\rangle \otimes \sum_{k'} D(\beta_{k'}) \{0\} \\ &+ \sum_k c_{\uparrow}^{(k)}(t) e^{-\omega_k t} \hat{b}_k^\dagger |\uparrow, 0, 0\rangle \otimes \sum_{k'} D(\beta_{k'}) \{0\} \\ &+ \sqrt{v_g} \int dt_e c_{\uparrow}(t, t_e) \hat{a}^\dagger(z_0) |\uparrow, 0, 0\rangle \otimes \sum_{k'} D(\beta_{k'}) \{0\} \\ &+ \sqrt{v_g} \int dt_e \sum_k c_{\uparrow}^{(k)}(t, t_e) e^{-i\omega_k t} \hat{a}^\dagger(z_0) \hat{b}_k^\dagger |\uparrow, 0, 0\rangle \otimes \sum_{k'} D(\beta_{k'}) \{0\}. \end{aligned} \quad (6.56)$$

In the next section, we change to the rotating frame.

6.3.2 Rotating Frame

Transforming (6.56) as

$$|\psi(t)\rangle \rightarrow \sum_{k'} D^\dagger(\beta_{k'}) |\psi(t)\rangle, \quad (6.57)$$

changes to a rotating frame which can be understood as a phononic interaction picture since it removes the free propagation of the phonons. The Schrödinger equation becomes

$$i \sum_{k'} \frac{\partial D^\dagger(\beta_{k'}) |\psi(t)\rangle}{\partial t} = i \sum_{k'} \frac{\partial D^\dagger(\beta_{k'})}{\partial t} |\psi(t)\rangle + i \sum_{k'} D^\dagger(\beta_{k'}) \frac{\partial |\psi(t)\rangle}{\partial t} \quad (6.58)$$

$$= i \sum_{k'} \frac{\partial D^\dagger(\beta_{k'})}{\partial t} |\psi(t)\rangle + \sum_{k'} D^\dagger(\beta_{k'}) \hat{H} |\psi(t)\rangle, \quad (6.59)$$

where \hat{H} is defined as in (6.53). To proceed we define the wavefunction (6.56) with the phonon bath in the vacuum state as

$$\begin{aligned} |\bar{\psi}(t)\rangle &= c_\uparrow(t) e^{-\omega_0 t} |\uparrow, 0, 0\rangle \otimes \{0\} \\ &+ \sum_k c_\uparrow^{(k)}(t) e^{-\omega_k t} \hat{b}_k^\dagger |\uparrow, 0, 0\rangle \otimes \{0\} \\ &+ \sqrt{v_g} \int dt_e c_\uparrow(t, t_e) \hat{a}^\dagger(z_0) |\uparrow, 0, 0\rangle \otimes \{0\} \\ &+ \sqrt{v_g} \int dt_e \sum_k c_\uparrow^{(k)}(t, t_e) e^{-i\omega_k t} \hat{a}^\dagger(z_0) \hat{b}_k^\dagger |\uparrow, 0, 0\rangle \otimes \{0\}. \end{aligned} \quad (6.61)$$

Thus (6.59) can be written as

$$\begin{aligned} i \sum_{k'} \frac{\partial D^\dagger(\beta_{k'})}{\partial t} |\psi(t)\rangle + \sum_{k'} D^\dagger(\beta_{k'}) \hat{H} |\psi(t)\rangle \\ = i \sum_{k'} \frac{\partial D^\dagger(\beta_{k'})}{\partial t} D(\beta_{k'}) |\bar{\psi}(t)\rangle + \sum_{k'} D^\dagger(\beta_{k'}) \hat{H} D(\beta_{k'}) |\bar{\psi}(t)\rangle. \end{aligned} \quad (6.62)$$

Using (6.61) and (6.62), we find

$$i \frac{\partial |\bar{\psi}(t)\rangle}{\partial t} = i \sum_{k'} \frac{\partial D^\dagger(\beta_{k'})}{\partial t} D(\beta_{k'}) |\bar{\psi}(t)\rangle + \sum_{k'} D^\dagger(\beta_{k'}) \hat{H} D(\beta_{k'}) |\bar{\psi}(t)\rangle, \quad (6.63)$$

which is the phononic interaction picture Schrödinger equation which we now proceed to solve starting with the time-derivative of the conjugate transpose of the displacement operator

$$\frac{dD^\dagger(\beta_{k'})}{dt} = \frac{d}{dt} \left(e^{-\beta_{k'}(t)\hat{b}_{k'}^\dagger} e^{\beta_{k'}^*(t)\hat{b}_{k'}} e^{-\frac{1}{2}|\beta_{k'}|^2} \right) \quad (6.64)$$

$$= \frac{\partial e^{-\beta_{k'}(t)\hat{b}_{k'}^\dagger}}{\partial t} e^{\beta_{k'}^*(t)\hat{b}_{k'}} e^{-\frac{1}{2}|\beta_{k'}|^2} + e^{-\beta_{k'}(t)\hat{b}_{k'}^\dagger} \frac{\partial e^{\beta_{k'}^*(t)\hat{b}_{k'}}}{\partial t} e^{-\frac{1}{2}|\beta_{k'}|^2} \quad (6.65)$$

$$= -\dot{\beta}_{k'}(t)\hat{b}_{k'}^\dagger e^{-\beta_{k'}(t)\hat{b}_{k'}^\dagger} e^{\beta_{k'}^*(t)\hat{b}_{k'}} e^{-\frac{1}{2}|\beta_{k'}|^2} \\ + e^{-\beta_{k'}(t)\hat{b}_{k'}^\dagger} \dot{\beta}_{k'}^*(t)\hat{b}_{k'} e^{\beta_{k'}^*(t)\hat{b}_{k'}} e^{-\frac{1}{2}|\beta_{k'}|^2} \quad (6.66)$$

$$= -\dot{\beta}_{k'}(t)\hat{b}_{k'}^\dagger D^\dagger(\beta_{k'}) + e^{-\beta_{k'}(t)\hat{b}_{k'}^\dagger} \dot{\beta}_{k'}^*(t)\hat{b}_{k'} e^{\beta_{k'}(t)\hat{b}_{k'}^\dagger} \\ e^{-\beta_{k'}(t)\hat{b}_{k'}^\dagger} e^{\beta_{k'}^*(t)\hat{b}_{k'}} e^{-\frac{1}{2}|\beta_{k'}|^2} \quad (6.67)$$

$$= -\dot{\beta}_{k'}(t)\hat{b}_{k'}^\dagger D^\dagger(\beta_{k'}) + \dot{\beta}_{k'}^*(t) e^{-\beta_{k'}(t)\hat{b}_{k'}^\dagger} \hat{b}_{k'} e^{\beta_{k'}(t)\hat{b}_{k'}^\dagger} D^\dagger(\beta_{k'}) \quad (6.68)$$

$$= \left(-\dot{\beta}_{k'}(t)\hat{b}_{k'}^\dagger + \dot{\beta}_{k'}^*(t) e^{-\beta_{k'}(t)\hat{b}_{k'}^\dagger} \hat{b}_{k'} e^{\beta_{k'}(t)\hat{b}_{k'}^\dagger} \right) D^\dagger(\beta_{k'}) \quad (6.69)$$

$$= \left(-\dot{\beta}_{k'}(t)\hat{b}_{k'}^\dagger + \dot{\beta}_{k'}^*(t)(\hat{b}_{k'} + \beta_{k'}(t)) \right) D^\dagger(\beta_{k'}) \quad (6.70)$$

$$= \left(-\dot{\beta}_{k'}(t)\hat{b}_{k'}^\dagger + \dot{\beta}_{k'}^*(t)\hat{b}_{k'} + \dot{\beta}_{k'}^*(t)\beta_{k'}(t) \right) D^\dagger(\beta_{k'}) \quad (6.71)$$

$$= \left(i\omega_{k'}\beta_{k'}(t)\hat{b}_{k'}^\dagger + i\omega_{k'}\dot{\beta}_{k'}^*(t)\hat{b}_{k'} + i\omega_{k'}|\beta_{k'}|^2 \right) D^\dagger(\beta_{k'}). \quad (6.72)$$

where (D.5) is applied in (6.66) and the first term in (6.67) and (D.6) is applied in (6.70). Inserting (6.72) into the photonic interaction Hamiltonian Schrödinger equation (6.63) yields

$$i \frac{\partial |\bar{\psi}(t)\rangle}{\partial t} = - \sum_{k'} \left(\omega_{k'}\beta_{k'}(t)\hat{b}_{k'}^\dagger + \omega_{k'}\dot{\beta}_{k'}^*(t)\hat{b}_{k'} + \omega_{k'}|\beta_{k'}|^2 \right) |\bar{\psi}(t)\rangle \\ + \sum_{k'} D^\dagger(\beta_{k'}) \hat{H} D(\beta_{k'}) |\bar{\psi}(t)\rangle. \quad (6.73)$$

Before evaluating the second term on the right hand side of (6.73), we note that the only part of \hat{H} which is affected by the displacement operator is \hat{H}_{phonon} , since it is

the only part with non-commuting operators. Therefore, it is sufficient to evaluate

$$D^\dagger(\beta_{k'})\hat{H}_{phonon}D(\beta_{k'}) = \sum_{k,k'} D^\dagger(\beta_{k'}) (\omega_{k'}\hat{b}_{k'}^\dagger\hat{b}_{k'} + g_{kk'}\hat{b}_k^\dagger\hat{b}_{k'} |\uparrow\rangle \langle\uparrow|) D(\beta_{k'}) \quad (6.74)$$

$$= \sum_{k,k'} \omega_{k'} D^\dagger(\beta_{k'}) \hat{b}_{k'}^\dagger \hat{b}_{k'} D(\beta_{k'}) + g_{kk'} D^\dagger(\beta_{k'}) \hat{b}_k^\dagger \hat{b}_{k'} D(\beta_{k'}) |\uparrow\rangle \langle\uparrow| \quad (6.75)$$

$$= \sum_{k,k'} \omega_{k'} D^\dagger(\beta_{k'}) \hat{b}_{k'}^\dagger D(\beta_{k'}) (\hat{b}_{k'} + \beta_{k'}(t)) + g_{kk'} D^\dagger(\beta_{k'}) \hat{b}_k^\dagger D(\beta_{k'}) (\hat{b}_{k'} + \beta_{k'}(t)) |\uparrow\rangle \langle\uparrow| \quad (6.76)$$

$$= \sum_{k,k'} \omega_{k'} (\hat{b}_{k'}^\dagger + \beta_{k'}^*(t)) (\hat{b}_{k'} + \beta_{k'}(t)) + g_{kk'} (\hat{b}_k^\dagger + \beta_{k'}^*(t)) (\hat{b}_{k'} + \beta_{k'}(t)) |\uparrow\rangle \langle\uparrow| \quad (6.77)$$

$$= \sum_{k,k'} \omega_{k'} (\hat{b}_{k'}^\dagger \hat{b}_{k'} + \hat{b}_{k'}^\dagger \beta_{k'}(t) + \beta_{k'}^*(t) \hat{b}_{k'} + |\beta_{k'}|^2) + g_{kk'} (\hat{b}_k^\dagger \hat{b}_{k'} + \hat{b}_k^\dagger \beta_{k'}(t) + \beta_{k'}^*(t) \hat{b}_{k'} + |\beta_{k'}|^2) |\uparrow\rangle \langle\uparrow|. \quad (6.78)$$

In (6.76) and (6.77) we have used (D.6).

Inserting the expression derived in (6.78) into (6.73) yields

$$i \frac{\partial |\bar{\psi}(t)\rangle}{\partial t} = - \sum_{k'} (\omega_{k'} \beta_{k'}(t) \hat{b}_{k'}^\dagger + \omega_{k'} \beta_{k'}^*(t) \hat{b}_{k'} + \omega_{k'} |\beta_{k'}|^2) |\bar{\psi}(t)\rangle + (\hat{H}_0 + \hat{H}_{Zeeman} + \hat{H}_{Photon}) \sum_{k'} D^\dagger(\beta_{k'}) \hat{H}_{phonon} D(\beta_{k'}) |\bar{\psi}(t)\rangle \quad (6.79)$$

$$= - \sum_{k'} (\omega_{k'} \beta_{k'}(t) \hat{b}_{k'}^\dagger + \omega_{k'} \beta_{k'}^*(t) \hat{b}_{k'} + \omega_{k'} |\beta_{k'}|^2) |\bar{\psi}(t)\rangle + (\hat{H}_0 + \hat{H}_{Zeeman} + \hat{H}_{Photon}) |\bar{\psi}(t)\rangle + \sum_{k'} \omega_{k'} (\hat{b}_{k'}^\dagger \hat{b}_{k'} + \hat{b}_{k'}^\dagger \beta_{k'}(t) + \beta_{k'}^*(t) \hat{b}_{k'} + |\beta_{k'}|^2) |\bar{\psi}(t)\rangle \quad (6.80)$$

$$+ \sum_{k,k'} g_{kk'} (\hat{b}_k^\dagger \hat{b}_{k'} + \hat{b}_k^\dagger \beta_{k'}(t) + \beta_{k'}^*(t) \hat{b}_{k'} + |\beta_{k'}|^2) |\uparrow\rangle \langle\uparrow| |\bar{\psi}(t)\rangle = (\hat{H}_0 + \hat{H}_{Zeeman} + \hat{H}_{Photon}) |\bar{\psi}(t)\rangle + \sum_{k'} \omega_{k'} \hat{b}_{k'}^\dagger \hat{b}_{k'} |\bar{\psi}(t)\rangle + \sum_{k,k'} g_{kk'} (\hat{b}_k^\dagger \hat{b}_{k'} + \hat{b}_k^\dagger \beta_{k'}(t) + \beta_{k'}^*(t) \hat{b}_{k'} + |\beta_{k'}|^2) |\uparrow\rangle \langle\uparrow| |\bar{\psi}(t)\rangle. \quad (6.81)$$

The first three terms in (6.81) contain no information about the phonon induced pure dephasing: \hat{H}_0 couples the excited states ($c_{\uparrow}(t)$ and $c_{\uparrow}^{(k)}(t)$) to themselves, \hat{H}_{Zeeman} couples the ground states ($c_{\uparrow}(t, t_e)$ and $c_{\uparrow}^{(k)}(t, t_e)$) to themselves and \hat{H}_{Photon} couples $c_{\uparrow}(t)$ to $c_{\uparrow}(t, t_e)$ and $c_{\uparrow}^{(k)}(t)$ to $c_{\uparrow}^{(k)}(t, t_e)$ via absorption and emission of a photon. The calculations necessary to evaluate these three terms are similar to those performed in section 4.3 and will, for this reason, not be shown explicitly.

The remaining terms will however be calculated explicitly:

$$\begin{aligned}
& \sum_{k'} \omega_{k'} \hat{b}_{k'}^\dagger \hat{b}_{k'} |\bar{\psi}(t)\rangle + \sum_{k,k'} g_{kk'} (\hat{b}_k^\dagger \hat{b}_{k'} + \hat{b}_k^\dagger \beta_{k'}(t) + \beta_{k'}^*(t) \hat{b}_{k'} + |\beta_{k'}|^2) |\uparrow\rangle \langle \uparrow | |\bar{\psi}(t)\rangle \\
&= \left(\sum_{k'} \omega_{k'} \hat{b}_{k'}^\dagger \hat{b}_{k'} + \sum_{k,k'} g_{kk'} (\hat{b}_k^\dagger \hat{b}_{k'} + \hat{b}_k^\dagger \beta_{k'}(t) + \beta_{k'}^*(t) \hat{b}_{k'} + |\beta_{k'}|^2) |\uparrow\rangle \langle \uparrow | \right) \\
& \quad (c_{\uparrow}(t) e^{-\omega_0 t} |\uparrow, 0, 0\rangle + \sum_k c_{\uparrow}^{(k)}(t) e^{-\omega_k t} \hat{b}_k^\dagger |\uparrow, 0, 0\rangle \\
& \quad + \sqrt{v_g} \int dt_e c_{\uparrow}(t, t_e) \hat{a}^\dagger(z_0) |\uparrow, 0, 0\rangle \tag{6.82} \\
& \quad + \sqrt{v_g} \int dt_e \sum_k c_{\uparrow}^{(k)}(t, t_e) e^{-i\omega_k t} \hat{a}^\dagger(z_0) \hat{b}_k^\dagger |\uparrow, 0, 0\rangle) \\
&= c_{\uparrow}(t) e^{-i\omega_0 t} \sum_{k,k'} g_{kk'} \beta_{k'}(t) |\uparrow, 0, 0\rangle + \sum_k \omega_k c_{\uparrow}^k(t) e^{-i\omega_k t} \hat{b}_k^\dagger |\uparrow, 0, 0\rangle \\
& \quad + \sum_{k,k'} g_{kk'} c_{\uparrow}^k(t) e^{-i\omega_k t} \beta_{k'}^*(t) \hat{b}_k^\dagger |\uparrow, 0, 0\rangle \tag{6.83} \\
& \quad + \sqrt{v_g} \int dt_e \sum_k \omega_k c_{\uparrow}^{(k)}(t, t_e) e^{-i\omega_k t} \hat{a}^\dagger(z_0) \hat{b}_k^\dagger |\uparrow, 0, 0\rangle.
\end{aligned}$$

By inserting the expression in (6.83) back into (6.81), the Schrödinger equation yields

$$\begin{aligned}
i \frac{\partial |\bar{\psi}(t)\rangle}{\partial t} &= (\hat{H}_0 + \hat{H}_{Zeeman} + \hat{H}_{Photon}) |\bar{\psi}(t)\rangle \\
& \quad + c_{\uparrow}(t) e^{-i\omega_0 t} \sum_{k,k'} g_{kk'} \beta_{k'}(t) |\uparrow, 0, 0\rangle \\
& \quad + \sum_k \omega_k c_{\uparrow}^k(t) e^{-i\omega_k t} \hat{b}_k^\dagger |\uparrow, 0, 0\rangle \tag{6.84} \\
& \quad + \sum_{k,k'} g_{kk'} c_{\uparrow}^k(t) e^{-i\omega_k t} \beta_{k'}^*(t) \hat{b}_k^\dagger |\uparrow, 0, 0\rangle \\
& \quad + \sqrt{v_g} \int dt_e \sum_k \omega_k c_{\uparrow}^{(k)}(t, t_e) e^{-i\omega_k t} \hat{a}^\dagger(z_0) \hat{b}_k^\dagger |\uparrow, 0, 0\rangle.
\end{aligned}$$

We can now obtain four coupled differential equations by multiplying (6.84) with $\langle \uparrow, 0, 0 |$, $\langle \uparrow, 0, 0 | \hat{b}_k$, $\langle \uparrow, 0, 0 | \hat{a}(z)$ and $\langle \uparrow, 0, 0 | \hat{a}(z) \hat{b}_k$, respectively

$$\dot{c}_{\uparrow}(t) = -i \frac{g}{\sqrt{v_g}} c_{\uparrow}(t, t_e) - i \sum_{k,k'} g_{kk'} c_{\uparrow}^{(k)}(t) e^{-i(\omega_k - \omega_0)t} \beta_{k'}^*(t) \tag{6.85}$$

$$\sum_k \dot{c}_{\uparrow}^{(k)}(t) = -i \frac{g}{\sqrt{v_g}} \sum_k c_{\uparrow}^{(k)}(t, t_e) - i \sum_{k,k'} g_{kk'} c_{\uparrow}(t) e^{i(\omega_k - \omega_0)t} \beta_{k'}(t) \tag{6.86}$$

$$\dot{c}_{\uparrow}(t, t_e) = -i \frac{\delta g}{2} c_{\uparrow}(t, t_e) - i \frac{g}{\sqrt{v_g}} \delta(t - t_e) c_{\uparrow}(t) \tag{6.87}$$

$$\sum_k \dot{c}_{\uparrow}^{(k)}(t, t_e) = -i \frac{\delta g}{2} \sum_k c_{\uparrow}^{(k)}(t, t_e) - i \frac{g}{\sqrt{v_g}} \delta(t - t_e) \sum_k c_{\uparrow}^{(k)}(t). \tag{6.88}$$

Imposing the boundary conditions $c_{\uparrow}(t = 0) = 1$ and $c_{\uparrow}^{(k)}(t = 0) = c_{\uparrow}(t = 0, t_e) = c_{\uparrow}^{(k)}(t = 0, t_e) = 0$, integrating (6.86) and (6.87) and inserting $c_{\uparrow}(t, t_e)$ and $c_{\uparrow}^{(k)}(t)$ into

(6.85) yields

$$\dot{c}_{\uparrow}(t) = -\frac{g^2}{v_g}c_{\uparrow}(t) - \sum_{k,k',k''} g_{kk'}g_{kk''}\beta_{k''}(t)e^{-i\omega_k t} \int_0^t dt' c_{\uparrow}(t')\beta_{k'}(t')e^{i\omega_k t'}. \quad (6.89)$$

Averaging over the displacement coefficients in (6.89) sets $k' = k''$, and (6.89) becomes

$$\dot{\bar{c}}_{\uparrow}(t) = -\frac{g^2}{v_g}c_{\uparrow}(t) - \sum_{k,k'} |g_{kk'}|^2 |\bar{\beta}_{k'}|^2 \int_0^t dt' c_{\uparrow}(t')e^{-i(\omega_k - \omega_{k'})(t-t')}. \quad (6.90)$$

To proceed, we perform the Weisskopf-Wigner approximation: assuming $c_{\uparrow}(t')$ varies little in the time interval $t \sim t'$, where the integral has a non-zero value, we may replace $c_{\uparrow}(t')$ with $c_{\uparrow}(t)$. This approximation can be recognised as Markovian, since it effectively states that the dynamics of $c_{\uparrow}(t)$ is independent of time $t > t'$, i.e. the system has no memory of the past. Applying the Weisskopf-Wigner approximation to (6.90) yields

$$\dot{\bar{c}}_{\uparrow}(t) = -\frac{g^2}{v_g}c_{\uparrow}(t) - \sum_{k,k'} |g_{kk'}|^2 |\bar{\beta}_{k'}|^2 c_{\uparrow}(t) \int_0^t dt' e^{-i(\omega_k - \omega_{k'})(t-t')} \quad (6.91)$$

$$= -\frac{g^2}{v_g}c_{\uparrow}(t) - \sum_{k,k'} |g_{kk'}|^2 |\bar{\beta}_{k'}|^2 c_{\uparrow}(t) \pi \delta(\omega_k - \omega_{k'}), \quad (6.92)$$

where the Cauchy principal part has been omitted in (6.92). The solution to (6.92) is

$$\bar{c}_{\uparrow}(t) = e^{-\frac{\gamma}{2}t - \gamma_d t}, \quad (6.93)$$

where $\gamma \equiv \frac{g^2}{2v_g}$ and $\gamma_d \equiv \pi \sum_{k,k'} |g_{kk'}|^2 |\bar{\beta}_{k'}|^2 \delta(\omega_k - \omega_{k'})$.

From (6.86), the coefficient $c_{\uparrow}^{(k)}(t)$ is seen to be

$$c_{\uparrow}^{(k)}(t) = -ie^{-\frac{\gamma}{2}t - i\omega_0 t} \sum_{k'} g_{kk'} \int_0^t dt' \beta_{k'}(t')e^{i\omega_k t'} \quad (6.94)$$

To solve (6.94), we take the absolute square, average and include the sum of k , obtaining

$$\sum_k |\bar{c}_{\uparrow}^{(k)}(t)|^2 = \sum_{k,k'} |g_{kk'}|^2 |\bar{\beta}_{k'}|^2 e^{-\gamma t} \int_0^t dt' \int_0^t dt'' e^{i(\omega_k + i\omega_{k'})(t' - t'') - \gamma_d(t' + t'')}. \quad (6.95)$$

Defining the new parameters $\tau = t - t''$ and $s = t' + t''$ allows us to perform integration by substitution in (6.95)

$$\sum_k |\bar{c}_{\uparrow}^{(k)}(t)|^2 = \frac{1}{2} \sum_{k,k'} |g_{kk'}|^2 |\bar{\beta}_{k'}|^2 e^{-\gamma t} \int_0^{2t} d\tau \int_{-\infty}^{\infty} ds e^{i(\omega_k + i\omega_{k'})\tau - \gamma_d s} \quad (6.96)$$

$$= \sum_{k,k'} |g_{kk'}|^2 |\bar{\beta}_{k'}|^2 e^{-\gamma t} \pi \delta(\omega_k - \omega_{k'}) \int_0^{2t} d\tau e^{-\gamma_d s} \quad (6.97)$$

$$= \pi \sum_{k,k'} |g_{kk'}|^2 |\bar{\beta}_{k'}|^2 e^{-\gamma t} \delta(\omega_k - \omega_{k'}) \frac{1}{\gamma_d} (1 - e^{-2\gamma_d t}) \quad (6.98)$$

$$= e^{-\gamma t} (1 - e^{-2\gamma_d t}). \quad (6.99)$$

Note that the coefficients (6.92) and (6.99) for the two excited states satisfy

$$|\bar{c}_{\uparrow}(t)|^2 + \sum_k |\bar{c}_{\uparrow}^{(k)}(t)|^2 = e^{-\gamma t - 2\gamma_d t} + e^{-\gamma t} (1 - e^{-2\gamma_d t}) \quad (6.100)$$

$$= e^{-\gamma t} \quad (6.101)$$

as expected.

The two ground state coefficients can be determined using a Laplace transformation, for which the calculation is similar to the one performed in section 4.3, yielding

$$\bar{c}_{\uparrow}(t, t_e) = \sqrt{\gamma} e^{-i\frac{\delta g}{2}(t-t_e) - \frac{\gamma}{2} t_e - \gamma_d t_e} \theta(t - t_e) \quad (6.102)$$

$$\sum_k |\bar{c}_{\uparrow}^{(k)}(t, t_e)|^2 = \gamma e^{-\gamma t_e} (1 - e^{-2\gamma_d t_e}) \theta(t - t_e). \quad (6.103)$$

In the next section, we define the ideal state and output state from the coefficients (6.102) and (6.103) and in section 6.3.4 we calculate the dephasing fidelity using these states.

6.3.3 Ideal State and Output State

Ideally, the probability of a phonon scattering upon the trion is zero, corresponding to evaluating (6.102) at $\gamma_d = 0$, which gives

$$\bar{c}_{\downarrow}(t, t_e) \Big|_{\gamma_d=0} = \sqrt{\gamma} e^{-i\frac{\delta g}{2}(t-t_e) - \frac{\gamma}{2} t_e} \theta(t - t_e) \quad (6.104)$$

The ideal GHZ state can now be defined by inserting the coefficient in (6.104) into the wavefunction (6.55) and generalising to $N/2$ photons. The ideal GHZ state is:

$$|\psi_{ideal, GHZ}^{dephasing}\rangle = \frac{1}{\sqrt{2}} \left(\prod_{j'=1,3}^{N-1} \bar{c}_{\uparrow}(t, t_{e,j'}) \Big|_{\gamma_d=0} |\downarrow, e', 0\rangle^{\otimes N/2} + \prod_{i'=2,4}^N \bar{c}_{\uparrow}(t, t_{e,i'}) \Big|_{\gamma_d=0} |\uparrow, l', 0\rangle^{\otimes N/2} \right), \quad (6.105)$$

where the prime symbols are included such that the photon states in (6.105) can be distinguished from the photon states in the output state defined below. In the output

state, the probability of a photon to scatter and not scatter are both included and the GHZ output state is defined from (6.102), (6.103) and (6.55) as

$$\begin{aligned}
|\psi_{output,GHZ}^{dephasing}\rangle &= \frac{1}{2} \prod_{j=1,3}^{N-1} (\bar{c}_{\downarrow}(t, t_{e,j}) |\downarrow, e, 0\rangle^{\otimes N/2} \\
&\quad + \sum_k \bar{c}_{\downarrow}^{(k)}(t, t_{e,j}) |\downarrow, e, 1_k\rangle^{\otimes N/2}) \\
&\quad + \frac{1}{2} \prod_{i=2,4}^N (\bar{c}_{\uparrow}(t, t_{e,i}) |\uparrow, l, 0\rangle^{\otimes N/2} \\
&\quad + \sum_k \bar{c}_{\uparrow}^{(k)}(t, t_{e,i}) |\downarrow, l, 1_k\rangle^{\otimes N/2})
\end{aligned} \tag{6.106}$$

6.3.4 Dephasing Fidelity

Before calculating the fidelity, we perform a partial trace of the output density matrix to remove the phononic subsystem, since the phonons are not measured. The output density matrix is

$$\hat{\rho}_{output} = |\psi_{output,GHZ}^{dephasing}\rangle \langle \psi_{output,GHZ}^{dephasing}| \tag{6.107}$$

The reduced output density matrix, where the phononic subsystem is removed, is

$$\hat{\rho}'_{output} = \text{Tr}_{phonon} [\hat{\rho}_{output}] \tag{6.108}$$

$$= \langle 0 | \hat{\rho}_{output} | 0 \rangle + \sum_k \langle 1_k | \hat{\rho}_{output} | 1_k \rangle \tag{6.109}$$

$$\begin{aligned}
&= \frac{1}{4} (|\downarrow, e\rangle^{\otimes N/2} \langle e, \downarrow|^{\otimes N/2} \prod_{j=1,3}^{N-1} (|\bar{c}_{\downarrow}(t, t_{e,j})|^2 + \sum_k |\bar{c}_{\downarrow}^{(k)}(t, t_{e,j})|^2) \\
&\quad + |\uparrow, l\rangle^{\otimes N/2} \langle l, \uparrow|^{\otimes N/2} \prod_{i=2,4}^N (|\bar{c}_{\uparrow}(t, t_{e,i})|^2 + \sum_k |\bar{c}_{\uparrow}^{(k)}(t, t_{e,i})|^2) \\
&\quad + |\uparrow, l\rangle^{\otimes N/2} \langle e, \downarrow|^{\otimes N/2} \prod_{i=2,4}^N \prod_{j=1,3}^{N-1} \bar{c}_{\uparrow}(t, t_{e,i}) \bar{c}_{\downarrow}^*(t, t_{e,j}) \\
&\quad + |e, \downarrow\rangle^{\otimes N/2} \langle \uparrow, l|^{\otimes N/2} \prod_{i=2,4}^N \prod_{j=1,3}^{N-1} \bar{c}_{\downarrow}(t, t_{e,j}) \bar{c}_{\uparrow}^*(t, t_{e,i}) \\
&\quad + |\uparrow, l\rangle^{\otimes N/2} \langle e, \downarrow|^{\otimes N/2} \prod_{i=2,4}^N \prod_{j=1,3}^{N-1} \sum_k \bar{c}_{\uparrow}^{(k)}(t, t_{e,i}) \bar{c}_{\downarrow}^{*(k)}(t, t_{e,j}) \\
&\quad + |e, \downarrow\rangle^{\otimes N/2} \langle \uparrow, l|^{\otimes N/2} \prod_{i=2,4}^N \prod_{j=1,3}^{N-1} \sum_k \bar{c}_{\downarrow}^{(k)}(t, t_{e,j}) \bar{c}_{\uparrow}^{*(k)}(t, t_{e,i}),
\end{aligned} \tag{6.110}$$

where the last two terms in (6.110) are removed by the Markov approximation. The fidelity is from (6.105) and (6.110) defined as

$$F_{dephasing} = \langle \psi_{ideal,GHZ}^{dephasing} | \hat{\rho}_{output}^{dephasing} | \psi_{ideal,GHZ}^{dephasing} \rangle \quad (6.111)$$

$$= \frac{1}{8} \left((| \langle e|e' \rangle |^2)^{\otimes N/2} \prod_{\substack{j=1,3 \\ j'=1,3}}^{N-1} |\bar{c}_{\downarrow}(t, t_{e,j})|^2 |\bar{c}_{\downarrow}(t, t_{e,j'})|^2 \right) \Big|_{\gamma_d=0} \quad (6.112)$$

$$+ (| \langle e|e' \rangle |^2)^{\otimes N/2} \prod_{\substack{j=1,3 \\ j'=1,3}}^{N-1} \sum_k |\bar{c}_{\downarrow}^{(k)}(t, t_{e,j})|^2 |\bar{c}_{\downarrow}(t, t_{e,j'})|^2 \Big|_{\gamma_d=0} \\ + (| \langle l|l' \rangle |^2)^{\otimes N/2} \prod_{\substack{i=2,4 \\ i'=2,4}}^N |\bar{c}_{\uparrow}(t, t_{e,i})|^2 |\bar{c}_{\uparrow}(t, t_{e,i'})|^2 \Big|_{\gamma_d=0} \quad (6.113)$$

$$+ (| \langle l|l' \rangle |^2)^{\otimes N/2} \prod_{\substack{i=2,4 \\ i'=2,4}}^N \sum_k |\bar{c}_{\uparrow}^{(k)}(t, t_{e,i})|^2 |\bar{c}_{\uparrow}(t, t_{e,i'})|^2 \Big|_{\gamma_d=0} \\ + (\langle l|l \rangle \langle e|e' \rangle)^{\otimes N/2} \prod_{\substack{i=2,4 \\ i'=2,4}}^N \prod_{\substack{j=1,3 \\ j'=1,3}}^{N-1} \bar{c}_{\uparrow}(t, t_{e,i}) \bar{c}_{\downarrow}^*(t, t_{e,j}) (\bar{c}_{\uparrow}^*(t, t_{e,i'}) \bar{c}_{\uparrow}(t, t_{e,j'})) \Big|_{\gamma_d=0} \\ + (\langle e|e \rangle \langle l|l' \rangle)^{\otimes N/2} \prod_{\substack{i=2,4 \\ i'=2,4}}^N \prod_{\substack{j=1,3 \\ j'=1,3}}^{N-1} \bar{c}_{\uparrow}^*(t, t_{e,i}) \bar{c}_{\downarrow}(t, t_{e,j}) (\bar{c}_{\uparrow}(t, t_{e,i'}) \bar{c}_{\uparrow}^*(t, t_{e,j'})) \Big|_{\gamma_d=0}.$$

Solving (6.113) is simply a matter of integrating exponential functions. Plugging (6.92),(6.99),(6.102),(6.103) and (6.104) into (6.113) and performing the integrals yields $F_{dephasing}$ and the result of this section:

$$F_{dephasing} = \frac{1}{2} + \frac{1}{2} \left(\frac{\gamma}{\gamma + 2\gamma_d} \right)^N. \quad (6.114)$$

As a final remark, a typical value of the dephasing rate γ_d is introduced. The dephasing rate depends on the temperate of the system and the dimensionality of the structure surrounding the quantum dot. For a 1 dimensional waveguide at 5 K, a parameter value of $2\gamma_d \approx 0.12 \text{ ns}^{-1}$ is realistic [48].

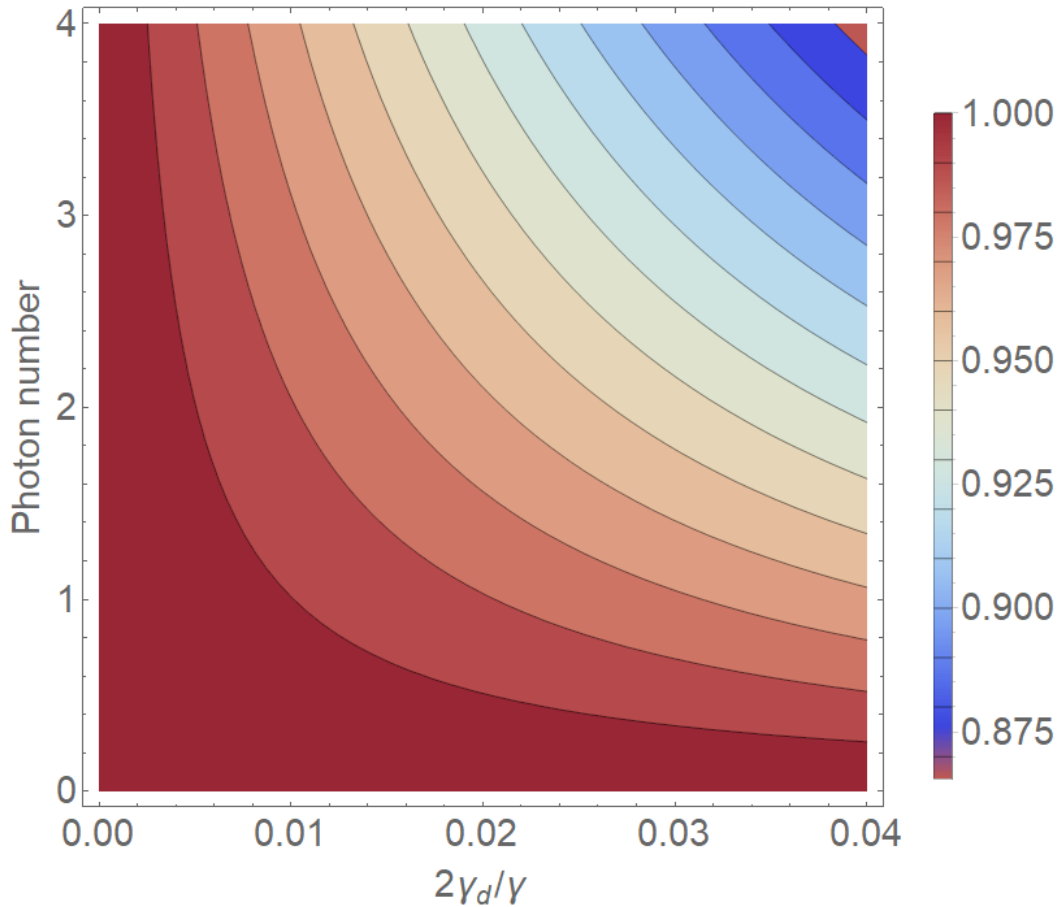


FIGURE 6.12: Each contour line corresponds to a change in the dephasing fidelity $F_{dephasing}$ of 0.01.

Purcell enhancing to $\gamma = 5.7 \text{ ns}^{-1}$ and assuming a dephasing rate of $2\gamma_d = 0.12 \text{ ns}^{-1}$ yields $2\gamma_d/\gamma \approx 0.02$. Fig. 6.12 shows that these parameter values achieve a dephasing fidelity of $F_{dephasing} \approx 0.98$ for a Bell state. A 4 photon GHZ state with similar parameter values achieves a dephasing fidelity of $F_{dephasing} \approx 0.92$. It is seen in fig. 6.12 that further Purcell enhancement will be beneficial, since an increased value of γ leads to an increased dephasing fidelity.

6.4 Combined Fidelity

To conclude the discussion of imperfections in the time-bin spin-photon entanglement protocol, the combined fidelity is defined as:

$$F_{combined}^{GHZ} = \bar{F}_{visibility} F_{decay} F_{dephasing}. \quad (6.115)$$

The value of the combined fidelity as a function of the number of photons is shown in fig. 6.13. The parameter values applied in fig. 6.13 are shown in table 6.1.

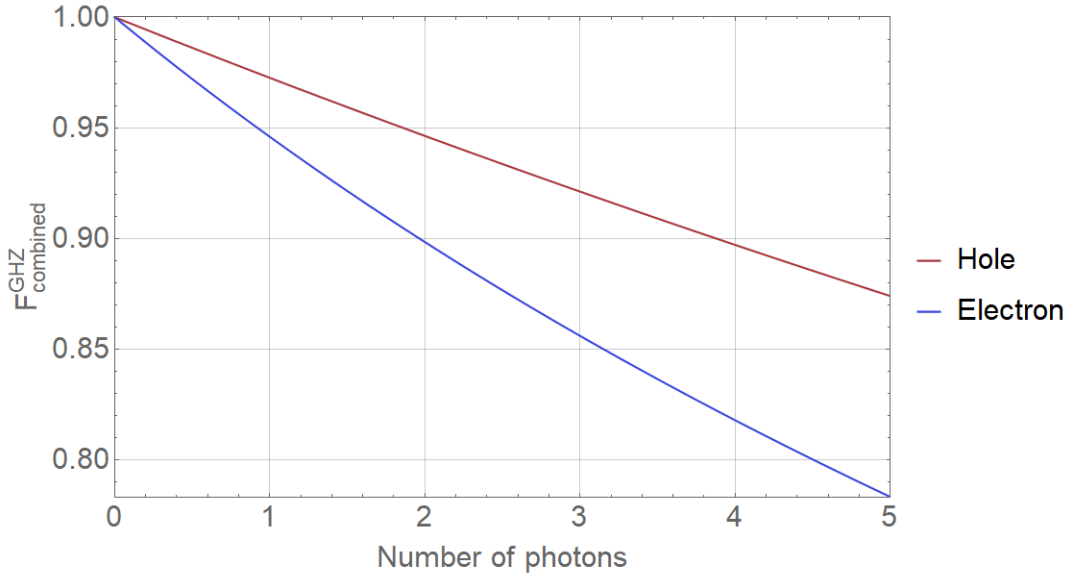


FIGURE 6.13: The combined fidelity defined as in (6.115) for a hole and an electron with the realistic parameters values shown in 6.1.

The hole is in fig. 6.13 seen to be superior to the electron when aiming at achieving a high combined fidelity. This is due to the long coherence time T_2^* of the hole compared to the electron. In the case of a hole, a combined fidelity of $F_{combined}^{GHZ} \approx 0.97$ is achieved for a Bell state and $F_{combined}^{GHZ} \approx 0.9$ for a 4 photon GHZ state. In the case of an electron, a combined fidelity of $F_{combined}^{GHZ} \approx 0.95$ is achieved for a Bell state and $F_{combined}^{GHZ} \approx 0.82$ for a 4 photon GHZ state.

	γ [ns^{-1}]	$2\gamma_d$ [ns^{-1}]	T_2^* [ns]	β_{fs}	$\beta_{\perp,QD}/\beta_{\parallel,QD}$	η_{\perp}	η_{\parallel}
Electron:	5.7	0.12	2.0	0.02	0.05	0.001	0.05
Hole:	5.7	0.12	20.2	0.02	0.05	0.001	0.05

TABLE 6.1: Realistic parameter values used in fig. 6.13. The only difference between a hole and an electron is the coherence time T_2^* .

As a last remark, the perturbative expansion of $F_{combined}^{GHZ}$ in the limit $F_{combined}^{GHZ} \approx 1$ is shown:

$$F_{combined}^{GHZ} \approx 1 - n \left(2 \frac{\sigma^2}{\gamma^2} + \frac{1}{2} (\beta'_{\perp,QD} + \beta_{\perp,QD} \eta_{\perp} (1 - \eta_{\perp}) + \frac{\beta_{\perp,QD}}{\beta_{\parallel,QD}} (1 + 2\beta'_{\perp,QD} + 2\beta_{\perp,QD} \eta_{\perp} (1 - \eta_{\perp}) + \beta'_{\parallel,QD} + \beta_{\parallel,QD} \eta_{\parallel} (1 - \eta_{\parallel}))) + 2 \frac{\gamma_d}{\gamma} \right), \quad (6.116)$$

where $n = N/2$ is the number of photons in the GHZ state. Ideally, the combined fidelity is $F_{combined}^{GHZ} = 1$ but the creation of each photon subtracts the term in the big parentheses in (6.116). Purcell enhancing reduces the contribution of $\bar{F}_{visibility}$ and $F_{dephasing}$ and lowering the free space coupling and implementing a frequency filter in the experimental setup reduce the contribution from F_{decay} .

Chapter 7

Conclusion and Outlook

The results of this thesis are summarised in the conclusion and the need for further theoretical analysis of the protocols are discussed in the outlook.

7.1 Conclusion

In this thesis, imperfections of two different spin-photon entanglement protocols realised by quantum dots embedded in waveguides have been studied. These imperfections arise from unwanted interactions between the system creating the entangled spin-photon states and the environment and from limited performance of experimental equipment. The first protocol creates frequency entangled spin-photon Bell states and two imperfections were studied: the first imperfection is caused by insufficient separation of the ground states, which can lead to sub-maximal entanglement, and the second imperfection is imperfect visibility caused partly by the nuclear Overhauser field and partly by time-jitter of the photon detector. These two imperfections were quantified by the fidelities F_{state} and $\bar{F}_{visibility}$, respectively. Considering both imperfections, quantified by the combined fidelity $F_{combined} = F_{state}\bar{F}_{visibility}$, an optimisation problem occurred which was examined using the perturbative expansion of the combined fidelity

$$F_{combined} \approx 1 - \frac{(\delta_g \epsilon)^2}{4} - \frac{\gamma^2}{4\delta_g^2} + \frac{\epsilon^2 \gamma^2}{8} - \frac{2\sigma^2}{\gamma^2}, \quad (7.1)$$

with the following values of the external magnetic field and the decay rate optimising the fidelity

$$B_{optimal} = \sqrt{\frac{\gamma}{\epsilon(g\mu_B/\hbar)^2}}, \quad \gamma_{optimal} = \sqrt[3]{\frac{4\sigma^2}{\epsilon}}. \quad (7.2)$$

In table 7.1, the main results of the study of imperfections in the frequency entanglement protocol are summarised. It is found that the system applying a hole instead of an electron is superior when comparing the performance based on the combined fidelity for realistic parameter values.

	ϵ [ns]	T_2^* [ns]	$g_{e/h}$	$\gamma_{optimal}$ [ns ⁻¹]	$B_{optimal}$ [T]	$F_{combined}$
Electron:	0.03	2.0	0.5	4.0	0.26	≈ 0.92
Hole:	0.03	20.2	0.08	0.87	0.76	≈ 0.98

TABLE 7.1: The achieved combined fidelity $F_{combined}$ for the system applying an electron or a hole. Realistic values are used for the time-jitter ϵ , the coherence time T_2^* , and the g factors $g_{e/h}$. Optimal values are used for the decay rate γ and the magnetic field B , which are determined using the expressions in (7.2)

The second protocol creates time-bin entangled spin-photon states for which three imperfections were studied. The first imperfection involves sub-maximal visibility caused by the nuclear Overhauser field. Due to the long coherence time of the hole and utilising Purcell enhancement, it was shown that achieving a close-to-unitary visibility fidelity is possible even for extremely large GHZ states. For an electron, a close-to-unitary visibility fidelity is possible for a Bell state and four photon GHZ state yielding a visibility fidelity of $F_{visibility} \approx 0.97$. The second imperfection involves imperfect branching ratio of the spontaneous decay and photon loss. Assuming a free space coupling of $\beta_{fs} = 0.02$ and a branching ratio of $\beta_{\perp, QD}/\beta_{\parallel, QD} = 0.05$, a decay fidelity of $F_{decay} \approx 0.955$ for a four photon GHZ state was achieved under the condition that all unwanted high energy photons are filtered out. The third imperfection is phonon induced pure dephasing of the trion which was shown to be the most significant imperfection in the time-bin entanglement protocol. Realistic values of decay rate $\gamma = 5.7 \text{ ns}^{-1}$ and dephasing rate $2\gamma_d = 0.12 \text{ ns}^{-1}$ yields a dephasing fidelity of $F_{dephasing} \approx 0.98$ for a Bell state and a dephasing fidelity of $F_{dephasing} \approx 0.92$ of for a 4 photon GHZ state.

The combined effect of the three imperfections was shown in section 6.4. In the case of a hole, a combined fidelity of $F_{combined}^{GHZ} \approx 0.97$ is achieved for a Bell state and $F_{combined}^{GHZ} \approx 0.9$ for a 4 photon GHZ state. The applied parameter values are shown in table 6.1. In the case of an electron, a combined fidelity of $F_{combined}^{GHZ} \approx 0.95$ is achieved for a Bell state and $F_{combined}^{GHZ} \approx 0.82$ for a 4 photon GHZ state with the parameter values likewise shown in table 6.1.

The results in this thesis show that the two studied protocols are promising and likely to perform well if applied in the laboratory to create highly entangled states.

7.2 Outlook

In this section, the need for further theoretical investigation of the imperfections in two protocols is discussed. Two different investigations should be considered: the possible effect of imperfections which are not considered in this thesis and the limitations of the combined fidelities defined in this thesis. An additional imperfection, which should be considered, is the effect of inhomogeneous broadening [49]. The combined fidelities applied in this thesis are defined in (5.50) and (6.115). The fidelities quantifying the effect of imperfections studied in this thesis were calculated separately and simply multiplied to obtain the combined fidelities. This method of obtaining an expression for the combined imperfections is expected to be accurate if the effects of the individual imperfections are small. In cases where the effects of the individual imperfections become increasingly significant, the definitions of the combined fidelity (5.50) and (6.115) can seem naive. In a further study, the possible correlations between the different imperfection effects should be exploited and it should be studied whether several imperfections can be simultaneously evaluated using alternative definitions of the combined fidelity.

Appendix A

Photon basis

A.1 Normalised Orthogonal Photon Basis

We start by explicitly showing that $\phi = -\arccos \langle \omega_+ | \omega_- \rangle$ indeed orthogonalizes the photon basis

$$\langle \theta_+ | \theta_- \rangle = \frac{1}{2}(e^{-i\phi/2} \langle \omega_+ | + e^{i\phi/2} \langle \omega_- |)(e^{i\phi/2} |\omega_+\rangle + e^{-i\phi/2} |\omega_-\rangle) \quad (\text{A.1})$$

$$= \frac{1}{2}(e^{i\phi} \langle \omega_- | \omega_+ \rangle - e^{-i\phi} \langle \omega_+ | \omega_- \rangle). \quad (\text{A.2})$$

It is seen that the two terms in (A.2) becomes identical when $\phi = -\arccos \langle \omega_+ | \omega_- \rangle$, making $|\theta_+\rangle$ and $|\theta_-\rangle$ orthogonal.

To obtain the normalisation coefficients, we calculate

$$\langle \theta_{\pm} | \theta_{\pm} \rangle = \frac{1}{2}(e^{-i\phi/2} \langle \omega_+ | \pm e^{i\phi/2} \langle \omega_- |)(e^{i\phi/2} |\omega_+\rangle \pm e^{-i\phi/2} |\omega_-\rangle) \quad (\text{A.3})$$

$$= 1 \pm \frac{1}{2}(e^{i\phi} \langle \omega_- | \omega_+ \rangle + e^{-i\phi} \langle \omega_+ | \omega_- \rangle) \quad (\text{A.4})$$

$$= 1 \pm |\langle \omega_+ | \omega_- \rangle|, \quad (\text{A.5})$$

where in the last line the orthogonalisation condition $\phi = -\arccos \langle \omega_+ | \omega_- \rangle$ is applied.

Appendix B

Coherence time

The definition of the coherence time T_2^* is derived from the time evolution of the total angular momentum along the x-direction J_x using the Heisenberg equation which in general can be written as

$$\frac{d}{dt}A(t) = i[\hat{H}, A(t)] \quad (\text{B.1})$$

Using the Hamiltonian $\hat{H} = \Delta\delta_g J_z$ and the commutator relations $[J_i, J_j] = i\epsilon_{ijk}J_k$, the time evolution of the in-plane total angular momenta is from the Heisenberg equation derived as

$$\dot{J}_x = -\Delta\delta_g J_y \quad (\text{B.2})$$

$$\dot{J}_y = \Delta\delta_g J_x, \quad (\text{B.3})$$

with the solution of the x-component

$$J_x = J_x(t=0)(\cos(\Delta\delta_g t) - J_z(t=0)\sin\Delta\delta_g t). \quad (\text{B.4})$$

We now average over J_x using the definition of the Overhauser field (5.33). We find

$$\langle J_x \rangle = \frac{1}{\sqrt{2\pi\sigma}} \int_{-\infty}^{\infty} d\Delta\delta_g J_x(t=0)(\cos(\Delta\delta_g t) - J_z(t=0)\sin\Delta\delta_g t) e^{-\frac{\Delta\delta_g^2}{2\sigma^2}} \quad (\text{B.5})$$

$$= \frac{1}{\sqrt{2\pi\sigma}} \langle J_x(t=0) \rangle \sqrt{2\pi\sigma} e^{-\frac{t^2\sigma^2}{2}} \quad (\text{B.6})$$

$$= \langle J_x(t=0) \rangle e^{-\frac{t^2\sigma^2}{2}}. \quad (\text{B.7})$$

It is seen from (B.7) that σ characterises the time evolution of J_x and we define the coherence time as

$$T_2^* \equiv \frac{\sqrt{2}}{\sigma} \quad (\text{B.8})$$

Appendix C

Combined Fidelity

C.1 Validity of the combined fidelity perturbative expansion

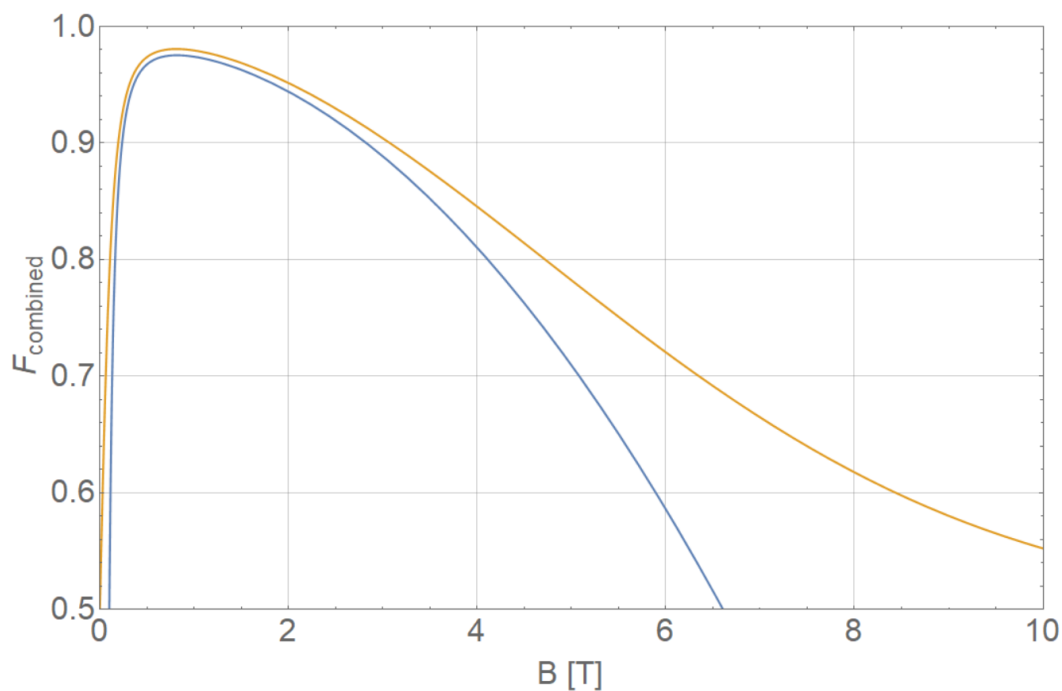


FIGURE C.1: The orange curve is the exact combined fidelity $F_{combined} = F_{state}\bar{F}_{visibility}$ and the blue curve is the perturbative expansion of the combined fidelity 5.62. Chosen values are $\sigma = 0.07 \text{ ns}^{-1}$, $g_h = 0.08$, $\epsilon = 0.03 \text{ ns}$ and $\gamma = 1 \text{ ns}^{-1}$

The exact combined fidelity and the perturbative expansion is in excellent agreement, especially in the area where fidelity reaches its maximal value, as expected.

Appendix D

Phonons

D.1 Phonon Coherent State

To argue that the phonons can be written as a coherent state, we use the Glauber-Sudarshan P representation which is a quasi probability distribution able to tell if a system can be written as a coherent state. More specifically, the P representation is the function $P(\beta)$ which diagonalizes the density matrix $\hat{\rho}$ in the basis of coherent states $\{|\beta\rangle\}$,

$$\hat{\rho} = \int P(\beta) |\beta\rangle \langle\beta| d^2\beta. \quad (\text{D.1})$$

Assuming the quantum dot to be a black body, the P representation is

$$P(\{\beta_k\}) = \prod_k \frac{1}{\pi \langle \hat{n}_k \rangle} e^{-|\beta|^2 / \langle \hat{n}_k \rangle},$$

where

$$\langle \hat{n}_k \rangle = \frac{1}{e^{\hbar\omega/k_B T} - 1} \quad (\text{D.2})$$

which is known as Planck distribution or Bose-Einstein distribution.

If the quantum system has a classic analogue, in our case a coherent state, then P is all ways non-negative. Hence, as long the Boltzmann factor $e^{\hbar\omega/k_B T}$ is not below one, we may assume the phonons to be in a coherent state. At sufficient low temperatures, where only acoustic phonons need to be considered, this is indeed the case.

D.2 Displaced Vacuum

Since the phonons are in a coherent state, we may express them as displaced vacuum states

$$\sum_k D(\beta_k) |0\rangle = \{\beta_k\}, \quad (\text{D.3})$$

where

$$D(\beta_k) = e^{\beta_k(t) \hat{b}_k^\dagger - \beta_k^*(t) \hat{b}_k} \quad (\text{D.4})$$

is the displacement operator for a phonon with wavenumber k .

The following properties of the displacement operator will be needed:

$$\hat{D}_k(\beta_k) = e^{\beta_k(t)\hat{b}_k^\dagger - \beta_k^*(t)\hat{b}_k} = e^{-\frac{1}{2}|\beta_k|^2} e^{\beta_k(t)\hat{b}_k^\dagger} e^{-\beta_k^*(t)\hat{b}_k}, \quad (\text{D.5})$$

and

$$\hat{D}^\dagger(\beta_k)\hat{b}\hat{D}(\beta_k) = \hat{b} + \beta_k \quad (\text{D.6})$$

$$\hat{D}(\beta_k)\hat{b}\hat{D}^\dagger(\beta_k) = \hat{b} - \beta_k. \quad (\text{D.7})$$

Bibliography

- [1] C. E. Shannon, A mathematical theory of communication. Bell System Technical Journal **27** (1948)
- [2] P. Benioff, *The computer as a physical system: A microscopic quantum mechanical Hamiltonian model of computers as represented by Turing machines*. Journal of Statistical Physics **22** (1980), page: 563–591.
- [3] Y. I. Manin, *Vychislimoe i nevychislimoe*. Sov.Radio. page: 13–15 (1980).
- [4] R. P. Feynman, *Simulating physics with computers*. International Journal of Theoretical Physics **21**, page: 467-488 (1982).
- [5] D. Deutsch, Quantum Theory, the Church-Turing Principle and the Universal Quantum Computer. Proceedings of the Royal Society of London A. **400** (1985).
- [6] P. Shor, *Polynomial-time algorithms for prime factorization and discrete logarithms on a quantum computer*. SIAM J. Sci. Stat. Comput **26** (1997).
- [7] A. Montanaro, *Quantum algorithms: an overview*. npj Quantum Inf. **2**, 15023 (2016).
- [8] C. H. Bennett, G. Brassard *Quantum cryptography: Public key distribution and coin tossing*. Proceedings of IEEE International Conference on Computers, Systems and Signal Processing **175**, page: 8 (1984).
- [9] W. B. Gao, et. al, *Observation of entanglement between a quantum dot spin and a single photon*. Nature **491**, pages 426–430 (2012)
- [10] J. P. Lee, et. al, *Towards a source of multi-photon entangled states for linear optical quantum computing*. arXiv:1804.11311 (2018).
- [11] Klaus Mattle, et. al, *Dense Coding in Experimental Quantum Communication*. Phys. Rev. Lett. **76** (1996).
- [12] C. H. Bennett, et. al, *Teleporting an Unknown Quantum State via Dual Classical and Einstein-Podolsky-Rosen Channels*. Phys. Rev. Lett. **70** (1993).
- [13] B. Hensen, et. al, *Loophole-free Bell inequality violation using electron spin separated by 1.3 kilometres*. Nature **526** (2015).
- [14] M. Hillery, et. al, Quantum secret sharing. Phys. Rev. A **59** (1999)
- [15] Li Xiao, et. al, Efficient multiparty quantum-secret-sharing schemes. Phys. Rev. A **69** (2004).
- [16] R. Raussendirf, et. al, *Measurement-based quantum computation with cluster states*. arXiv:quant-ph/0301052

- [17] P. Michler, *Single semiconductor quantum dots*. NanoScience and Technology, Berlin, Heidelberg: Springer Berlin Heidelberg (2009).
- [18] J. Riel, et. al, *InAs/GaAs self-assembled quantum dots: Arsenic pressure and capping effects*. J. Cryst. Growth 236, 145–154 (2002).
- [19] A. Greilich, et. al, *Mode locking of of Electron Spin Coherence in Singly Charged Quantum Dots*. Science **313**, 341-345 (2006).
- [20] S. A. Crooker, et. al, *Spin noise of electrons and holes in self-assembled quantum dots*. Phys. Rev. Lett. **104**,036601 (2010).
- [21] H. Drexler, et. al, *Spectroscopy of quantum levels in charge-tunable InGaAs quantum dots*. Phys. Rev. Lett. **73**, 2252-2255 (1994).
- [22] R. J. Warburton, et. al, *Optical emission from a charge-tunable quantum ring*. Nature **405**, 926-929 (2000).
- [23] Peter Lodahl, Sahand Mahmoodian and Søren Stobbe. *Interfacing single photons and single quantum dots with photonic nanostructures*. Rev. Mod. Phys. **87** (2015).
- [24] R. J. Warbuton *Single spins in self-assembled quantum dots* Nature Materials, **12** (2013).
- [25] <http://www.photonspot.com/detectors>
- [26] M. H. Appel *Spin Dynamics of a Negatively Charged Quantum dot in a Nanobeam Waveguide*. Master Thesis, University of Copenhagen (2017).
- [27] J. H. Prechtel, et. al, *Electrically-tunable hole g-factor of an optically-active quantum dot for fast spin rotations*. arXiv:1412.4238v1 (2014)
- [28] I. Hapke-Wurst, et. al, *Mapping the g factor of InAs self-assembled quantum dots*. Physica E 12 (2002)
- [29] A. Hogele, et al, *Spin-selective optical absorption of singly charged excitons in a quantum dot*. Appl. Phys. Lett., **86** (2005)
- [30] C. E. Pryor, et. al, *Landé g Factors and Orbital Momentum Quenching in Semiconductor Quantum Dots*. Phys. Rev. Lett. **PRL 96** (2006)
- [31] N. J. Traynor, et. al, *Zeeman splitting and g factor of a heavy-hole excitations in $In_xGa_{1-x}As/GaAs$ quantum wells*. Phys Rev. B **51** (1995).
- [32] E. Aubry, et. al, *Anisotropic spin splitting of the electron ground state in InAs quantum dots*. Applied Physics Letters **90** (2007).
- [33] U. Berhard, et. al, *Nuclear spin physics in quantum dots: an optical investigation*. arXiv:1202.4637v2 (2012).
- [34] J. Fischer, et. al, *Spin decoherence of a heavy hole coupled to nuclear spins in a quantum dot*. Phys. Rev. B **78** (2008)
- [35] E. A. Chekhovich, et. al, *Isotope sensitive measurement of the hole-nuclear spin interaction in quantum dots*. ArXiv eprint 1109.0733 (2011)
- [36] P. Fallahi, et. al *Measurement of a Heavy-Hole Hyperfine Interaction in InGaAs Quantum Dots Using Resonance Fluorescence*. Phys. Rev. Lett. **105** (2010).

- [37] W. A. Coish, et. al, *Hyperfine interaction in a quantum dot: Non-Markovian electron spin dynamics*. Phys. Rev. B **70** (2004).
- [38] B. Urbaszek, et. al *Nuclear spin physics in quantum dots: An optical investigation*. Reviews of Modern Physics, **85** (2013).
- [39] J. G. Tischler, et. al, *Fine structure of trions and excitons in single GaAs quantum dots*. Phys. Rev. B **66** (2002).
- [40] T. Belhadj, et. al, *Impact of heavy hole-light hole coupling on optical selection rules in GaAs quantum dots*. Appl. Phys. Lett. **97** (2010)
- [41] T. Lund-Hansen, S. Stobbe, B. Julsgaard, H. Thyrrestrup, T. Sünner, M. Kamp, A. Forchel, and P. Lodahl, *Experimental realization of highly efficient broadband coupling of single quantum dots to a photonic crystal waveguide*. Phys. Rev. Lett. **101**, no. 11 (2008)
- [42] X. Xu, et. al. *Coherent population trapping of an electron spin in a single negatively charged quantum dot*. Nature Phys. **4** (2008)
- [43] D. Press, et. al. *Ultrafast optical spin echo in a single quantum dot*. Nature Photon **40** (2010).
- [44] K. Hennessy, et. al, *Quantum nature of a strongly-coupled single quantum dot-cavity system*. Nature, **445**, p. 896 (2007)
- [45] V. Loo, et. al, *Quantum dot-cavity strong-coupling regime measured through coherent reflection spectroscopy in a very high-Q micropillar*. Applied Phys. Lett. **97**, p. 241110 (2010)
- [46] M. Jönsson, G. Björk *Evaluating Performance of Photon-Number-Resolving Detectors*. arXiv:1812.05422v2 (2018)
- [47] M. Atatüre, et. al, *Quantum-Dot Spin-State Preparation with Near-Unity Fidelity*. Science **312**, 551 (2006).
- [48] P. Tighineanu, et. al, *Phonon Decoherence of Quantum Dots in Photonic Structures: Broadening of the Zero-Phonon Line and the Role of Dimensionality*. arXiv:1702.04812v3 [cond-mat.mes-hall] 22 (2008).
- [49] L. C. Andreani, et. al, *Effect of inhomogeneous broadening on optical properties of excitons in quantum wells*. Phys. Rev. B **57** (1998)